Progress in Materials Science 117 (2021) 100734

Contents lists available at ScienceDirect

Progress in Materials Science

journal homepage: www.elsevier.com/locate/pmatsci

A review on molten salt synthesis of metal oxide nanomaterials: Status, opportunity, and challenge

Santosh K. Gupta [a], Yuanbing Mao [b,*]

[a] Radiochemistry Division, Bhabha Atomic Research Centre, Trombay, Mumbai 400085, India
[b] Department of Chemistry, Illinois Institute of Technology, 3101 South Dearborn Street, Chicago, IL 60616, USA

ARTICLE INFO

Keywords:
Molten salt synthesis
Nanomaterials
Metal oxides
Nanoparticles

ABSTRACT

Molten-salt synthesis (MSS) method becomes an excellent bottom-up synthesis technique of nanomaterials with various chemical compositions and morphologies because of its meritorious features including environmental friendliness, low cost, simple to operate, easy to scale-up, etc. This review article highlights the status, potential and challenges of MSS for the synthesis of metal oxide nanomaterials. It gives a concise flavour on the importance of synthesis on the properties and application of nanomaterials. We have compiled a brief write-up on a few frequently used synthesis methods and their advantages and disadvantages. This review article encompasses different aspects of MSS such as the role of molten salt, the choice of molten salt, the effect of various synthesis parameters, typical oxosalts and their electrochemical aspects. Some advanced modifications of the MSS method and their implications are also discussed in brief citing a few examples. For readers to have a completed understanding and feel of MSS, both pros and cons of it have been discussed as well. The recent progress in MSS of inorganic metal oxide nanoparticles is reviewed in this article. We start with simple binary oxides and then explain a few technologically important cases of complex metal oxide nanomaterials. This review article also highlights how the MSS method has been successful in synthesizing ABO_2 delafossite, ABO_3 perovskite, AB_2O_4 spinel and $A_2B_2O_7$ pyrochlore nanomaterials. This review article opens a new avenue for exploring MSS in making size and shape tunable nanomaterials for various catalytic, optoelectronic, magnetic, and electrical applications.

1. Introduction

Nanomaterials are not only a very important footmark in the area of miniaturization, but also an important milestone as the nanosized domain lies in between atomic and quantum realm and the bulk scale. Once a material goes down to nanodomain, their physical, biological and chemical properties are governed mostly by quantum physics, rather than classical physics governing the bulk phase [1]. Such differences arise mainly due to enhanced surface area, increased chemical reactivity and mechanical strength [2]. Based on different parameters such dimension, phase composition and manufacturing process, they can be classified into various categories (Table 1) [3]. These properties of nanomaterials have led to their use for various applications which are classified mostly based on surface properties (Table 2). Particularly for applications in the areas of optics, magnetism and catalysis, nanomaterials have been fetching lot of attention in the scientific community.

* Corresponding author.
E-mail address: ymao17@iit.edu (Y. Mao).

https://doi.org/10.1016/j.pmatsci.2020.100734
Received 22 January 2019; Received in revised form 14 August 2020; Accepted 8 September 2020
Available online 15 September 2020

The properties governing these applications are strongly influenced by particle size, phase composition and shape of nanomaterials, therefore, synthesis plays a very important role in designing well defined, monodisperse and uniform nanostructured materials [10–12]. There has been a great deal of effort invested in nanoscience related research pertaining to improved design strategies for making size and phase specific nanomaterials with well-defined morphology and narrow size distribution in order to improve their existing chemical and physical behaviours [13–16]. Specifically, in order to have improved optical, magnetic and catalytic properties, it was found that nanomaterials need to have optimum size, shape, crystallinity, pH, surface area, etc. [17–19]. The perfect balance of all these characteristics of nanomaterials are needed for them to work efficiently for specific applications. Other than optimizing these properties, synthesis methods should be simple enough to be reproducible, cheap, easily scalable, green, and clean, and not lead to any kind of hazards in a lab or industrial scale. Particularly green chemistry is the demand of scientific and social community. The generation of hazardous substances and waste production also should be bare minimum.

Because of various favourable and non-toxic properties associated with oxide systems, there have been increased demands for metal oxide nanomaterials for many scientific and technological applications particularly in the areas of medical sciences, information technology, catalysis, energy storage and sensors [20]. Consequently, there has been an upsurge in research related to designing new synthesis strategies for metal oxide nanomaterials. There have been many wet chemical routes reported in literature for the synthesis of nanomaterials such as hydrothermal, sol–gel, co-precipitation, microemulsion, combustion, etc. [21]. Many of these techniques involve toxic and costly chemicals, sophisticated instrumentation, organic solvent for washing, etc.

Through molten salt synthesis (MSS) method it is reported that metal oxide nanoparticles (NPs) can be synthesized very rapidly and efficiently from suitable metal ion precursors along with proper flux/molten salt at temperatures beyond the melting point of the salts [22,23]. MSS is a simple techniques which is cheap, clean and scalable [14,24]. Because of its various favourable properties and easy to scale, MSS is expected to be used for nanomaterial synthesis at industrial level [14,22,23,25–30].

Compared to conventional solid-state synthesis route where chemical reactivity is limited by the large diffusion length and slow diffusion of the reacting constituents, the MSS method has lower formation temperature of products as it facilitates fast movement of solids in liquid molten salt phase by means of convection and diffusion. In wet chemical synthesis, solvation is the most crucial step. Most of molecular solvents used in synthesis fail to solvate all metal ions and inorganics. In case of the MSS method, ionic molten salts are used to facilitate chemical reactions at low temperature. Unlike in other synthesis systems, it is possible that most of the metal ions or ionic/covalent bond can get easily destabilized in the MSS process by solvents from the strong polarization induced by molten salt (a pool of ionized cations and anions) at relatively high temperature. One of other important aspects of the MSS method is the high aqueous solubility of molten salts which allows their easy removal at the end of chemical reaction and makes the efficient isolation of products from synthesis reaction mixture. These kinds of molten salts have been used in both academia for research purpose and industry. In fact, molten salts have been used in many inorganic and organic chemical reactions as suitable solvent media and help in growth of crystalline products for quite a long time [31–33].

The aim of this review article is to present the state of the art of the current researches performed by the nanoscience community on the recent synthesis advances of inorganic materials via the MSS method particularly in nanodomain. To give a concise flavor of the MSS method for nanomaterials, we start with a general and brief introduction of synthesis methods for nanomaterial. Then we describe the role of molten salts and their chemical and physical aspects with some widely used salt melt systems as examples. Afterwards, we discussed the synthesis parameters, pros/cons, and some advanced techniques of the MSS method. Finally, we summarize the nanomaterials obtained by the MSS approach in the categories of binary and complex metal oxides. Only a few examples in each type of above-mentioned materials are mentioned since an exhaustive presentation of all accessible materials is impossible.

2. General synthesis methods for nanomaterials

For getting desired properties from nanomaterials, it is especially important to synthesize them in a controlled manner. Particularly size and shape of nanomaterials have huge role in optimizing their properties for specific applications. Some of the important synthesis

Table 1
Classification of nanomaterials with regard to different parameters [3].

Classification	Examples
Dimension	
3 dimensions < 100 nm	Particles, quantum dots, hollow spheres, etc.
2 dimensions < 100 nm	Tubes, fibers, wires, platelets, etc.
1 dimension < 100 nm	Films, coatings, multilayer, etc.
Phase composition	
Multi-phase solids	Matrix composites, coated particles, etc.
Single-phase solids	Crystalline, amorphous particles and layers, etc.
Multi-phase systems	Colloids, aerogels, ferrofluids, etc.
Manufacturing process	
Gas phase reaction	Flame synthesis, condensation, chemical vapor deposition, etc.
Liquid phase reaction	Microemulsion (reverse micelle), sol–gel, precipitation, hydrothermal/solvothermal process, sonochemical process, etc.
Mechanical procedures	High energy ball milling, plastic deformation, etc.

Table 2
Properties and applications of nanomaterials.

Surface Properties	Application examples
Mechanical properties (e.g. tribology, hardness, scratch-resistance).	Wear protection of machinery and equipment, mechanical protection of soft materials (polymers, wood, textiles, etc.) [4]
Wetting properties (e.g. anti-adhesive, hydrophobic, and hydrophilic).	Anti-graffiti, anti-fouling, lotus-effect, self-cleaning surface for textiles and ceramics, etc. [5]
Thermal and chemical properties (e.g. heat resistance and insulation, corrosion resistance).	Corrosion protection for machinery and equipment, heat resistance for turbines and engines, thermal insulation equipment and building materials, etc. [6]
Biological properties (biocompatibility, anti-infective).	Biocompatible implants, anti-bacterial medical tools and wound dressings, etc. [7]
Electronic and magnetic properties (e.g. magneto resistance, dielectric).	Ultra-thin dielectrics for field-effect transistors, magneto-resistive sensors and data memory, etc. [8]
Optical properties (e. anti-reflection, photo- and electro-chromatic).	Photo- and electro-chromic windows, anti-reflective screens and solar cells, etc. [9]

parameters which play decisive roles in fine tuning the size, shape, and surface properties of nanomaterials are precursor used, annealing time, rate of heating and cooling, annealing temperature, pH, concentration, etc. [34].

Nanomaterials can be synthesized by various methods that are categorised into bottom-up and top-down approaches. A simplified representation of these two processes is shown in Fig. 1. Top-down methods involve the breaking of bulk materials into NPs. Some of the widely explored examples of these methods are nanolithography, laser ablation, mechanical milling, sputtering and thermal decomposition [35]. Most of these methods need highly sophisticated, costly and complex instrumentation for specific conditions. Also there are associated problems of large surface defects and non-uniform shapes by top-down methods which drastically limit their applications [35].

On the other hand, bottom-up methods are entirely opposite to the top-down methods in a sense that molecular species are integrated to form nanomaterials. They resulted from bonding atom to clusters and then to nanomaterials. Some of the well-known examples include sol–gel, electrospinning, chemical/physical vapour deposition, combustion, hydrothermal, solvothermal, MSS, sonochemical, micro emulsion, co-precipitation, polymer precursor route, pyrolysis, and biosynthesis. In general, the bottom-up approaches are relatively simple, inexpensive, and easy to carry out in laboratory scale compared to the top-down approaches. Moreover, they also allow better control over size, composition and shape of nanostructured materials which directly impact their properties. Because of these reasons bottom-up approaches based on wet chemical synthesis are more successful and widely used techniques in research community working on nanomaterials. Some of the bottoms up approaches involving wet chemical routes are discussed briefly in the following sections. All these wet chemical routes have a major advantage over solid-state synthesis methods that they lead to drastic reduction in diffusion path lengths and therefore reaction completes in much shorter time and requires less thermal energy.

2.1. Sol-gel method

Sol–gel synthesis technique of nanomaterials proceeds via the formation of inorganic network through the synergy of sol (colloidal suspension of solid particles) and gel (3D continuous solid porous networks). One of the requirements of the sol–gel method is a water-soluble metal precursor such as metal alkoxides. Formation of particles in nanodomain requires stringent control over nucleation and growth kinetics. These steps are rather difficult to acquire in sol–gel process because of the complexity involved in the formation of sol and gel through hydrolysis and condensation steps. Such complexity in sol–gel process arises mainly due to a large number of process parameters which need to be controlled at microlevel to provide good reproducibility. Some of them are kinetics of hydrolysis and condensation steps, pH of the solution, step duration, reaction temperature, catalyst concentration, etc. [37]. Fig. 2a schematically shows the formation of sol and gel in a sol–gel process utilizing metal alkoxides as precursors and resorcinol–formaldehyde.

2.2. Polymeric precursor method

Polymeric precursor method for the synthesis of nanomaterials is based on Pechini-type reaction route [41]. The process initiates

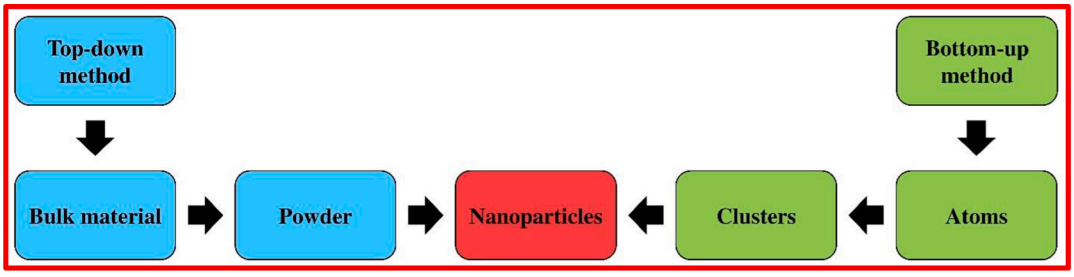

Fig. 1. General synthesis processes for nanomaterials [36]. *Copyright 2017. Reproduced with permission from IOP publishing.*

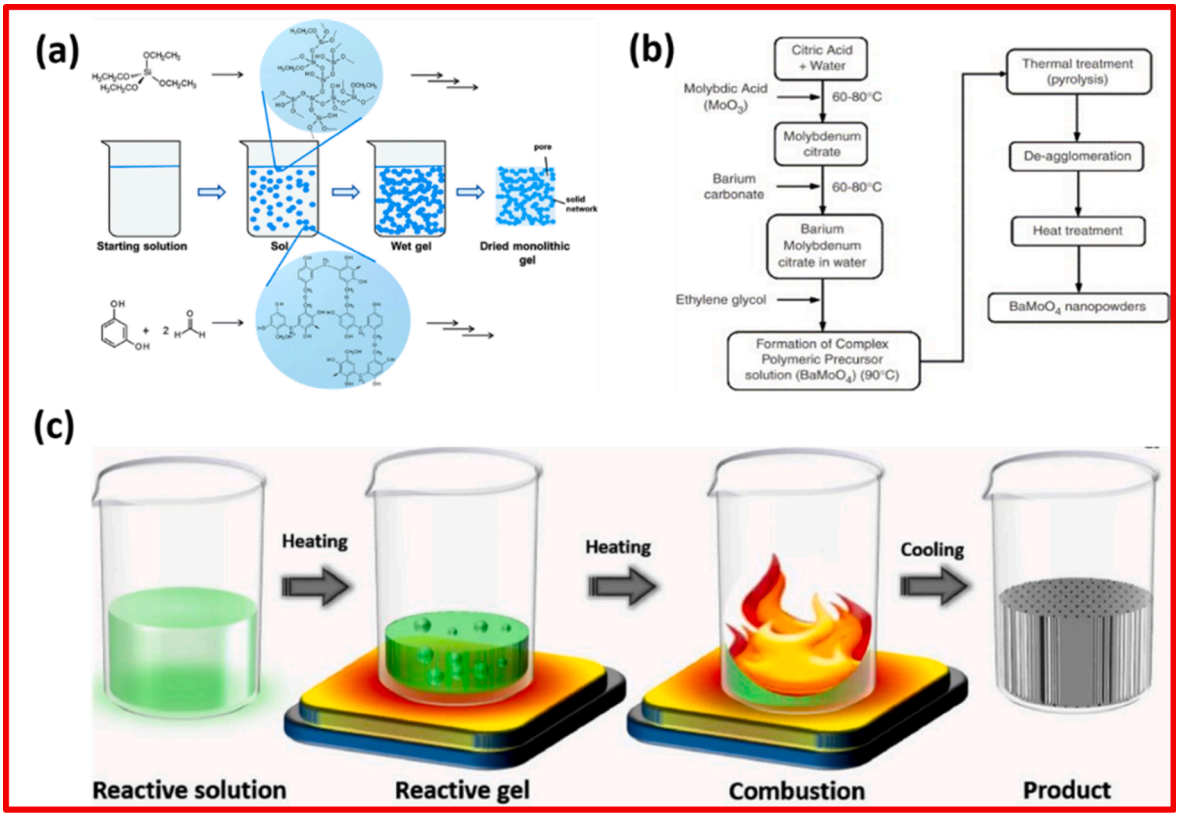

Fig. 2. (a) Sol-gel methods showing the formation of sol and gel starting from silicon alkoxides and resorcinol/formaldehyde [38]. *Copyright 2016. Reproduced with permission from Royal Society of Chemistry.* (b) Typical steps in complex polymerization method used for the synthesis of $BaMoO_4$ [39]. *Copyright 2006. Reproduced with permission from Elsevier.* (c) Schematic representation of the steps for conventional solution combustion synthesis process [40]. *Copyright 2017. Reproduced with permission from Elsevier.*

by formation of polymeric gel which is formed as a result of chemical reaction involving citric acid (complexing agent), ethylene glycol (stabilizing agent) and the metal ionic precursor. In this reaction the metal ions get immobilized in polymeric gel and finally charred off on heating. Fig. 2b shows the various steps involved in polymeric precursor synthesis of $BaMoO_4$. Some of the most important advantages associated with this process are low synthesis temperature, homogenous product formation, stabilization of metastable phase, etc. There are also several limitations, such as complex chemicals are used, it is difficult to maintain stoichiometry in few cases, sometimes it becomes very difficult to find suitable chemical precursors (for example, pentavalent tantalum and niobium ions immediately hydrolyze and precipitate in aqueous solution).

2.3. Gel-combustion method

Combustion synthesis is also explored extensively for synthesis of nanomaterial in scientific community. It basically involves two steps: precursor formation and auto-ignition (Fig. 2c) [42]. In combustion synthesis, product formation takes place via exothermic reaction that takes place between metal ion precursors (mostly water soluble) and a fuel (citric acid, glycine, urea, etc.) which generates sufficient amount of heat for combustion reaction. This heat of combustion pushes the reaction in forward direction [43]. One can tune the size of NPs by changing the fuel to oxidant ratio and therefore choice and composition of fuel is of paramount importance. Various advantages and limitations of this method over other routes are mentioned in Table 3.

Table 3
Advantages and disadvantages of combustion synthesis route.

	Advantages	Disadvantages
1	Requires less thermal energy as result of reduced diffusion length	Safety is major issue
2	Particle size can be controlled by altering fuel to oxidant ratio	Evolution of NO_x which is highly toxic
3	Cost efficient	Morphology tuning is an issue
4	Metastable states can be synthesized	Non-oxide ceramic is very difficult to synthesize

2.4. Microemulsion method (reverse micellar route)

Synthesis of NPs via microemulsions is a simple and powerful technique, which does not require specialized or expensive equipment. Here chemical reaction takes place in small aqueous core which is dispersed in non-polar solvent. Such reverse micelles are stabilized by employing surfactant/co-surfactant [44]. It leads to the formation of highly homogenous product because requisite stoichiometry is maintained throughout the chemical reaction. Microemulsion can assume different kind of shapes based on the constituents and the location within the phase diagram. One can tune the size and shape of NPs by changing the water to surfactant ratio of microemulsion. While the reverse micelle method clearly leads to lowering of the calcination temperatures for the formation of single phase, a question that follows is the cost of the reverse micelle method itself and the feasibility of employing this method for scale-up. Such method is also not considered as a chemically 'green' process.

2.5. Hydrothermal/solvothermal synthesis

Hydrothermal/solvothermal synthesis involves fabricating ceramic compounds directly from solutions at elevated temperature and pressure [45]. The size and stability of the final compound is highly dependent on pH of the reaction medium, composition, temperature and time [1]. Reaction rate in hydrothermal/solvothermal process can be significantly increased by coupling it with microwave radiation, ultrasonication, electromagnetic radiation, etc. There are several issues in hydrothermal/solvothermal synthesis, such as various synthesis steps, usage of large amount of organic reagents, which increases the cost and at the same time leads to environmental pollution, making them not easy to scale up.

3. MSS

Fused/molten salts or their mixtures are dissociated commonly into ions during operation and are widely used in many industrial processes which need to be free from the limitations associated with the use of aqueous and organic solvents. A number of their properties, including their high thermal stability, generally low vapor pressure, high thermal and electrical conductivity, and low viscosity, has qualified them as excellent reaction media, so molten salts have been widely adopted to high-temperature chemistry with fast reaction rates [33]. Their ability to dissolve many inorganic compounds makes them ideal solvents useful in electrometallurgy,

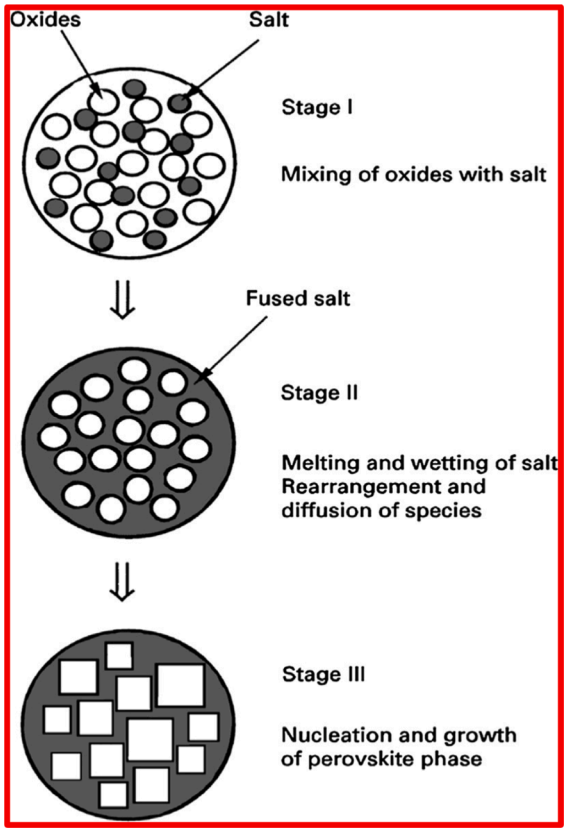

Fig. 3. Schematic illustration of the main processing stages of the MSS method for synthesis of perovskite oxide powders [68]. *Copyright 2006. Reproduced with permission from Elsevier.*

metal coating, treatment of byproducts, and energy conversion.

Laboratory research using molten salts has never stopped to explore new ways for interesting applications. Here the MSS method is explored as one of simple, green, scalable, cost efficient, versatile and generalizable synthesis techniques for making high quality nanomaterials because of various favorable properties of molten salts such as non-toxicity, cost efficient, low vapor pressure, easy availability, high heat capacity, large electrochemical range, and high ionic conductivity [14,24,30,46–48]. The two most important aspects of MSS which makes it a highly superior technique among its peers is the reduction of product formation temperature and its efficacy in generating uniform particles. The increased reactivity of the MSS method is attributed to two aspects: enhancement in mobility and contact area of reactant molecules in the molten salts. So far, it has been demonstrated to prepare nanomaterials with different morphologies [23]. The final products by the MSS method are formed in a flux of salts with low melting point which tends to partially dissolve the reacting species and hence facilitates efficient ionic diffusion and chemical reactions among reactants. Therefore, products are formed at relatively lower temperature in the MSS process compared with conventional solid state reaction (SSR) route [49]. Moreover, the MSS does not require any sophisticated instrumentation or costly chemicals and can be easily performed in common chemistry laboratory.

All these properties are ideal and make the MSS highly feasible for large scale industrial synthesis of nanomaterials for various scientific and technological applications using this simple, green and cheap approach [14,22,23,25–30,50]. It is also successful in producing other complex nanomaterials such as Si [51], metal boride [52], SiC [53,54], Ge [55], boron based nanocomposites [56], porous B-doped carbons [57], intermetallics [58], graphite [59], $KSr_2Nb_5O_{15}$ [60], Ti_4N_3 [61], etc. There have been a few recent reports on the exploration of MSS for stable colloids [62], 2D metal oxide [63], metal ion doping [64], non-metal doping [65], quantum dots [66], etc. Molten salts act as a solvent and help form crystalline products from both inorganic and organic chemical reactions [31–33]. Nanomaterials with different morphologies and tunable sizes have also been reported by the MSS synthesis method [46,67].

As pictorially depicted in Fig. 3, three different stages are defined in an MSS process. Stage I involves the mixing of precursors with a salt (e.g., $NaNO_3$, KNO_3, NaCl, and KCl) or with a eutectic mixture (e.g., NaCl-KCl, NaOH-KOH, and $NaNO_3$-KNO_3). The second stage involves the heating of precursor and salt mixture above the melting temperature of the salt to form a molten flux. At this stage, various physical processes take place within the molten salt: uniform dispersion of precursor molecules, dissociation, rearrangement and diffusion. At stage III, nucleation and growth of the product particles starts via solution-precipitation process. Growth of the particles may be governed by Ostwald ripening. The particles which are much smaller than certain critical size get dissolved in molten salt as the expense of the growth of large particles. The heating temperature and time play important roles in controlling final powder characteristics. Once annealing is done on the mixture of precursor and salt in a furnace, they are cooled slowly and washed with water which is the most suitable solvent for the MSS to remove the used salt.

For a long time, molten salts have been used in flux synthesis method to increase the rate of reaction as an additive. Usually the amount of molten salts used in flux synthesis reactions is small. On the other hand, large amount of molten salts is used as solvents in MSS process to synthesize particles and control their final powder characteristics. This is the basic difference between MSS and flux method: MSS uses molten salts as solvents where flux method employs them as additives [69]. MSS proceeds via two important mechanisms before final products are formed: first one is that all reactant species are fully dissolved in molten salts and rapidly diffuse into each other [70]. The second one is that there is higher solubility of one reactant compared to that of others in molten salts which diffuses to other components rapidly and reacts with them, therefore, products have similar morphology as that of low solubility component [71]. Because the important roles of the selected molten salts in a MSS process, selection criteria of molten salts, and types of molten salts are described in the following sections.

3.1. Selection criteria of molten salts

The selection of salts for the MSS method is an important part of the entire MSS process. Oxosalts are the most commonly employed choices which include hydroxides, nitrates, sulfates, and carbonates. Most extensively used salts in MSS include nitrates, hydroxides, chlorides, and sulfates. The synthesis of many complex metal oxides requires eutectic salt mixtures to lower the melting temperature to assist product formation. The melting temperatures of individual alkali halides of NaCl and KCl are 801 °C and 770 °C, respectively, and that of 0.5NaCl–0.5KCl (50–50 eutectic composition) is 650 °C. The mixture of $0.635Li_2SO_4$–$0.365Na_2SO_4$ is one of the most frequently used eutectic mixtures because of its low eutectic point of 594 °C. The eutectic point of Na_2SO_4–K_2SO_4 is 823 °C. Oxides solubility in molten salts varies typically between 1×10^{-3} and 1×10^{-7} mole fraction [72]. In many cases of solid state synthesis, the product formation takes place with the presence of solid reactant particles aided with molten salts. Molten salts differ from normal solvents in a sense that all reactant species are dissolved in solvents and the product formation takes place from a homogeneous liquid phase. On the other hand, MSS exploits the use of low-melting point solvents like alkali chlorides, sulfates, nitrates, or hydroxides, for the synthesis of the ceramics in nanosized and bulk forms.

Therefore, molten salts play a variety of crucial roles in the MSS process: enhances the chemical reactivity of reactant species, reduces synthesis temperature, decreases the degree of final product agglomeration, and makes final product powder homogeneous [69]. Therefore, the selection of suitable molten salts in a MSS process is of paramount importance and it should satisfy three most important features: low melting point, compatibility with reactants and high aqueous solubility so that it can be easily eliminated after synthesis just by simple washing with water [30].

Other important requirements of molten salts are high stability, low reactivity, ease of availability and cost efficient. Vapor pressure of molten salts at heating temperature should be low so that unnecessary evaporation and loss could be minimal. Their low reactivity could avoid reactions of molten salts with reactants/products. One example of unsuitable salts is LiCl for the MSS of $LiFe_5O_8$ [73]. LiCl

enhances the chemical reaction between Fe_2O_3 and Li_2CO_3 to yield $LiFe_5O_8$, but its high volatility and hygroscopic nature makes the synthesis setup cumbersome [74]. Moreover, it picks up water easily and forms Li_2O which reacts with $LiFe_5O_8$ to form $LiFeO_2$. Lin et al. successfully synthesized bulk $LiFe_5O_8$ using Li_2SO_4–Na_2SO_4 eutectic mixture [75].

3.2. Categories of molten salts

3.2.1. Metal halide systems

Based on the chemical characteristics, molten salts are classified into inert and reactive systems. For example, metal halides fall in the former category whereas metal hydroxides belong to the latter category. Inert halides are frequently used in MSS. Table 4 shows the list of various alkali metal halides along their melting points. Inertness of molten salt is also important for efficient MSS. The inert nature of alkali halides provides them with a large electrochemical window. It means that they are stable in the presence of strong reducing or oxidizing reagents, especially for fluorides and chlorides.

3.2.2. Oxosalt systems

For the synthesis of metal oxides nanoceramics, oxosalt systems, such as metal nitrate and sulfate, are preferred choices as a molten salt. Metal hydroxides are also considered good salts for the synthesis of oxide ceramics and behave similar to oxide ion when melting into mobile cations (M^{x+}) and anions (OH^-). Similar to water autoprotolysis, a Lux–Flood type acid–base equilibrium exists for oxide based molten salts by the reaction [77,78]:

$$\text{Oxobase (oxide donor)} \leftrightarrow \text{Oxoacid (oxide acceptor)} + O^{2-} \quad (1)$$

Proposed by German chemist Hermann Lux in 1939, this acid-base theory is a revisit to oxygen theory of acids and bases. It is further modified by Hakon Flood circa in 1947. It was found to be highly useful in explaining modern geochemistry and the electrochemistry of molten salts [79].

In this equation, the O^{2-} ion acts a simple base. The basicity of the molten salt is defined as $pO^{2-} = -\log m(O^{2-})$, similar to pH. Reaction feasibility in molten salts is determined by the magnitude of pO^{2-}. For example, if the value of pO^{2-} is moderate, TiO_2 precipitation occurs via:

$$Ti^{4+} + 2O^{2-} \rightarrow TiO_2 \quad (2)$$

If the value of pO^{2-} goes down further low, TiO_2 precipitate gets dissolved in titanates.

$$TiO_2 + O^{2-} \rightarrow TiO_3^{2-} \quad (3)$$

Metal nitrates, sulfates and hydroxides are considered as decent bases, so they can be good oxidizing agent and serve as good oxygen donors. For example, molten hydroxide has been used in a MSS process as a great alternative to synthesize lead free $K_{0.5}Na_{0.5}NbO_3$ [80]. The potential of metal hydroxides in the MSS has also been harnessed recently for the first synthesis of $Sr_4Mn_3O_{10}$ at the mesoscale as platelets at 600 °C [81]. Moreover, Hu et al. have reported on the rapid large scale production of 2D metal oxides/hydroxides using the MSS employing metal nitrates as salts [63]. Fig. 4 shows different ceramic materials synthesized using nitrates, hydroxides and sulfates as the molten salts. Fig. 4a depicts the general MSS scheme for 2D nanosheets of oxides and hydroxides. The molten salt used was a $NaNO_3$-KNO_3 mixture. The nanosheet formation is facilitated by very rapid reaction between ionized components from the $NaNO_3$-KNO_3 mixture and the precursor. In this work, the same strategy led to several cation and anion intercalated (CIC and AIC) oxides and hydroxides in nanometer thickness such as CIC manganese oxides ($Na_{0.55}Mn_2O_4{\cdot}1.5H_2O$ and $K_{0.27}MnO_2{\cdot}_0.54H_2O$), CIC tungsten oxides ($Li_2WO_4$ and $Na_2W_4O_{13}$), and AIC metal hydroxides ($Zn_5(OH)_8(NO_3)_2{\cdot}2H_2O$ and $Cu_2(OH)_3NO_3$) in a short time [63]. On the other hand, Fig. 4b shows the formation of multicationic $Sr_4Mn_3O_{10}$ platelets at the

Table 4
Melting points and compositions of some commonly used metal halides, hydroxides and oxosalt systems [23]. *Copyright 2013. Reproduced with permission from the Royal society of Chemistry.*

	Salt System	Composition (mol%)	Melting point (°C)
Halides	LiCl/KCl	59/41	352
	NaCl/KCl	50/50	658
	$AlCl_3$/NaCl	50/50	154
	KCl/$ZnCl_2$	48/52	228
	LiF/NaF/KF	46.5/11.5/42	459
	LI/KI	63/37	286
Oxosalts	NaOH/KOH	51/49	170
	$LiNO_3$/KNO_3	43/57	132
	Li_2SO_4/K_2SO_4	71.6/28.4	535
	Li_2CO_3/K_2CO_3	50/50	503
	Li_2CO_3/Na_2CO_3 [76]	50/50	500
	$NaNO_3$/KNO_3 [76]	50/50	228
	$LiBO_2$/KBO_2 [76]	56/44	582
	Na_2SiO_3/K_2SiO_3 [76]	18/82	753

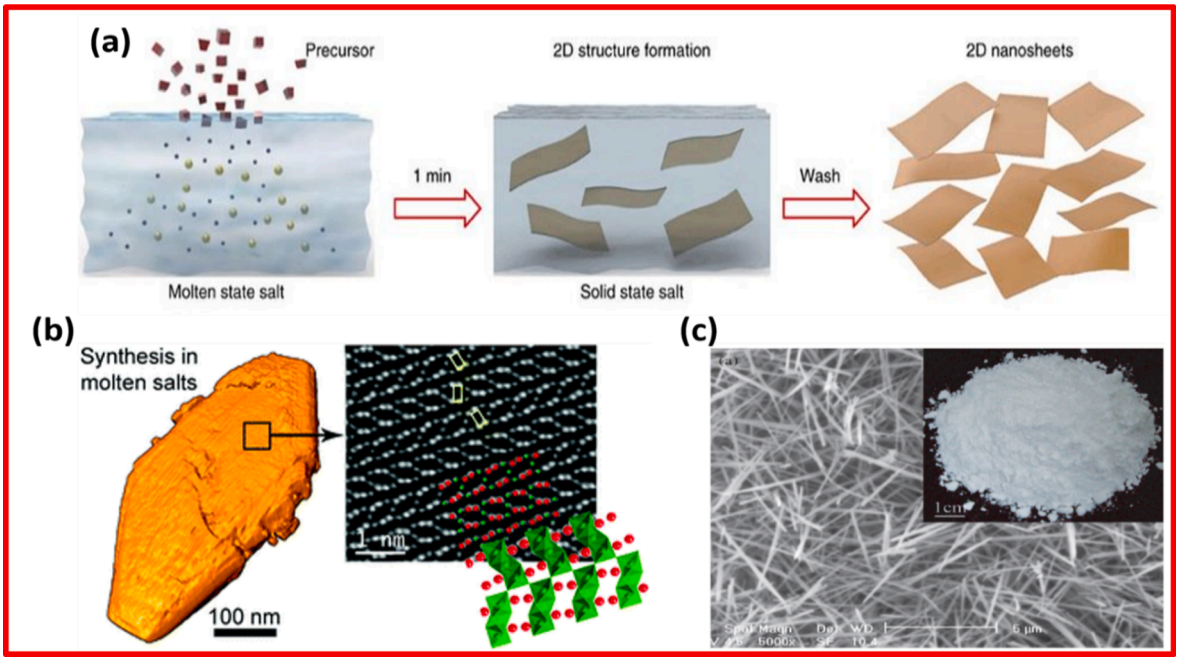

Fig. 4. MSS synthesis of (a) 2D oxides and hydroxides using metal nitrates [63]. *Copyright 2017. Reproduced with permission from Springer Nature Publishing.* (ii) multicationic mesostructures using metal hydroxides [81]. *Copyright 2018. Reproduced with permission from Royal Society of Chemistry.* (c) Mullite nanowires synthesized using metal sulfates [82]. *Copyright 2017. Reproduced with permission from American Scientific Publishers.*

mesoscale with the dimension of the basal face at 100 s of nm and the thickness in the range of 20–100 nm using the MSS method with $Sr(OH)_2$ as the molten salt at 600℃ . Fig. 4c displays the synthesis of single-crystalline mullite ($3Al_2O_3{\cdot}2SiO_2$) nanowires in a large quantity using the low cost and environmentally benign MSS method with Na_2SO_4 as the molten salt but no surfactant or template at 1000℃.

3.2.3. *Other systems: chalcogenides, chlorate and metalate*

Other than metal halides and oxides, metal chalcogenides are another option in the MSS of complex metal oxide-based transition metal ions though its role is slightly cumbersome. The chalcogenides play dual roles: act as both chalcogen donors and building blocks to final products. They also do an additional job of controlling the texture and the crystal structure of the finished products [83]. It is reported long back by Sunshine et al. that the synthesis of potassium titanium sulfide can be realized using the MSS at intermediate temperature [84].

Strong oxidizing agents like chlorate (ClO_3^-) can also be utilized for the MSS of materials where certain elements need to be stabilized at high oxidation state. For example, $KClO_3$ has been used for the synthesis of lead magnesium niobate $Pb(Mg_{1/3}Nb_{2/3})O_3$ powder from PbO, MgO and Nb_2O_5 [85]. Its strong oxidizing nature makes it as a suitable flux for synthesis of $Pb(Mg_{1/3}Nb_{2/3})O_3$ perovskite. Safety concerns related to metal chlorates restrict their applicability as it can leads to unwanted explosion when used in large quantity [86].

To synthesize compounds using the MSS process with similar metalate anions as building units, the use of salts with metalate ions could be extremely useful. For instance, the MSS of multicationic mesostructured $Sr_4Mn_3O_{10}$ requires metalate ions like MnO_4^- as a building block [81].

3.2.4. *Eutectic mixture systems*

To lower the reaction temperature of the MSS process, instead of using individual ionic salts, eutectic mixtures of salts are preferred owing to their lower melting point, reduced viscosity, and wider operation temperature range. Heterogeneous salt mixtures can suitably adjust the acid–base equilibrium so that there is preferential precipitation of targeted products. For example, Helan and group have explored chloride-carbonate mixed salt for the synthesis of $LiMn_2O_4$ [87].

3.3. *Synthesis parameters*

One can tune the size, shape and surface properties of the NPs synthesized by MSS with various salt-to-reactant (S/R) molar ratios, MSS annealing temperatures, MSS processing times, and other reaction conditions such as pH [88]. Our group has done systematic studies on exploring the effects of pH, processing time and annealing temperature on optical and scintillation properties of the MSS synthesized pyrochlore NPs [89–91]. These synthesis parameters which can affect the quality of products by MSS are discussed

systematically in the following sections.

Fig. 5 depicts the steps of the MSS method with the factors that can be manipulated to fine tune the physical and morphological properties of the final NPs. In the first step to prepare single-source complex precursors, certain parameters, such as the pH of the medium, can be adjusted to yield different sized NPs. Moreover, changing the molten salt mixture in the second step or the amount of salts used can have big impact on the morphology of the final NPs. In the MSS step, there are multiple parameters that can be adjusted. Changing the annealing temperature and ramp rate for example can alter the size and degree of agglomeration of the final products. Also, changing the annealing atmosphere can affect the number of oxygen vacancies in products. Finally, the choice of washing solvent, and technique used and dry the sample can also affect the agglomeration degree of the NPs.

3.3.1. Composition of salt (S_c)

Salt composition (S_c) plays an important role in MSS and its amount is basically decided by fact that how much interstitial space is there in the reactants and how much is needed to coat the surface of reacting species [69]. There have been report where S_c is known to affect the size of synthesized particles [92]. When S_c is too small, the implication of the liquid phase is not fully expected. On the other hand, if it is too high, there can be two main issues. The first one is that the reactant particles get separated sedimentation [73,93]. This separation is attributed to different sedimentation rates of reactant molecules due to their distinct size and density which ultimately affect the rate of reaction. The second problem is coming out of excess salts from reactant mixture due to limited availability of interstices which fail to hold all salt molecules. These salts which come out of reactant mixture no longer act as solvent. Moreover, such salts stick to the wall of alumina/SiC crucible and get converted to hard solid mass and dissolution of such filthy mass is very tedious [69].

There is an issue in the particle size of the MSS synthesized products even when all the reacting species dissolved in molten salts. Considering the case of bismuth tungstate which is synthesized using precursor of bismuth oxide and tungsten oxide in a NaCl-KCl eutectic mixture. It was found that two different kinds of plate-like particles of bismuth tungstate (Px and Py) are formed depending upon the value of S_c and heating conditions [94]. The size of Px is of the order of several microns whereas Py is approximately around 100 μm.

Let us assume two different scenarios in this case: (A) low S_c and low heating and (B) high S_c and high heating temperature. In scenario A, the system is positioned at solid–liquid phase boundary in a phase diagram. Consequently, nucleation of bismuth tungstate particles takes place on the surface of reacting molecules and large number of such particles is formed. In case B, the system is positioned at liquid phase only in a phase diagram and therefore homogeneous nucleation of bismuth tungstate takes place and we get more uniform particles. Compared to single crystals, the number of particles formed in an MSS process is much higher because of higher cooling rate but the particle nucleating heterogeneously is low in number and therefore large sized particle is formed.

3.3.2. Salt-to-reactant (S/R) molar ratios

Akdogan et al. have found profound influence of salt to oxide ratio on the product morphology of $Sr_3Ti_2O_7$ (Fig. 6) [95]. They found

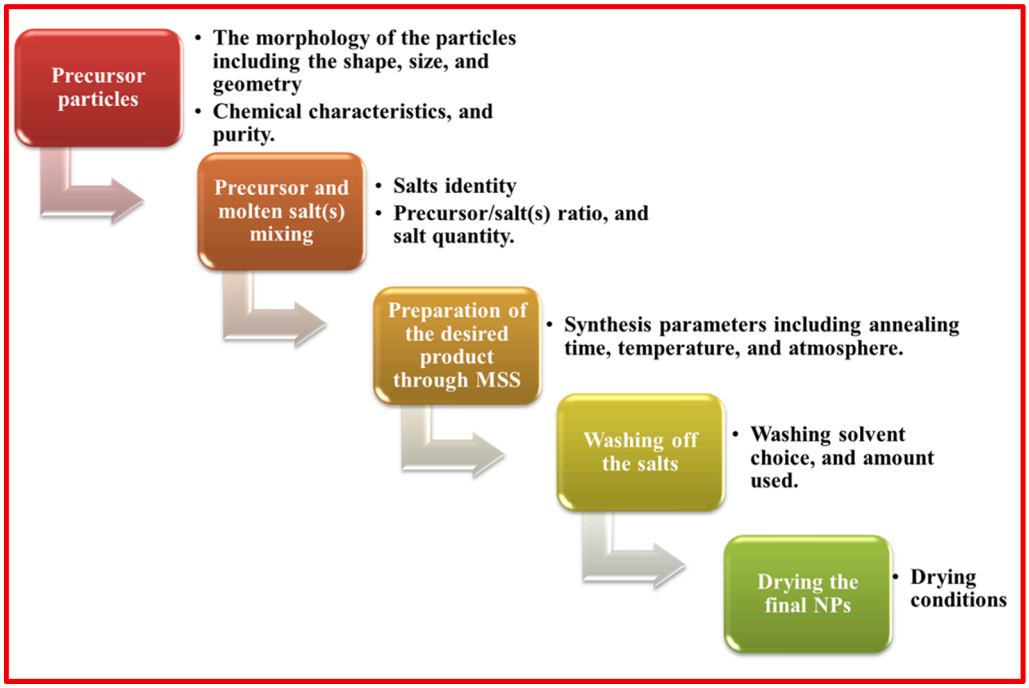

Fig. 5. Flow chart depicting various critical parameters of the MSS method.

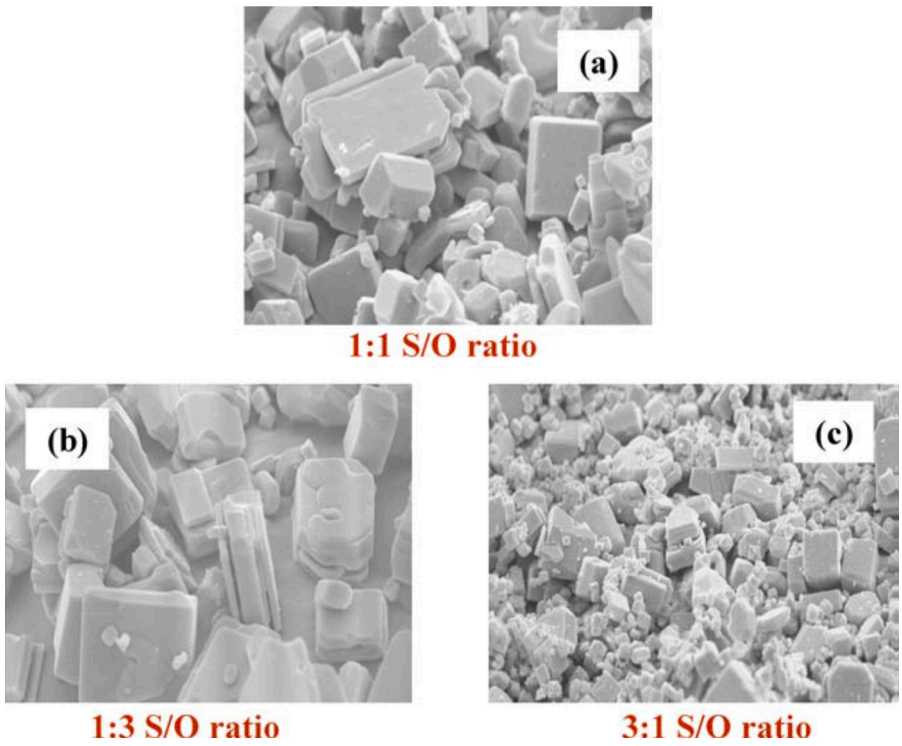

Fig. 6. Effect of salt to oxide ratio on the morphology of the MSS synthesized $Sr_3Ti_2O_7$ [95]. *Copyright 2006. Reproduced with permission from Springer nature.*

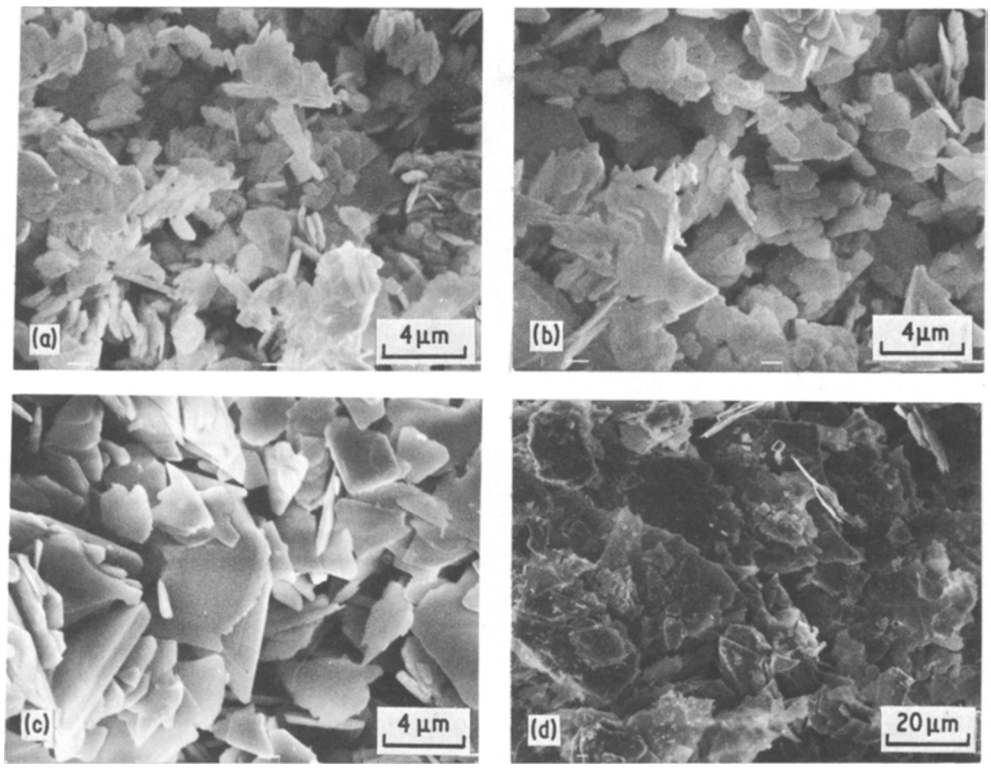

Fig. 7. Morphology of Bi_2WO_6 powder synthesized in chloride flux at a salt/oxide ratio of 1.0 at different temperatures: (a) 650 °C, (b) 700 °C, (c) 800 °C, and (d) 850 °C [94]. *Copyright 1982. Reproduced with permission from Springer nature.*

that with S/R = 1:1, the formed $Sr_3Ti_2O_7$ particles were mostly of platelet morphology with some cubic and tetragonal shape existing as well (Fig. 6a). At S/R = 1:3, $Sr_3Ti_2O_7$ platelets of lower aspect ratio were formed (Fig. 7b). When S/R = 3:1, very fine and small sized $Sr_3Ti_2O_7$ was formed (Fig. 7c).

3.3.3. MSS operating temperature (MOT)

Normally the most suitable crucible to carry out the MSS heating is made of platinum. Considering the cost of platinum, one can also opt for ceramic crucibles such as alumina and zirconia as long as no chemical interactions take place between reactants/products with the crucibles. The criteria of selecting MSS processing time and temperature are decided by the products to be synthesized. The main purpose of heating the salt and precursor mixture is to shorten the diffusion length and increase the transport rate of molecules to react. Heating causes the evaporation of the used molten salts other than possibly the reactants, so it is recommended to cover the crucibles with suitable lid to avoid evaporation and unnecessary contamination. MSS processing time is mostly dictated by the kinetics of chemical reaction occurring in the MSS process and the size/shape of the product molecules. Heating rate is also known to have profound influence on the size of formed particles [92].

MOT should be higher than the melting temperature of salt used in MSS. To have large temperature range of operation; heterogeneous salt system (A + B) having low eutectic temperature is used as discussed earlier also as seen in the case of chloride-carbonate mixed salt for synthesis of $LiMn_2O_4$ [87]. The lists of different halides and oxosalt based molten salt with composition and their melting point is mentioned in Table 4 [23]. MOT basically depends on two main factors: decomposition temperature and vapor pressure of the selected salts. It is better to avoid the salt having high vapor pressure such as $BaCl_2$, CsI and $ZnCl_2$ unless closed systems are used for carrying out the reactions. These salts normally have mixed ionic and covalent bonding character.

Also, the particle size of the powders synthesized by the MSS method is dictated greatly by liquidus temperature (T_l). Below T_l, unreacted precursors get solubilized in the molten salts and precipitate out as byproducts. Further raising the MOT keeps giving more products, and thereby particle size increases. After the reaction is complete, particle continues to grow. Above T_l, all precursors get solubilized in the molten salts and product precipitates on cooling. This precipitation is governed by nucleation followed by supersaturation. Crystal growth is proportional to the degree of supersaturation. In this case, once the nuclei are formed, the growth of particles happens very rapidly until supersaturation vanishes, which results in the formation of large plate-like Bi_2WO_6 with well-defined (010) facets.

Fig. 7 shows the influence of MOT on the morphology of particles at chloride salt/oxide (Bi + W) ratio of 1.0 and annealing time of 1 h. The particle morphology seems to be plate-like in the temperature range of 650–900 °C. The obtained particles are smaller in size when synthesized below 800 °C (Px type) and kept increasing as the temperature was raised and became almost 100 μm (Py) when the synthesis temperature was beyond 850 °C. The effect was found to be similar for the chloride salt/oxide (Bi + W) ratio between 0.25 and 2.0. Both Px and Py particles were formed below and above a certain critical MOT, which was lowered by the increased amount of the fused salts.

Fig. 8a shows the fractional completion for the formation of various ferrite compounds MFe_2O_4 (M = Ni, Zn, Mg) using SSR route and with MSS employing Li_2SO_4-Na_2SO_4 eutectic mixture. It can be seen from this plots that the MSS lowers the formation temperature compared to the SSR route. It is quite interesting to see that $MgFe_2O_4$, $NiFe_2O_4$ and $ZnFe_2O_4$ forms almost at identical temperatures by the MSS method but SSR synthesis of these compounds requires different temperatures depending on the kind of metal ion M^{n+}. The MSS process leads to enhanced reaction rate and at lower temperature because the addition of molten salt increases in the contact area between the reacting species and enhances the diffusion rate which is of the order of 10^{-5}–10^{-8} cm^2 sec^{-1}, much higher than that in SSR route [72,96]. In case of SSR route, the diffusion rate is on the order of 10^{-18} cm^2 sec^{-1}. For SSR, the contact area is also small because the product formation only takes place at the point of contact of two different reactant. Surfaces of the reactants in the MSS are shielded with salt-melt and they become available to the reaction.

The mechanistic view of material synthesis using the MSS and SSR route has also been well-explained in case of $BaTiO_3$ by Hayashi et al. [97]. Both methods could successfully produce rod-shaped $BaTiO_3$ with chloride based MSS at 700 °C and by SSR at 1000 °C. It should be emphasized here that the dissolution rate of the precursors in molten salts also plays a very important role, which determines

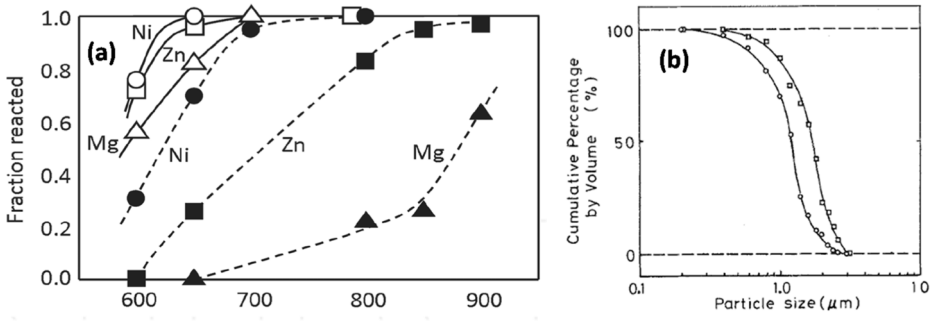

Fig. 8. (a) Formation of MFe_2O_4 (M = Ni, Zn, Mg) with (solid lines) and without (dashed lines) molten Li_2SO_4-K_2SO_4 salt, heated for 1 h [98]. *Copyright 1980. Reproduced with permission from Japan Chemical Society.* (b) Size distribution plot of $BaTiO_3$ rods synthesized using the MSS and SSR routes [97]. *Copyright 1986. Reproduced with permission from Springer Nature.*

the morphology of the products. When the dissolution rate of TiO_2 is less than that of $BaCO_3$, $BaTiO_3$ rods is formed. In the MSS process, Ba^{2+} ions diffuse though the $BaTiO_3$ layer formed on the surface of TiO_2, which leads to the formation of $BaTiO_3$ rods. On the other hand, spherical/cubic/equiaxed $BaTiO_3$ particles are formed when the dissolution rate of TiO_2 is higher than that of $BaCO_3$. This was attributed to conversion of anatase TiO_2 to equiaxed rutile under thermal treatment in molten salt before it could react with $BaCO_3$. On the other hand, the SSR between $BaCO_3$ and TiO_2 proceeds via the diffusion of Ba^{2+} ion resulting in the shape of $BaTiO_3$ similar to that of TiO_2. Fig. 8b shows particle size distribution in the case of both SSR and MSS routes. It was found that the fraction of smaller particles is larger in case of the MSS. Hard agglomerates was found from the SSR route whereas the inclusion of molten salt between the solid precursors avoids such bonding by the MSS process.

3.3.4. Removal and solubility of molten salt

Once the heating is done and final product is formed; they need to be thoroughly washed to get rid of salt. The most preferred solvent used for washing in MSS is water. That's why it is a prerequisite to use water soluble salt in MSS. The preferred choice of salts are metal nitrates, chlorides and sulphates due to their high solubility in water. In most cases, 2–3 times of washing are needed for removing all of the remnant salt. But some time repetitive washing is required to get phase pure materials because the salts may get adsorbed on the surface of product particles. Chloride ion is the most notorious of all and sometime hot water washing is needed to get rid of that. Once done with washing, supernatant is decanted off and the remaining powder is kept for room temperature drying. Sometime washing with low surface tension solvent such as acetone is very beneficial as it helps in avoiding formation of agglomerated products.

Rate of reaction is highly proportional to the solubility of molten salt as it determines the amount of precursor that can be accommodated by salt. For metals, neutral precursor, and gaseous molecules molten salts served as an excellent solvent at high temperature. Solubility of salt melts in case where only the van der Waals interaction exists is dependent on extent of free volume available during the solid to liquid transition. In most of the case, there exists higher order of chemical interaction via acid-base or through metal ion coordination.

As far as metal halide salt is concerned most of the metals are soluble in their halides and are completely miscible above a specific temperature. The solubility depends on many factors such as atomic size, electronegativity, polarity etc. For elements in the same group, it increases with the increase of molecular weight. The solubility follows the trend of $SrCl_2$ (25 mol%) > $CaCl_2$ (16 mol%) > $MgCl_2$ (1.1 mol%) at 1000 °C [33]. The number of electrons in the valence shell also dictates the solubility of some metal ions: the ones with higher valence state exhibit higher solubility. The one which display intermediate oxidation state such as rare earth halide results in formation of sub-halides. Structure of the metal–metal halides systems also plays a very important role in dictating the solubility. Molten metals exist in the form of small droplets in the salt melt in case of system like $Ba/BaCl_2$, resulting in stable colloidal solution. Based on conductivity measurement, it was confirmed that molten metals get ionized into metal ions and free electrons in many rare earth halide–metal systems. System exhibits transition from delocalized to localized electronic states as the metal ion content goes down [99–101].

Most of the metal oxides are soluble in metal salt at high temperatures which can be understood from the concept of hard–soft acid–base (HSAB) theory [77–79]. Based on this theory, hard species (such as small, highly charged and weakly polarizable ions) like to bind with hard ones and soft species (such as big, lowly charged and easily polarizable ions) with soft ones. Molten salts are mostly soft in character, so they prefer interacting with soft/polarizable reactant. The fact that MgO is hard in character finds it difficult to get dissolved in binary/multinary chloride systems (<0.05% at 800 °C). On the other hand, softer CaO easily dissolves in $CaCl_2$ (solubility > 15% at 800 °C). Similarly, SiO_2 is also difficult to solubilize in metal halide salt due to opposite nature of Silicon and chloride center. To tackle such situation, it is better to use metal fluoride as molten salt due to strong nucleophilic character of fluoride ion. In fact, silica easily gets dissolved in metal fluoride unlike chlorides and bromide. So, we can pin-point that the solvation chemistry in salt melts is rather cumbersome, but the old adage "similia similibus solvuntur" (Latin phrase which means "similar substances will dissolve similar substances") works perfectly in most cases.

3.4. MSS: Pros and Cons

3.4.1. Advantages of MSS

Unlike SSR with slow diffusion of the reactants, the MSS method endows reactions at lower temperatures with faster mass transfer transport promoted in the liquid phase by convection and diffusion [102]. MSS method also provides the facility of using salts with the nature to dissolve in water, which allows an easy way to purify final products [23]. Even though the MSS method may be not well-known in the nanoscience community, it provides several advantages. These advantages included simplicity, reliability, scalability, generalizability, and environmental friendliness, cost effectiveness, relative low synthesis temperature, free agglomeration of NPs with clean surface, etc. [14].

3.4.1.1. Simplicity. The MSS method provides an easy way to make functional materials. It can be conducted within common laboratories without requiring sophisticated instrumentation. In most cases, the synthetic steps can be handled in open air with the stability of the materials used without the need to use a glove box.

3.4.1.2. Reliability. The MSS method can generate high quality and pure products once all initial synthetic parameters are adjusted and optimized. It is a reliable route to make high quality final materials.

3.4.1.3. Scalability. The attribute to make large quantity of products with specific size and shape characteristics is a vital aspect of synthesis methods. The MSS method has the capability to generate large amount of product depending on its usage, either for laboratory, research or industrial purposes. By manipulating the stoichiometric value during the initial stage, one can take into account of the production amount of final products. The MSS method provides the ease of scalability which is an important feature at the level of industry mass production [29,103].

3.4.1.4. Generalizability. One of the best features of the MSS method is the fact that it can be utilized to synthesize a variety of structural phases with different compositions. This feature makes the MSS method a generalizable technique suitable to make simple and complex metal oxides. It has been reported to successfully synthesized perovskites (ABO_3) [29,104–107], spinel (AB_2O_4) [108,109], pyrochlore ($A_2B_2O_7$) [48,110–112], and orthorhombic structures ($A_2B_4O_9$) [113–115]. More specifically, these nanomaterials include ferrites [116], titanates [117], niobates, mullite, aluminum borate [118], wollastonite and carbonated apatite. In addition, the MSS method has been used to tune the morphological aspect of the produced nanomaterials such as nanospheres [48], ceramics powder bodies [49], nanoflakes [119], nanoplates [118], nanorods [120], and core–shell NPs [121], depending on synthesis conditions and crystal structure of the products.

3.4.1.5. Environmental friendliness. The MSS method is an environmentally friendly approach to make nanomaterials without the use of toxic chemicals compared to traditional methods that use large amounts of organic solvents that can cause environmental issues. The MSS method reduces the generation of waste and there is no byproduct formation [14]. Lastly, the use of renewable materials to make desirable final products allows the minimization of energy used and therefore provides a green pathway to generate high quality products.

3.4.1.6. Relative low synthesis temperature. Because the product formation temperature in the MSS process is relatively low, it has been considered as one of the most suitable choices for nanomaterials synthesis owing to its low thermal energy consumption. Compared to other methods such as conventional solid-state reaction [122] and sol–gel combustion reaction [123], the MSS method provides a more effective way to make nanomaterials at relatively low temperature.

3.4.1.7. Cost effectiveness. The MSS method provides a cost-effective approach because it does not require harsh and costly reactants. The used molten salts as a solvent are generally washed away with water which reduces the cost of purification. Also, the MSS method does not require special instrumentation that required special training to operate. Simple glassware and furnaces are normally used to make both simple and complex metal oxides.

3.4.1.8. Agglomeration free with clean surface and well-defined shape. As the molten salt media have high ionic strength, low viscosity, and low density, the NPs that are formed from the MSS process are well dispersed [14]. For the benefits of the readers, we are hereby comparing the physicochemical properties of one of the frequently used molten salt NaCl along with 0.1 M NaCl aqueous solution (Table 5). Also, unlike colloidal and most hydrothermal synthesis methods, no protection layer is needed to be added on the particle surface to prevent their growth and agglomeration. The following material As a comparative example, $SrTiO_3$ powders were prepared using both solid state and MSS methods (Fig. 9) [124]. Specifically, for the MSS synthesis of $SrTiO_3$, reactions were performed at 1000 °C using LiCl, NaCl, KCl, and $SrCl_2$ as the molten salt media in a 1:1 salt-to-reactant molar ratio. The alkali metal halides are unreactive, acting purely as solvents and avoiding the formation of undesired by-products (i.e., $ATiO_3$, A = Li, Na, K). The metal halides used act as mineralizers. The varied cation sizes of the molten salts affect their melting points, viscosities, supersaturation of the solvent system, so well-defined particles with various defined morphologies were produced. On the other hand, the SSR route produced irregularly shaped particles that are aggregated to ~5–15 μm.

3.4.1.9. Homogenous particles and narrow size distribution. Compared to other high temperature synthesis routes, the MSS method accelerates the rate of materials transport and the forms homogenous final products in terms of both chemical composition and size. To demonstrate the homogeneity of chemical composition clearly, Hayashi et al. have synthesized (Ni, Zn)Fe_2O_4 powders by MSS and solid state route [126]. They checked whether the compositional powders ($NiFe_2O_4$ and $ZnFe_2O_4$) were reacted by MSS using Li_2SO_4-Na_2SO_4 salt and by the solid-state reaction route at 900 °C for 4 h. Magnetic measurement was carried out as a function of nickel concentration on both the samples to elucidate Curie temperature (T_c) to see the compositional fluctuation in the obtained (Ni, Zn)Fe_2O_4 (Fig. 10) [126]. They showed that the distribution plot from the particles made by the solid state route without the molten salt looks broad which suggests large compositional fluctuation compared to the sample made by the MSS method where Li_2SO_4-Na_2SO_4

Table 5
Physicochemical properties of molten NaCl at 850 °C and 0.1 M NaCl(aq) solution at room temperature [125].
Copyright 2016. Reproduced with permission from Springer Nature.

	Molten NaCl	NaCl solution
Ion concentration (M)	26	0.1
Density (g/cc)	1.53	1.00
Electrical conductivity (S cm^{-1})	3.6	0.107
Viscosity (cP)	1.2	1.01

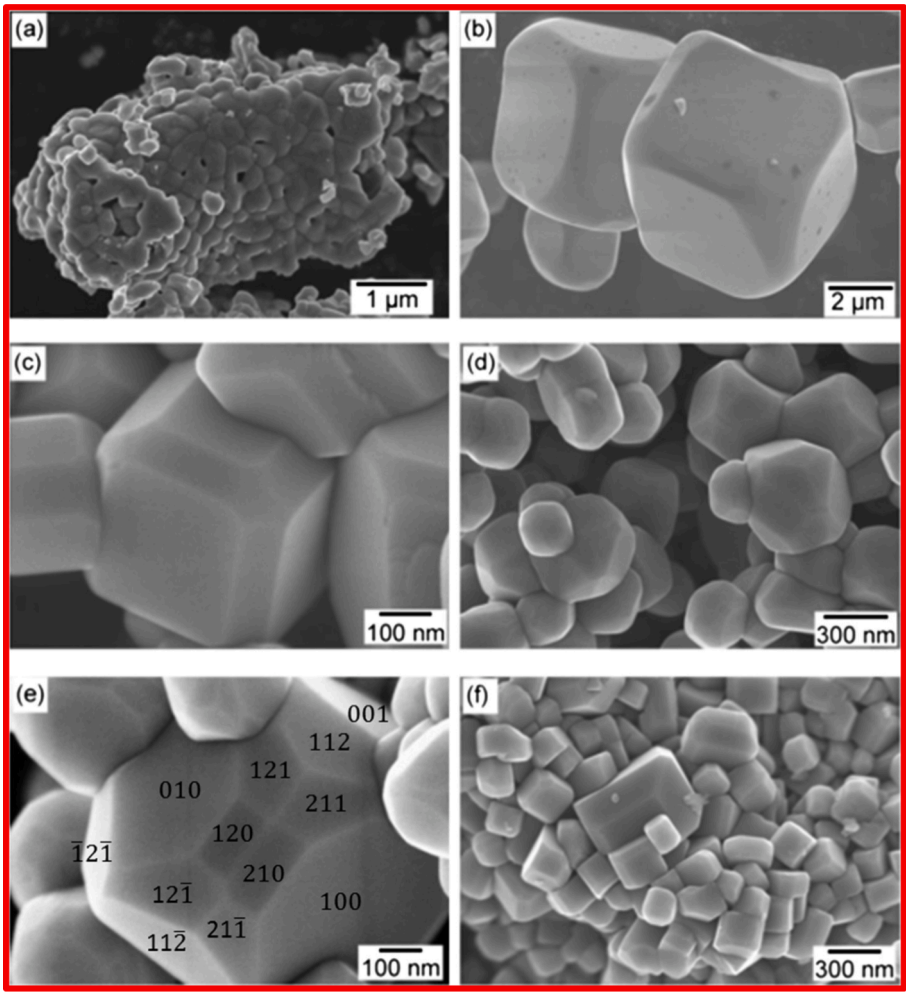

Fig. 9. SEM images of $SrTiO_3$ prepared by (a) the conventional SSR method and the MSS method using molten salts of (b) LiCl, (c) NaCl, (d and e) KCl, and (f) $SrCl_2$. The exposed crystal facets are labeled in (e) with the appropriate Miller indices of KCl [124]. *Copyright 1985. Reproduced with permission from Royal Society of Chemistry.*

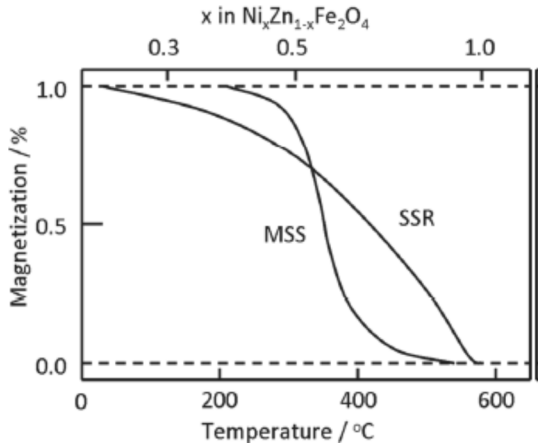

Fig. 10. Distribution of the Curie temperature in $(Ni,Zn)Fe_2O_4$ powders prepared by the MSS and SSR routes, heated at 900 °C for 4 h [126]. *Copyright 1985. Reproduced with permission from American ceramic society.*

salt was used.

In terms of the homogeneity of particle size and morphology, the surface of formed particles is well covered by molten salt during the MSS process, which avoids neck formation between product particles and leads to low degree of agglomeration. On the other hand, high degree of agglomeration happens in SSR route due to the concurrent occurrence of sintering and formation of products [127]. Theoretical aspect to explain the difference in the product characteristics formed by the MSS and SSR routes has been well-described by Boltersdorf et al. [88]. High temperatures annealing is very important criterion in the SSR route to get phase-pure products as it increases the rate of reaction and diffusion length. Diffusion kinetics is often the limiting step in the SSR route as reactions happen at the solid–solid interface in the absence of any solvents. Palletization is often done to increase the surface contact among the SSR reactants. High temperature treatment, repetitive grinding, frequent palletization in the SSR often result in non-uniform particles with irregular shapes and large degree of agglomeration. Some of the recent investigations on the kinetic study of the SSR and MSS routes by x-ray diffractions (XRD) measurements has thrown remarkably interesting results. XRD results clearly pinpointed the enhanced rate of chemical reactions and crystal formation in case of the MSS compared to the SSR. In fact, it was found that the reaction time for product formation in case of several metal oxides such as $NaTi_2O_4$, $CuNb_3O_8$, and $RbCa_2Nb_3O_{10}$ has been reduced from 24 to 96 h by the SSR route to as low as 15 min for the MSS method [128–134].

In case of the MSS, molten salts cover the surface of reactant species and thereby prevents extensive agglomeration unlike the SSR route. Surface protection further helps in achieving high degree of homogeneity and anisometric particle growth which leads to well-defined uniform particle distributions by the MSS method. The presence of molten salt during the product formation further leads to uniform particle with well-defined facets and few grain boundaries typical of single crystals. Extended heating in molten salt leads to crystal growth via the Ostwald ripening. Modulating the growth rate of metal-oxide surfaces can lead to materials with cubic, octahedron, or cuboctahedron morphologies. Such morphologies can be clearly visualized in the cases of $Pb_3Ta_4O_{13}$ (Fig. 11) when the growth rates along the [94,105], or intermediate directions are predominant for cubic systems, respectively.

3.4.2. *Disadvantages of MSS*

Selected salts for MSS processes may directly involve in reactions to form intercalates, solid solutions or other byproducts, and eventually affect the purity of the final products. It is desirable that the selected salts act as pure solvents only and do not react with the reactants and the products. Specifically, molten salts of borates, phosphates and silicates tend to form vitreous phase with reactants, so

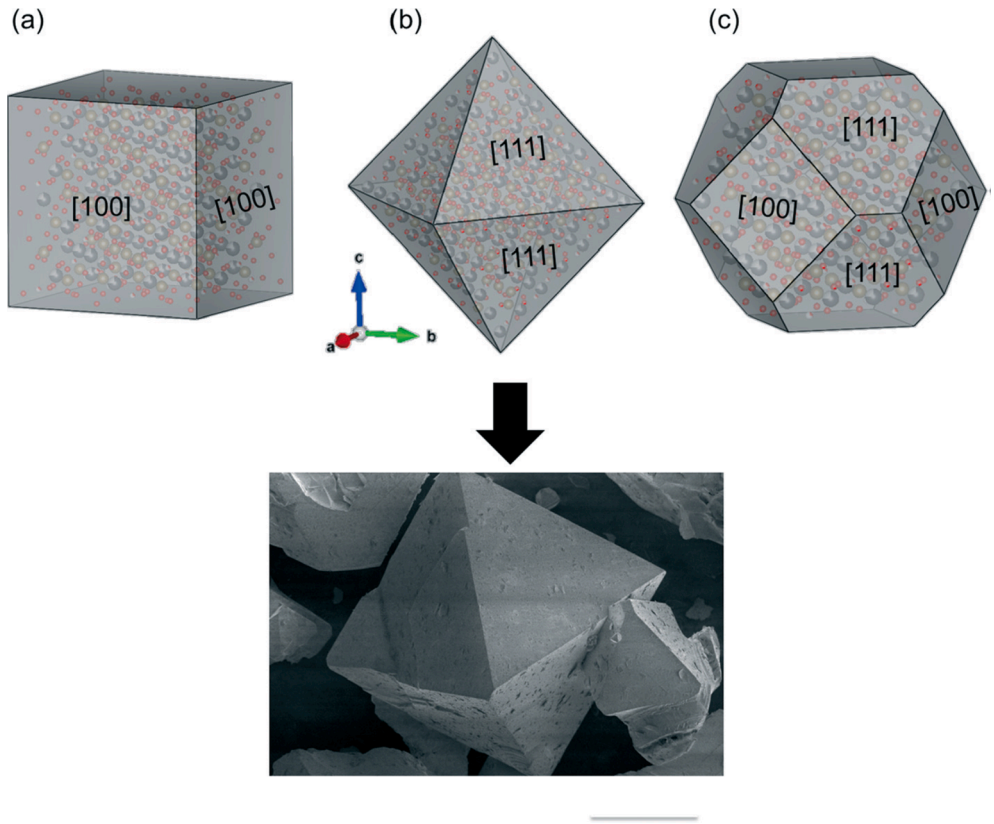

Fig. 11. Depiction of (a) cube, (b) octahedron, and (c) cuboctahedron particle morphologies from cubic crystal structures (e.g., Fd-3m), as shown by the SEM image for $Pb_3Ta_4O_{13}$ on exposure of the [94,105], and [94]/[105]. faces, respectively [88]. *Copyright 2015. Reproduced with permission from Royal Society of Chemistry.*

they should be prevented in many MSS processes. For this reason, alkali metal chlorides or nitrates which are chemically inert and have larger electrochemical window could be suitable salts to synthesize metallic and non-metallic products by the MSS method.

The strong interactions of the used molten salts with the products could be one of the major potential drawbacks of the MSS method. This disadvantage must be considered carefully in controlling the quality of the as-obtained products. The final stage to separate products from the used salts is crucial and mostly performed by washing with water. However, small amounts of salts or their ionic components may remain on the surface of the final product due to the intrinsic interactions of the used salts with the products. It is important that the molten salts used are highly water soluble.

The expense of the salts used could add up and increase the overall cost of MSS processes considering the high percentage of salts applied in the salt and reactant mixture, especially for large scale production and if they are not recovered and recycled. The preferred salt systems are composed of cheap and abundant elements, e.g. cheap salts like NaCl and KCl. On the other hand, Li salts are expensive and should only be applied for high value products. The development and implement of salt recycling methods in the MSS processes becomes important and economically necessary.

The MSS method could be potentially hazardous even though metallic halides (except fluorides) as selected molten salts are non-toxic and direct exposure to skin does not lead to any harmful effects taking into the consideration of all safety regulations. However, if handling of metal fluorides as used molten salts is necessary, extreme attention should be implemented due to the fact that they can cause severe damage to human tissues. If acidic salts such as $AlCl_3$ and alkalis like KOH are used, close awareness is required as these substances are corrosive. In addition, heavy metal salts, such as $BaCl_2$, should also be processed with care as they are harmful to the human body [23]. Moreover, at the stage when all salts are melted, the melts can present a potential danger due to the high temperature and gases such as NO_2 and SO_2 possibly released from the process. Thus, it is a good practice to perform MSS reactions with proper and continuous ventilation or in a fume hood.

Also, the choice of molten salt should be such that is does not react with reaction vessels such as crucibles. For instance, hydroxides of alkali- and alkaline-earth-metal hydroxides and PbO fluxes are extensively explored to solubilize several reactants owing to their high oxobasicity. However, it was found that they corrode Al_2O_3 and Pt crucibles which ultimately affects the purity of the final products by Al/Pt contamination [88,135].

3.5. Advanced MSS methods

In order to synthesize materials with unusual oxidation state, metastable phases, improved purity, and uniform particles with defined structure and composition, there are several modifications of the conventional MSS method such as topochemical MSS, kinetically modified MSS, aerosol based MSS, etc. [102,136].

3.5.1. Aerosol MSS

Aerosol-molten-salt-synthesis (AMSS) is a new approach that provides a spatially and temporally confined crystal growth in molten salts. It uses molten salt droplets to achieve nanoscale materials [137–139]. It can be thought as a new MSS method confined within

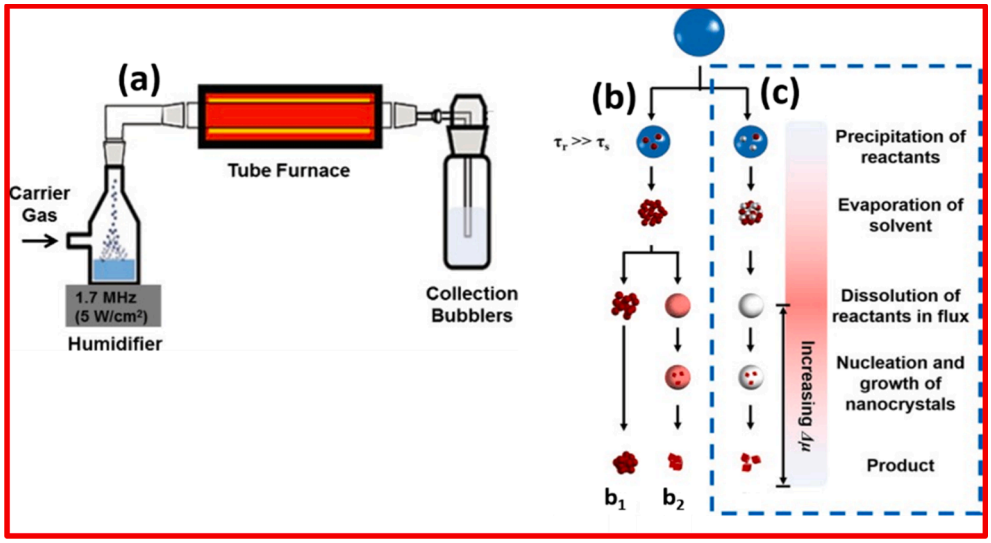

Fig. 12. (a) Schematic lab scale spray-synthesis setup. Schematic of the various liquid-to-solid conversion routes observed in ultrasonic spray. Route (b) displayed situation where the reactant diffusion rate $\tau_r \gg$ evaporation rate of the solvent τ_s with typical polycrystalline aggregates obtained (b_1 and b_2) [141]. *Copyright 1993. Reproduced with permission from Taylor and Francis.* Route (c) depicts flux-mediated crystal growth. The coloration adjacent to pathway (c) is a schematic of the temperature profile in the reactor, where red and blue represent high and low temperatures, respectively [140]. *Copyright 2015. Reproduced with permission from John Wiley and Sons.* (For interpretation of the references to colour in this figure legend, the reader is referred to the web version of this article.)

micro sized aerosol droplets which render unique pathway to control shape specially for compositions that are difficult to make at low temperature [140]. In a typical AMSS setup (Figure12a), an ultrasonic nebulizer creates water droplets containing precursors. The droplets produced by the nebulizer are transported using a steady flow of gas to a tube furnace where solvent evaporation, solute precipitation, precursor decomposition, reactions, and product densification take place. After this step, the final product is then collected in water vessels. Other collection methods have also been implemented depending upon specific needs [141,142]. In the absence of a fluid droplet phase, polycrystalline microspheres are the most common resultant powder [143]. Moreover, one can take care of necessary conditions required for optimum crystallinity in final products such as supersaturation, and lower barriers to diffusion can be achieved by proper thermal conditioning.

Compared to conventional SSR route, higher mass transport and heat diffusion rates in smaller volume lead to product formation in shorter time under relatively milder conditions. Mostly polycrystalline microspheres are formed from processes of droplet evolution in case of spray drying or liquid → solid state conversion (Fig. 12b) [141]. These droplets can be biased to molten salts and mediated properly to align crystal growth (Fig. 12c), especially by judiciously selecting precursors whose decomposition products can easily

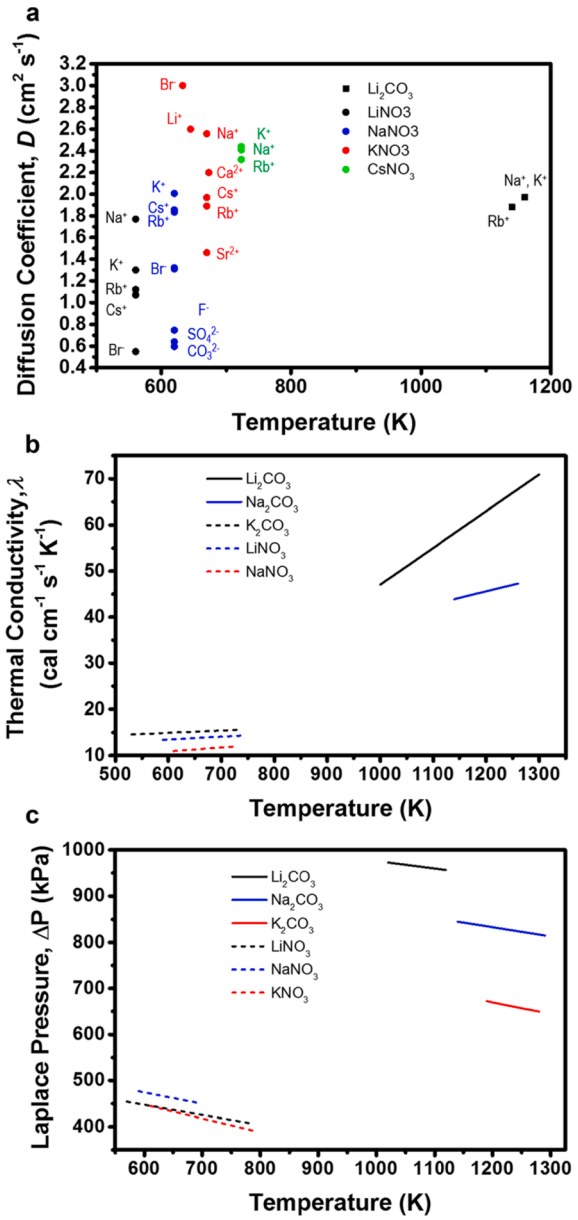

Fig. 13. Variations of (a) diffusion coefficient, (b) thermal conductivity, and (c) Laplace pressure for several alkali metal nitrate and carbonate molten salts for 1 mm spherical droplet and an external pressure of 1 atm [140]. *Copyright 2015. Reproduced with permission from John Wiley and Sons.*

dissolved in the molten salts. In such cases, molten salts themselves can prevent agglomeration of individual crystals forming within the droplets.

Crystal growth in such case is driven by chemical potential difference between solution (parent phase) and new crystal (daughter phase). Such driving force in case of solution chemistry is termed as supersaturation. The degree of supersaturation in case of AMSS can be modulated via choice of flux, flux/precursor ratio (FPR), MOT, and residence time ($T_{res.}$) [140].

Liquid state of ionic melts can be modeled in terms of electrostatic interaction between the cations and anions and also the polarizability of the solute and solvent [144,145].

Molten oxosalts such as $NaNO_3$ and Na_2CO_3 should be considered as possessing basic characteristics. Their property depends on its ability to donate oxygen, similar to what has been depicted in Eq. (1).

Oxygen donating ability of molten oxosalts can be further adjusted by tuning its basicity which consequently modifies the system solubility [76]. Compared to the conventional MSS wherein water is usually avoided, nebulization process in the AMSS involves an aqueous solution of precursors. Consequently, droplets produced in the AMSS absorb moisture. For example, halide salts used in the AMSS can be hydrolyzed to their respective acids and oxides at elevated temperature [146].

In case of the MSS for bulk material; polyhedral crystal growth happens when FPR $\geq$ 8. At this FPR value, supersaturation is high enough for nucleation but small enough for lowering diffusion assisted growth.

As discussed above, the crystal growth in the AMSS depends on supersaturation degree which in turns also depends on the residence time (flow rate and heating zone length). Residence time in the AMSS can be adjusted by modulating the rate at which gas flows in furnace. For tubular furnace (Fig. 12a), it is given by Eq. (4) [143]:

$$T_{res.} = \frac{0.06\pi R_t^2}{Q}\left(\frac{T^0}{T}\right)\frac{1-y_w}{1-y_w^0} \tag{4}$$

where R_t is the tube radius in cm, Q is the inlet flow rate in L/min, T is the air temperature in Kelvin, y_w is the mole fraction of water vapor in air. Residence time varies from one system to another depending on the thermal conductivity of tubular furnace materials, the size of the precursor, and the crystal growth regime of target product. Normally, the operational temperature is kept more than 100 °C above the melting point of designated flux and the residence time is kept longer than usual to allow for growth of the particle. Nucleation and growth of particles in the AMSS can happen in the hottest or coolest zone depending on the degree off supersaturation of the droplets in the AMSS (Fig. 12c).

Compared to lower cooling rate in conventional MSS, lower residence time in hot zone results in large temperature gradients which can lead to supercooling and crystal growth.

The morphology of the crystals formed in the AMSS ultimately depends on the physicochemical properties of the molten salt used as it dictates the operation temperature and residence time [147]. Fig. 13 shows the physiochemical properties such as the diffusion coefficient, thermal conductivity and Laplace pressure of various alkali metal nitrate and carbonate molten salts. Optimum thermal conductivity of the flux in particular is very important to achieve positive solid–liquid thermal gradient which promotes smooth front surface growth and is extremely desirable in case of polyhedral crystal. Laplace pressure is also very important because of the fact that droplet dimension in the AMSS usually lies in the range of 100–200 nm.

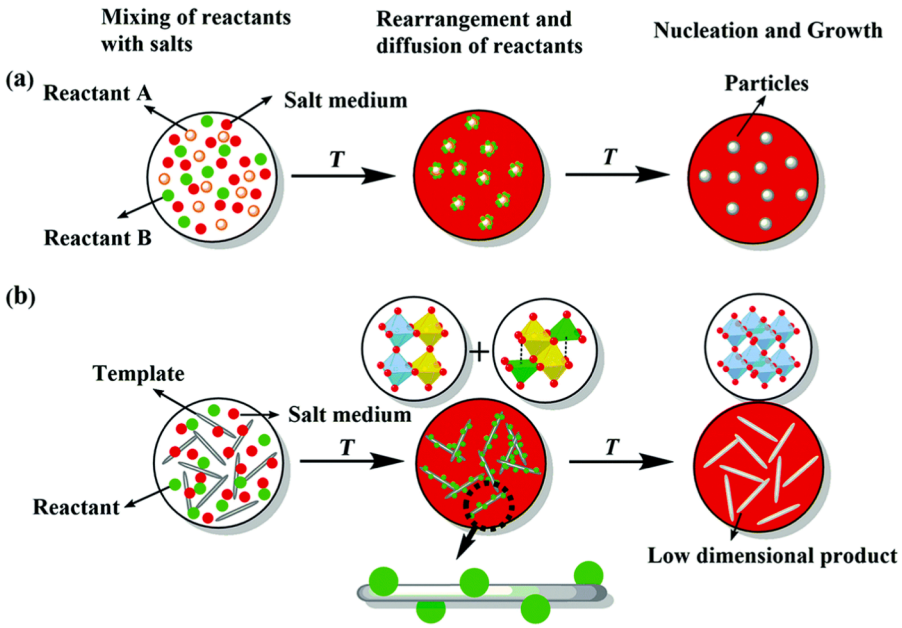

Fig. 14. Schematic showing the mechanisms of (a) the conventional MSS and (b) TMSS routes [171].

There have been many studies of the AMSS given on enabling synthesis conditions which induce flux-mediated crystal growth to produce shape-defined NPs, mostly in case of complex metal oxides [88,148–150]. Selective growth particularly for complex metal oxide NPs requires several critical steps such as (i) low reaction temperatures, (ii) shorter reaction duration, (iii) desired shape of primary precursor, and (iv) enhanced rate of dissolution of precursors by judiciously adjusting the flux conditions [88]. Some of the synthesized examples include $Cu_2Nb_8O_{21}$ [151], $ATiO_3$ (A = Sr, Ba, Pb) [71,152–156], $ANbO_3$ (A = Li, Na, K) [25,157,158], $LaMnO_3$ [153], $BaTi_2O_5$ [159], Sr_2SbMnO_6 [160], and several Li-ion battery materials [161–165].

3.5.2. Topochemical MSS

The performance of materials to a large extent depends on their structure and morphology. On the other hand, the shape of crystalline materials depends on their internal structure. For instance, system with cubic crystals leads to isotropic materials. Through the conventional MSS method, it is difficult to achieve targeted morphology of the product. Using equiaxed regular perovskite material, it is difficult to synthesize anisotropic particles via the conventional MSS. Here as discussed in Fig. 3, precursors disperse, dissociate, rearrange and diffuse inside molten salts [166]. The product morphology is decided by the low energy minimum shape decided by the surface and interfacial energy between precursor particle and molten salt [14]. If asymmetric reactants with feasible solubility is selected as a template for the MSS route, the morphology of final products will have recombination of the local basic units, that is what is known as topochemical MSS (TMSS) method.

The TMSS method combines the conventional MSS method and the topochemical method, associated with the use of localized solid-state compound transformations *via* the exchange, deletion, or insertion of individual atoms [167]. It prepares pure and morphologically-controllable samples at a moderate temperature in a short soaking time [102]. Similar to common MSS method, the shape and size of its products are controlled by appropriate choice of raw materials, salts, synthesis temperature and reaction time. On the other hand, the TMSS method does not require all precursors to be soluble while the MSS method most requires high solubility of precursors. In the TMSS, the morphology of products comes directly from solid-state raw materials. Specifically, particular solid-state raw materials as precursors acting as templates should be refractory or micro-melting in the molten salts. Schematics to illustrate the

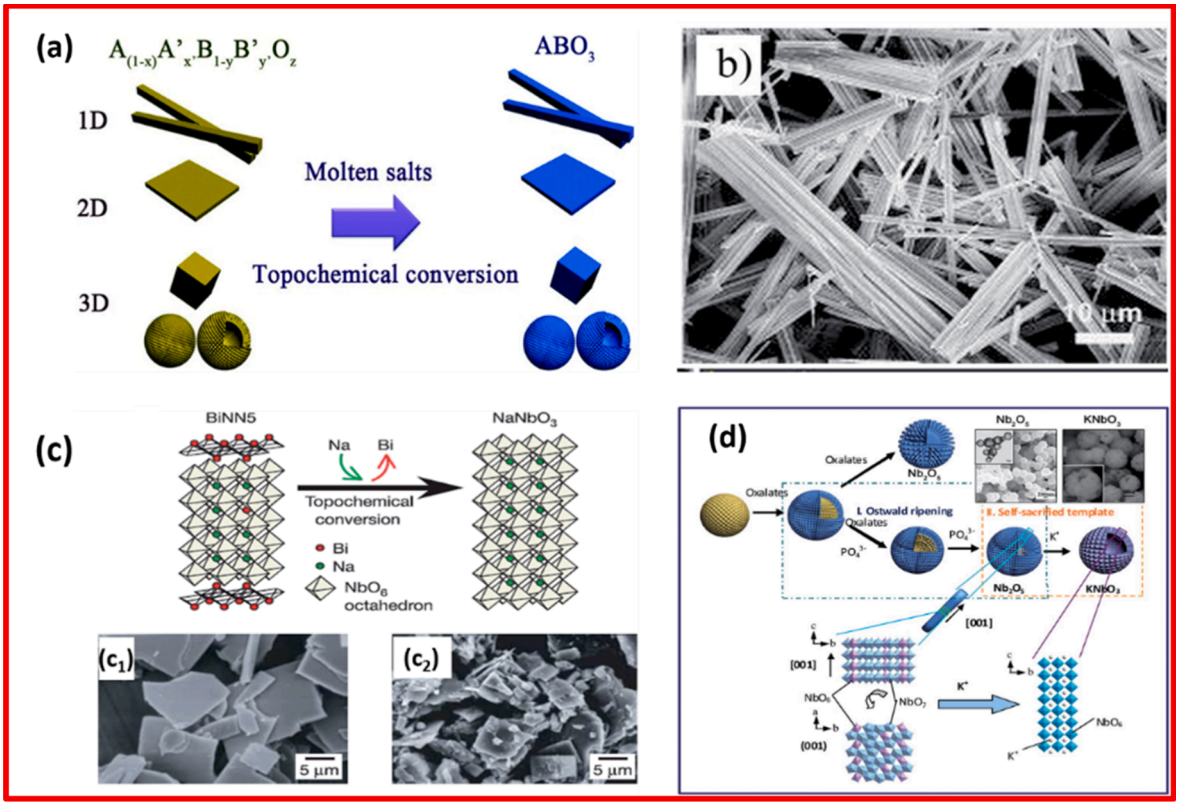

Fig. 15. (a) The schematic illustration of the TMSS method [102]. *Copyright 2010. Reproduced with permission from the Royal Society of Chemistry.* (b) SEM images of potassium niobate nanowires prepared by the TMSS method [168]. *Copyright 2007. Reproduced with permission from American Chemical Society.* (c) Schematic diagram of topochemical conversion from the bismuth layered structure BiNN5 particles to plate-like $NaNbO_3$ particles. This figure also reflects their crystal structure. (c_1 and c_2) SEM images of layered BiNN5 and $NaNbO_3$ [169]. *Copyright 2004. Reproduced with permission from the Nature Publishing Group.* (d) Formation processes and structure evolution of the $KNbO_3$ hollow spheres and Nb_2O_5 solid spheres. The insets are the SEM images of the Nb_2O_5 and $KNbO_3$ spheres [170]. *Copyright 2013. Reproduced with permission from the Royal Society of Chemistry.*

mechanism of both the MSS and TMSS routes are shown in Fig. 14a and b, respectively.

The schematic illustration of the involved TMSS method is also summarized in Fig. 15a. The equilibrium of the TMSS method is represented by the following reaction:

$$A_{(1-x)}A'_{x}B_{(1-y)}B'_{y}O_{z}\ \ (as\ \ template) + xA^{f+} + yB^{m+} \xrightarrow{Molten\ \ Salts\ \ (TMSS)} ABO_3 + x'A'^{f+} + y'B'^{f+} \quad (5)$$

where $0 \leq x, x', y$ and $y' \leq 1$ and z is a positive integer.

The TMSS method is arguably one of the best ways for controllable synthesis of functional materials by exploiting localized solid-state raw materials. In some studies, pure samples could be obtained with controllable morphology in a few minutes. This type of topochemical method based on the MSS process has been carried out to prepare various perovskite compounds such as sodium and potassium niobates with one-dimension (1D), two-dimension (2D), and three-dimension (3D) morphologies as shown in Fig. 15b–d, respectively.

Cheng-Yan Xu et al. have synthesized niobate nanorods using the TMSS approach [168]. The authors initially synthesized $K_2Nb_8O_{21}$ nanowires using the conventional MSS method with Nb_2O_5 as the reactant in KCl flux at 1000 °C. Then, utilizing the TMSS concept, the Xu group synthesized 1D $KNbO_3$ nanorods (Fig. 15b) using the preformed $K_2Nb_8O_{21}$ nanowires as the template in NaCl flux at 800 °C.

The TMSS approach has also been found to be an excellent technique for the synthesis of 2D materials wherein electrons are free to move in two dimensions such as thin films, superlattices and quantum wells. Perovskites in platelet-like morphology is very difficult to achieve via the conventional MSS or hydrothermal method as perovskite compounds regularly grow into equiaxed particles. Using the concept of TMSS, platelet-like morphology could be easily achieved for $NaNbO_3$ perovskite [169]. $Bi_{2.5}Na_{3.5}Nb_5O_{18}$ (BiNN5, Fig. 15c1) platelets were initially synthesized using the conventional MSS method in NaCl flux at 1100 °C, and then following the TMSS concept (Fig. 15c), $NaNbO_3$ in platelet-like morphology (Fig. 15c2) was synthesized using the BiNN5 platelet as the template and Na_2CO_3 as the reactant in NaCl flux at 950 °C.

The extraordinary potential of the TMSS approach was further demonstrated in the synthesis of $KNbO_3$ hollow nanospheres from Nb_2O_5 hollow spheres as template (Fig. 15d) [170]. This process employed KCl as the molten salt by involving the diffusion of K^+ ion inside the Nb_2O_5 hollow spheres. The product formation in this case was realized via breaking old bonds, bond rearrangement, rebonding, and finally the formation of new bonds. Both the NbO_6 and NbO_7 units in the Nb_2O_5 template were edge-shared whereas

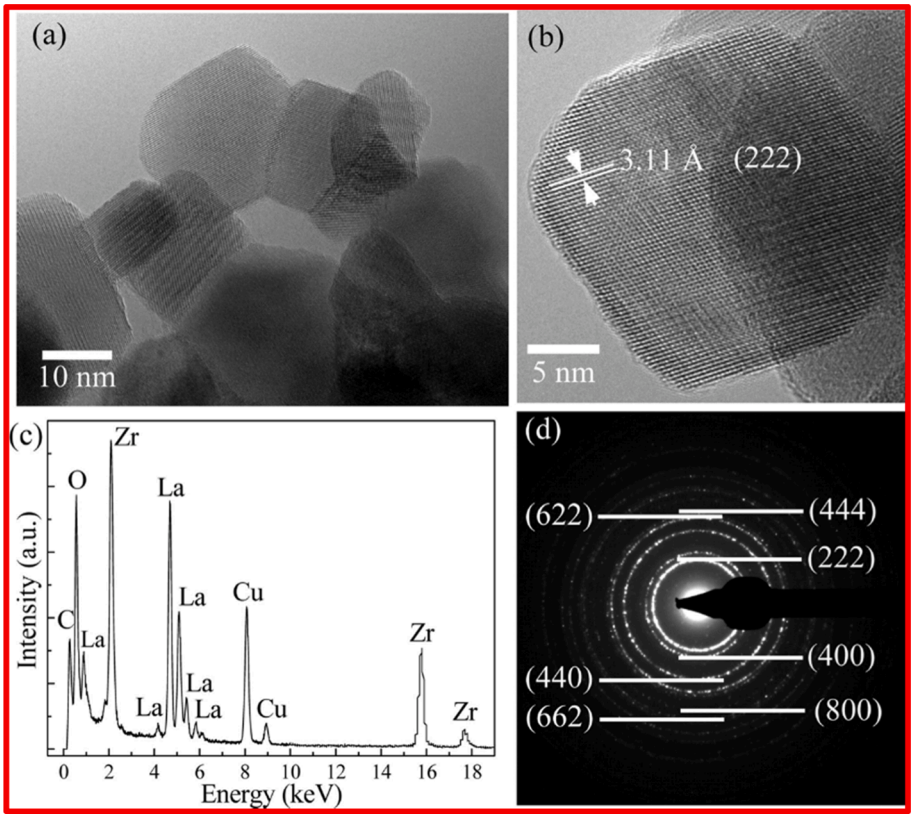

Fig. 16. TEM characterization of the $La_2Zr_2O_7$ nanocrystals synthesized by the KMMSS method: (a) TEM image, (b) HRTEM image, (c) EDS spectrum (the Cu and C peaks originate from the TEM grid), and (d) selected area electron diffraction pattern [48]. *Copyright 2009. Reproduced with permission from the American Chemical Society.*

NbO_6 units in $KNbO_3$ perovskite are corner-shared along the *a*, *b*, and *c* axes. Therefore, edge-shared NbO_6 and NbO_7 in the Nb_2O_5 template tend to transform into corner-shared modes to achieve the lowest energy state. The local recombination of the NbO_6 and NbO_7 basic units helps $KNbO_3$ perovskite as the product inherit the morphology of the Nb_2O_5 hollow spheres.

3.5.3. Kinetically modified MSS

Similar to other synthesis methods, the MSS method can affect its products characteristics by changing synthesis conditions including processing duration, processing temperature, type of salt, nature of precursor, ramp rate, etc. [14,48,30,92]. For complex metal oxides, single-source complex precursors can be advantageous to successfully synthesize high quality monodisperse NPs in terms of both chemical composition and particle size. Single-source precursors especially those are composed of simple inorganic ions help in two aspects: (i) homogeneous distribution and (ii) intimate atomic scale mixing of precursor and salt. Consequently its diffusion length is reduced; the rate of diffusion of the reactants in the molten salt increases, and material transport becomes highly efficient to meet the minimal kinetic requirement for the reaction, which is why this advanced MSS method is named kinetically modified MSS (KMMSS) method [13,89–91,172,174]. This KMMSS strategy can be exploited to its full potential for the preparation of variety of complex oxide nanocrystals due to its intrinsic simplicity, flexibility, and scalability. For example, the authors of this article have efficiently carried out the MSS process for $A_2B_2O_7$ type pyrochlore NPs using a single-source $A(OH)_3{\cdot}BO(OH)_2{\cdot}nH_2O$ complex precursor made via co-precipitation [30,48,89–92,110–112,121,174–182].

Using $La_2Zr_2O_7$ as an example of complex metal oxide nanocrystals, we have synthesized highly monodispersed cubic crystallites with an average size of 20 nm as seen in the TEM images (Fig. 16a, b). These nanocubes have flat surface while their edges and corners are a little distorted. Since the relative specific surface energies of facets dictate the shape of nanocrystals, the formation of cube in case of $La_2Zr_2O_7$ NPs can be attributed to a kinetic and morphological manifestation of the initial nuclei in the shape of a cube [13,183]. Lattice fringes of individual nanocubes (Fig. 16b) depict the single crystalline nature of the $La_2Zr_2O_7$ NPs. Elemental analysis by EDS (Fig. 16c) confirms the stoichiometry of La, Zr, and O in these nanocrystals to be 1:1:3.5 which is consistent with its chemical formula. Finally, the electron diffraction pattern (Fig. 16d) confirms the cubic phase of the $La_2Zr_2O_7$ NPs.

3.6. Different classes of simple and complex metal oxide NPs synthesized by MSS

Some metal oxides even in their nanostructured forms can be fabricated using different methods, such as hydrothermal or conventional colloid chemistry routes. However, the use of the MSS method may facilitate a higher crystallinity and contribute to a special texture in the final products. As exampled below, several types of both simple binary and complex oxides including their porous framework materials have been synthesized in different molten salt systems since 1970s [23].

3.6.1. Binary oxides

Pertaining to binary metal oxide systems, many reports have declared the use of the MSS method for MgO, ZnO, CuO, NiO, TiO_2, etc. Adjustable parameters such as synthesis temperature, salt/precursor used, and product characteristics along with relevant reference source are tabulated in Table 6. We explain some of the cases in details where the MSS method has not been extensively explored.

3.6.1.1. Iridium oxide NPs (IrO_2). Two of the best electrocatalysts for HER and OER reactions are crystalline IrO_2 and RuO_2 NPs even though a growing body of OER and HER catalysts containing abundant, inexpensive transition metals and their oxides have been reported recently in literature [192,195,196]. Nanostructured IrO_2 is commonly synthesized by metal organic chemical vapor deposition (MOCVD) [197–204]. Moreover, a variety of IrO_2 nanostructures have been produced by other strategies such as phase transport process [205], electrochemical synthesis [206], arc vaporization [207], hydrothermal [208], reactive radio frequency magnetron sputtering (RFMS) [209], sol–gel [210], wet chemistry method [195], Adams fusion method [211], sulfite complex route [212], thermal decomposition of precursor (H_2IrCl_6) [213], oleylamine-mediated synthesis [196], etc. However, all these synthesis techniques require expensive, complex, unstable and not-environmentally-friendly iridium-containing precursors. In addition, some of

Table 6
Examples of binary oxides produced by different MSS systems.

Oxide	Precursors/salt	Synthesis temp.	Product characteristics	Ref.
MgO	$MgSO_4$ or $MgCl_2/NaNO_3$-KNO_3 or $NaNO_2$-KNO_2	450–600 °C	Nanospheres, 50 nm	[184]
ZnO	$Zn(CH_3COO)_2/LiCl$	750 °C	Nanowires, 30–70 nm	[185]
TiO_2:Nb	NaCl-Na_2HPO_4	825 °C	Nanowires, 50–200 nm	[186]
WO_3	$(NH_4)_6H_2W_{12}O_{40}{\cdot}xH_2O/LiNO_3$-$KNO_3$	410 °C	NPs, 100 nm	[187]
α-Fe_2O_3	Fe_2O_3/NaCl	820 °C	Single-crystalline α-Fe_2O_3 rhombohedra, 200 nm with aspect ratio of 1.2	[188]
Co_3O_4	$CoCl_2$/NaCl-KCl	700 °C	Nanorods with diameter of 150 nm and length of 2 μm	[189]
CuO	$CuCl_2$/NaOH-KOH	200 °C	Flower-shaped nanostructure	[190]
In_2O_3:Ni	InOOH/$LiNO_3$	300–500 °C	NCs, <100 nm	[191]
Y_2O_3:Er	$Y(NO_3)_3/NaNO_3$-KNO_3	500 °C	NCs, <100 nm	[24]
IrO_2	$IrCl_4/NaNO_3$-KNO_3	650 °C	Nanorods, diameter = 15 nm, length = 200 nm	[192]
CeO_2:Ba	CeO_2-$BaCO_3$/NaOH-KOH	200 °C	Nanowires	[193]
ZrO_2	$ZrOCl_2/NaNO_3$-KNO_3	550 °C	NPs, 5–28 nm	[194]

these processes involve tedious synthetic procedures with complicated experimental setups. On the other hand, the MSS process is more cost effective, stable and eco-friendly compared to above reported methods. The research group of one of the authors of this article has implemented the MSS method with iridium tetrachloride, sodium chloride, and potassium chloride as the precursor and salt mixture to synthesize IrO_2 nanorods [192]. The precipitation of IrO_2 in a basic melt of chloride salts is a typical Lux–Flood acid–base reaction. For instance, the formation of IrO_2 from iridium chloride in the alkali metal nitrate salts proceeds by

$$IrCl_4 + 4NO_3^- \rightarrow IrO_2 + 4Cl^- + 4NO_2 + O_2 \quad (6)$$

The as-synthesized IrO_2 product by the MSS method is ultrafine nanorods appearing in rectangular shape (Fig. 17a–c). The diameter of the nanorods ranges from 8 nm to 20 nm with an average diameter of 15 nm, unlike the commercial IrO_2 NPs having a spherical shape with an average size of ~60 nm (Fig. 17d). The formed IrO_2 nanorods are composed of iridium and oxygen elements with no other impurities (inset of Fig. 17) and have an average diameter and length of ~15 nm and ~200 nm, respectively (Fig. 17e). The lattice spacing value of 3.20 Å which is consistent with (1 1 0) plane of IrO_2 crystal (Fig. 17f) and electron diffraction pattern with the circular fashion of the spots due to (1 1 0), (1 0 1), (2 0 0), (2 1 0), (2 1 1), and (2 2 0) planes indicate the formation of tetragonal crystal structure of IrO_2 nanorods which are consistent with XRD results [192].

Other groups like Kim et al. have used the MSS method from iridium chloride precursor, $NaNO_3$ salt, and cysteamine by calcining the reactant mixture at 450 °C to synthesized ultrathin IrO_2 nanoneedles [214]. The cross-sectional diameter of these IrO_2 long nanoneedles was found to be only 2.0 ± 0.5 nm (Fig. 18a). The diffraction ring corresponding to the (1 0 1) plane was the most significant in the selected area electron diffraction (Fig. 18b) which agrees with the X-ray diffraction pattern (Fig. 18e). Both high-resolution transmission electron microscopy image (Fig. 18f) and high angle annular dark field scanning TEM image with an atomic resolution (Fig. 18g) demonstrate that the formation of ultrathin long nanoneedles consists of about 6–8 layers of IrO_2 (1 1 0) plane.

3.6.1.2. Yttrium oxide NPs (Y_2O_3). Y_2O_3 is one of desirable luminescence hosts for phosphor applications because of its high chemical/photochemical stability, high melting point, wide band gap, easy to synthesize, ability to accommodate lanthanide ion at Y^{3+} site, and low phonon energy (430–500 cm^{-1}) [215,216]. Many studies have demonstrated that luminescent behavior of a phosphor powder is strongly dependent upon its particle size and size distribution [89,91,123,217,218], hence it is expected that NPs possess more surface luminous states because of their large surface area, and accordingly can display different luminescent properties than the bulk counterparts [219–222]. Moreover, it has been reported that phosphor particles with uniform size distribution and well defined shape are required for highly efficient photo luminescence [223,224]. Therefore, one of the authors of the current article used the MSS method to synthesize Er^{3+}:Y_2O_3 NPs as an upconversion phosphor using yttrium nitrate as the precursor in KNO_3-$NaNO_3$ molten salt at 500 °C [24]. The as-synthesized Er^{3+}:Y_2O_3 NPs are pure, single crystalline, of cubic phase, have an average size of ~80 nm with flat surface and distorted corners/edges (Fig. 19).

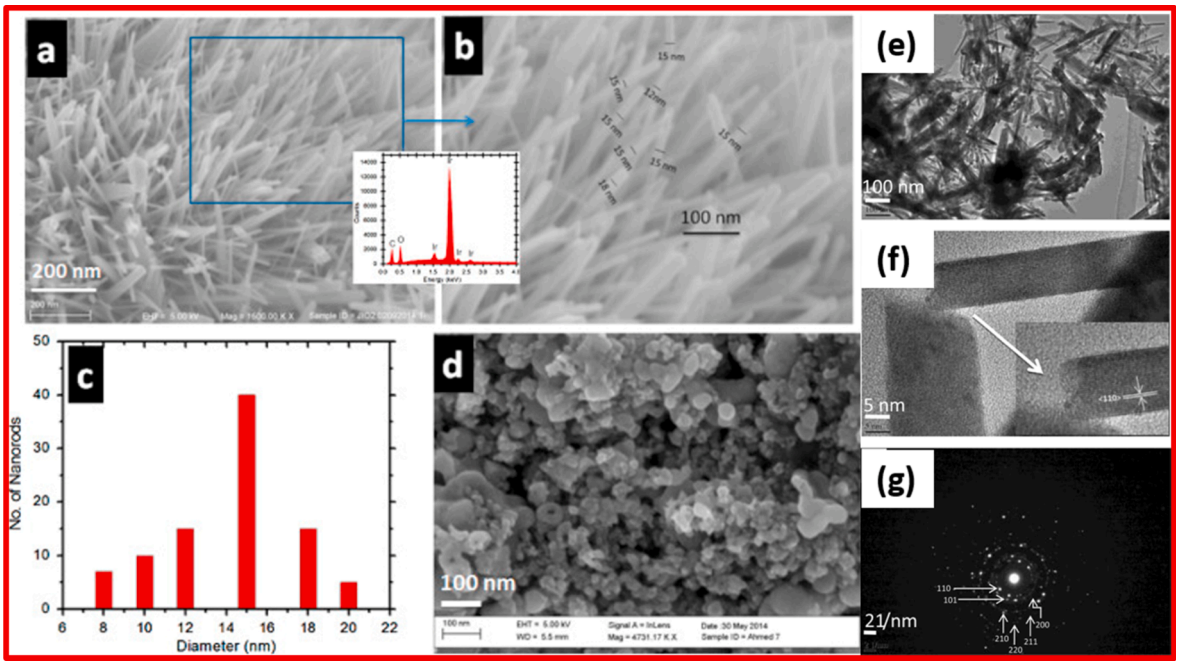

Fig. 17. (a & b) FESEM images of the MSS synthesized IrO_2 nanorods. The inset shows the corresponding energy dispersive X-ray spectrum. (c) Size distribution of the IrO_2 nanorods with respect to the diameters. (d) FESEM image of the commercial IrO_2 NPs. Representative (e) TEM and (f) HRTEM images and (g) electron diffraction pattern of the IrO_2 nanorods [192]. *Copyright 2016. Reproduced with permission from Elsevier.*

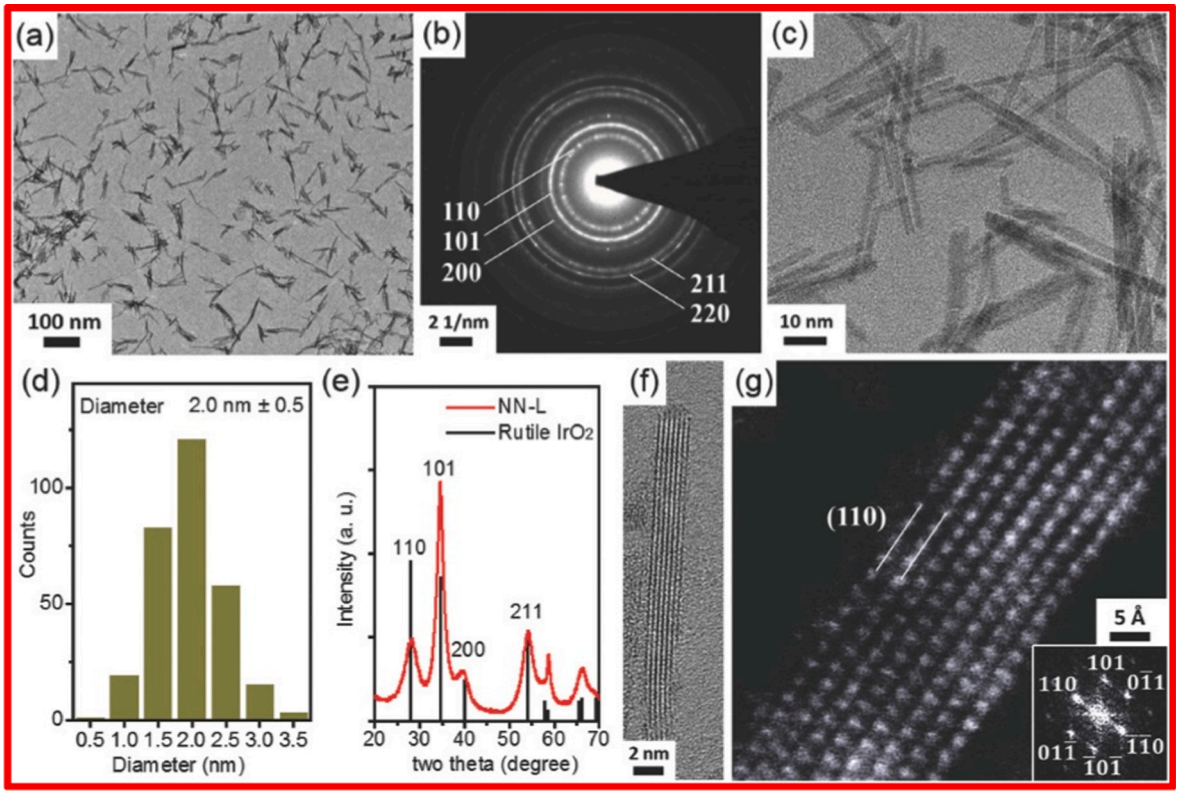

Fig. 18. (a) TEM image at low magnification, (b) SAED, (c) TEM image, (d) histogram of diameter, (e) XRD pattern, (f) HRTEM image, and (g) HAADF-STEM image of the IrO_2 nanoneedles. The reference pattern in (e) represents the standard diffraction of rutile IrO_2 (PDF#00-015-0870). The inset of (g) shows corresponding electron diffraction spots [214]. *Copyright 2018. Reproduced with permission from Wiley and Johns.*

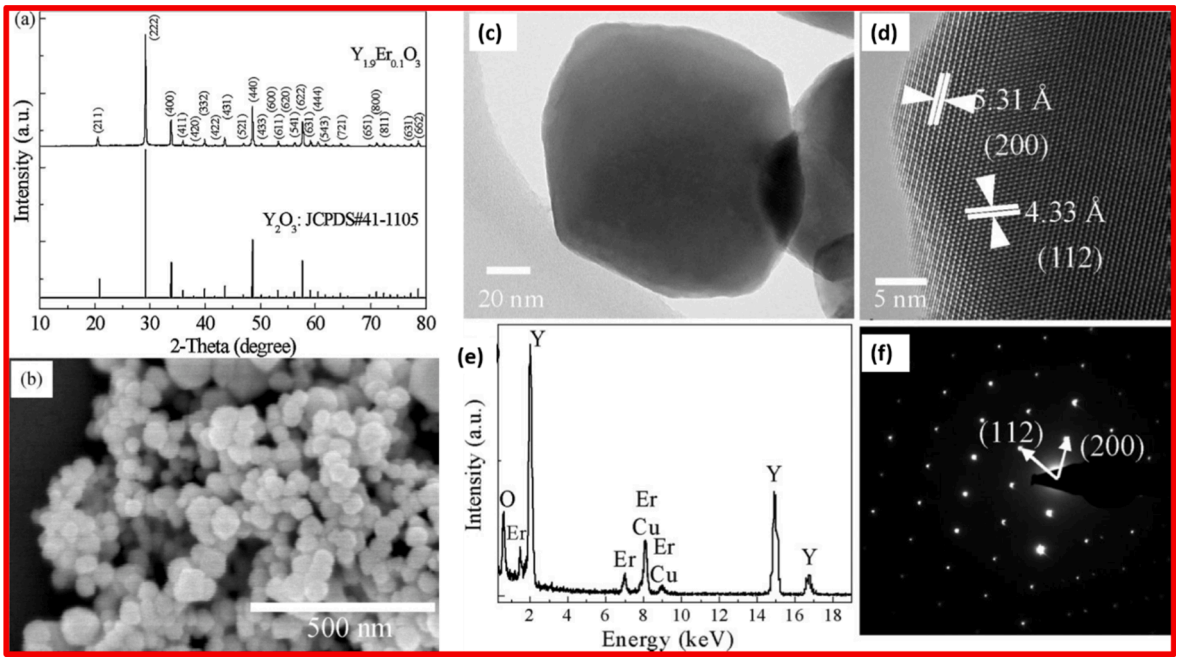

Fig. 19. The as-prepared 5%Er^{3+}:Y_2O_3 NPs by the MSS method: (a) XRD pattern, (b) SEM image, (c) TEM image, (d) HRTEM image, (e) EDS spectrum (the Cu peaks originate from the TEM grid), and (f) SAED pattern [24]. *Copyright 2009. Reproduced with permission from Wiley and John.*

There have also been a few reports on the MSS synthesis of bulk Y_2O_3:Eu^{3+} powders which are one of important and commercialized red emitting phosphors [225,226]. Xiaoyong Wu et al. have used Y_2O_3/Eu_2O_3 precursor in both KNO_3-$NaNO_3$ and KCl-NaCl molten salts to synthesize Y_2O_3:Eu^{3+} with different morphologies (Fig. 20a and b) [225]. It is known that the shape of particles is governed by their growth mechanisms. Cahn et al. have reported that spherical particles predominate when the growth mechanism proceeds via proliferation, and anisotropy comes into picture while the particle shape changes when the growth mechanism proceeds via interfacial reactions [227]. In the MSS process, the growth mechanism mostly follows interfacial reactions because the formation and growth of particles proceed via liquid transmission which supposedly has high liquidity and proliferation rate [225]. On the other hand, Yan et al. have used YCl_3/$EuCl_3$ as a precursor and the mixture of Na_2CO_3 + S + NaCl as the molten salt at 1200 °C for 2 h to make quasi-microspheres of 2–3 μm [226]. Luo et al. have synthesized Y_2O_3:Eu^{3+} nanocrystals using a surfactant aided MSS procedure. They tuned the particle size by changing the nature of used surfactants (Fig. 20c–f) [228].

3.6.2. Complex metal oxides

3.6.2.1. ABO_3 type perovskites. Owing to the scientific and application importance [14,29,68,107,113,224,229–241], the synthesis of high quality perovskite materials in well-defined size and morphology becomes vital. It is one of the research themes of the authors of the current article [14,29,105,107,113,235–242]. Recently, Xue et al. have summarized the advances of low dimensional perovskite nanomaterials by the MSS method [68]. To give a concise picture of the MSS of various perovskite compounds, here we have tabulated reported results in Table 7. For discussion, we have taken specific examples of nanocrystalline $BaTiO_3$ synthesized by the MSS method.

$BaTiO_3$ is one of the most important ferroelectric materials [251,252]. It has received intensive research interest for a number of important advanced applications when developed in nanosized domain including electrocaloric cooling devices [253], spintronics [254], triboelectric nanogenerators [255], energy harvester and sensor [256], pyroelectric catalysts [257], piezoelectric characteristics [258], etc. There have been many recent reports on designing $BaTiO_3$ nanostructures using various wet chemical methods such as hydrothermal method [259], combustion approach [260], solution casting [261], spin coating [262], etc. These techniques have several issues, such as low yield, the use of toxic solvent, safety related concerns, and low scalability, etc. Owing to the importance of shape controlled synthesis of $BaTiO_3$ nanostructures, the MSS method has been used to synthesis $BaTiO_3$ in the form of nanostrips, nanocubes, nanospheres, nanowires, NPs, nanorods, etc. [29,245,71,154,246,263,264].

Owing to the existence of anisotropy in various crystallographic directions, single crystals have superior piezoelectric performance compared to polycrystalline counterparts [265]. Also, $BaTiO_3$ synthesized in nanowire shape enhances its piezoelectric catalytic performance compared to its NPs [258]. Hence, our group has made single-crystalline $BaTiO_3$ nanowires using the MSS method by exploring NaCl as a molten salt which is aided by a non-ionic surfactant (Fig. 21A–E). The formed $BaTiO_3$ nanowires are uniform, homogenous and defect free single-crystals with diameter of ~50–80 nm and length of 1.5–10 μm. These nanowires are composed of

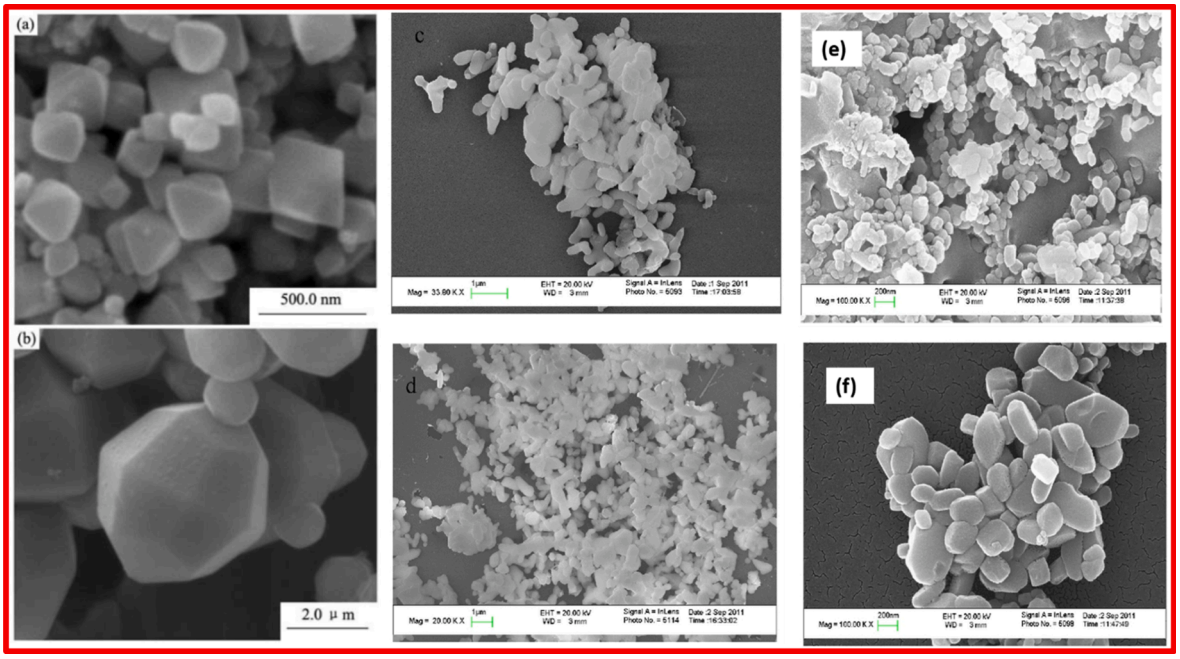

Fig. 20. SEM micrographs of the MSS synthesized Y_2O_3:Eu^{3+} particles using (a) KNO_3/$NaNO_3$ and (b) KCl/NaCl molten salts [225]. *Copyright 2010. Reproduced with permission from Elsevier.* SEM micrographs of the MSS synthesized Y_2O_3:Eu^{3+} particles using different surfactants: (c) octyl phenol together ethylene (10) ether oxygen (OP-10), (d) sodium dodecyl benzene sulfonate (LAS), (e) polyoxyethylene (5) nonyl phenyl ether (NP-5), and (f) polyoxyethylene (10) nonyl phenyl ether (NP-10) [228]. *Copyright 2013. Reproduced with permission from Hindawi.*

Table 7
Summary of various perovskite nanomaterials synthesized by the MSS method.

Perovskite	Salt	Synthesis temp.	Product characteristics	Ref.
$BaTiO_3$	KCl	800 °C	Micron size, electrical properties	Yoon et al. [243]
	$PbCl_2$	600–800 °C	Micron size, dielectric properties	Ito et al. [244]
	NaCl-KCl	950 °C	Rectangular nanostrip	Deng et al. [245]
	NaCl	820 °C	Single crystalline nanowires	Mao et al. [29]
	NaOH-KOH	300 °C	Nanocrystal, dielectric properties	Sahoo et al. [246]
$SrTiO_3$	KCl	750 °C	Nanowires	Li et al. [71]
	NaCl	820 °C	Single crystalline nanocubes	Mao et al. [29]
	NaCl-KCl	700 °C	NPs	Li et al. [247]
$Ca_{1-x}Sr_xTiO_3$	NaCl	720 °C	NPs: 70–110 nm	Mao et al. [107,235]
La_2BMnO_6 (B = Ni, Co)	$NaNO_3$-KNO_3	700 °C	NPs, ~64 nm	Mao et al. [105]
$BaZrO_3$	NaOH-KOH	720 °C	Shape tunable single crystal	Zhou et al. [241,241]
$PbTiO_3$	NaCl-KCl	900 °C	Rod-shape single-crystal	Cai et al. [248]
$ANbO_3$ (A = K, Na)	KCl	800 °C	TMSS, wire like structure	Li et al. [25]
$K_{0.5}Bi_{0.5}TiO_3$	KCl	900 °C	Nanowires (φ ~ 40 nm, l > 4 μm)	Yang et al. [249]
$BaMnO_3$	NaOH-KOH	200 °C	Elliptical nanorods (width ~20–50 nm)	Hu et al. [250]

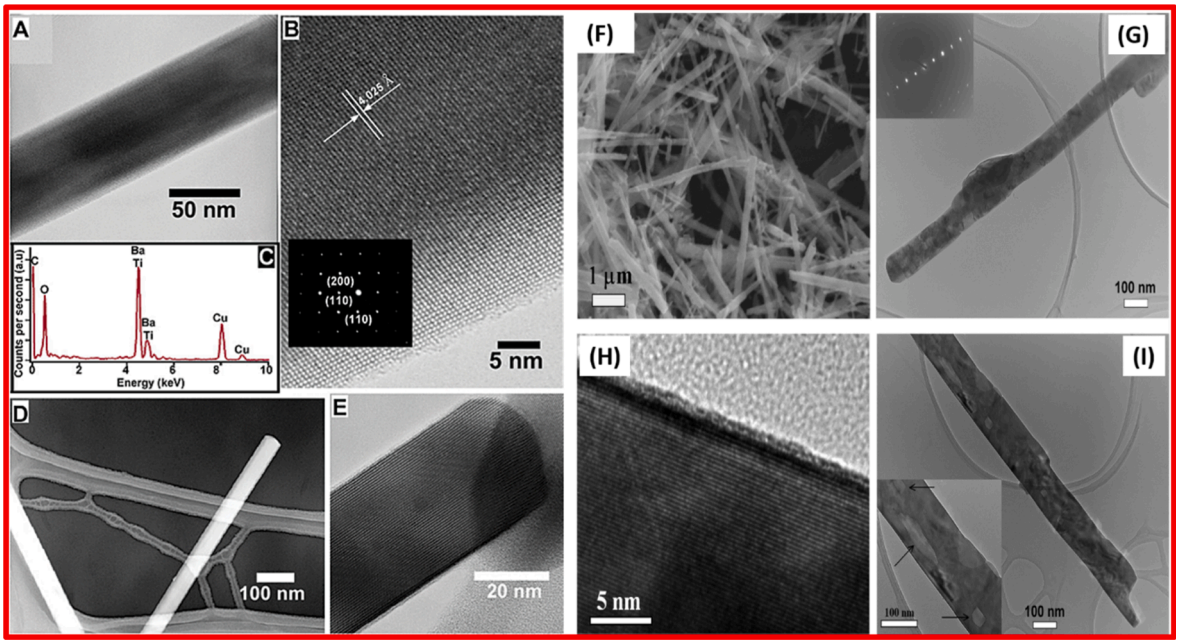

Fig. 21. $BaTiO_3$ nanowires synthesized by the MSS method: (A) TEM, (B) HTREM with SAED pattern as inset, (C) EDS spectrum, and (D) TEM and (E) HRTEM images representing the tip of the nanowires [29]. *Copyright 2003. Reproduced with permission from the American Chemical Society.* $BaTiO_3$ nanowires synthesized by topochemical solid state reaction: (F) SEM, (G) TEM, (H) HRTEM, and (I) ED pattern [264]. *Copyright 2009. Reproduced with permission from the American Chemical Society.*

only Ba, Ti, and O elements and have high crystallinity with cubic structure. Moreover, the tips of these nanowires are smooth and hemisphere like.

Also, Buscaglia et al. [264] synthesized $BaTiO_3$ nanowires (diameter: 50–300 nm and length: 2–30 μm) by using a topochemical MSS route as shown in Fig. 21F and 21G. Electron diffraction pattern at different location of the nanowire shown in inset of Fig. 21G depicted the same diffraction pattern with very well defined and sharp spot indicating single crystalline nature of nanowires. Lattice fringes shown in Fig. 21H matches well with the cubic crystal of $BaTiO_3$. The issue with the $BaTiO_3$ nanowires synthesized by the topochemical SSR route is the presence of high dislocation, defects, grain boundaries and internal pores as can be easily seen from the electron diffraction pattern shown in Fig. 21I. This again highlighted the superiority of the MSS process over other methods.

The MSS method has also been used to synthesize nanocubes, nanospheres, and nanorods of $BaTiO_3$ (Fig. 22a–c) [154]. Huang et al. highlighted the role of the initial shape of titania and its rate of dissolution on the final shape of $BaTiO_3$ nanostructure synthesized by the MSS method in a NaCl-KCl flux at 700 °C for 1 h [154]. Deng et al. reported the MSS synthesis of $BaTiO_3$ nanostrips using a surfactant-free approach in non-aqueous molten salt media (Fig. 22d–f). The synthesized strips have a diameter of 50–200 nm, a thickness of 20–50 nm, and a length of several to tens of microns.

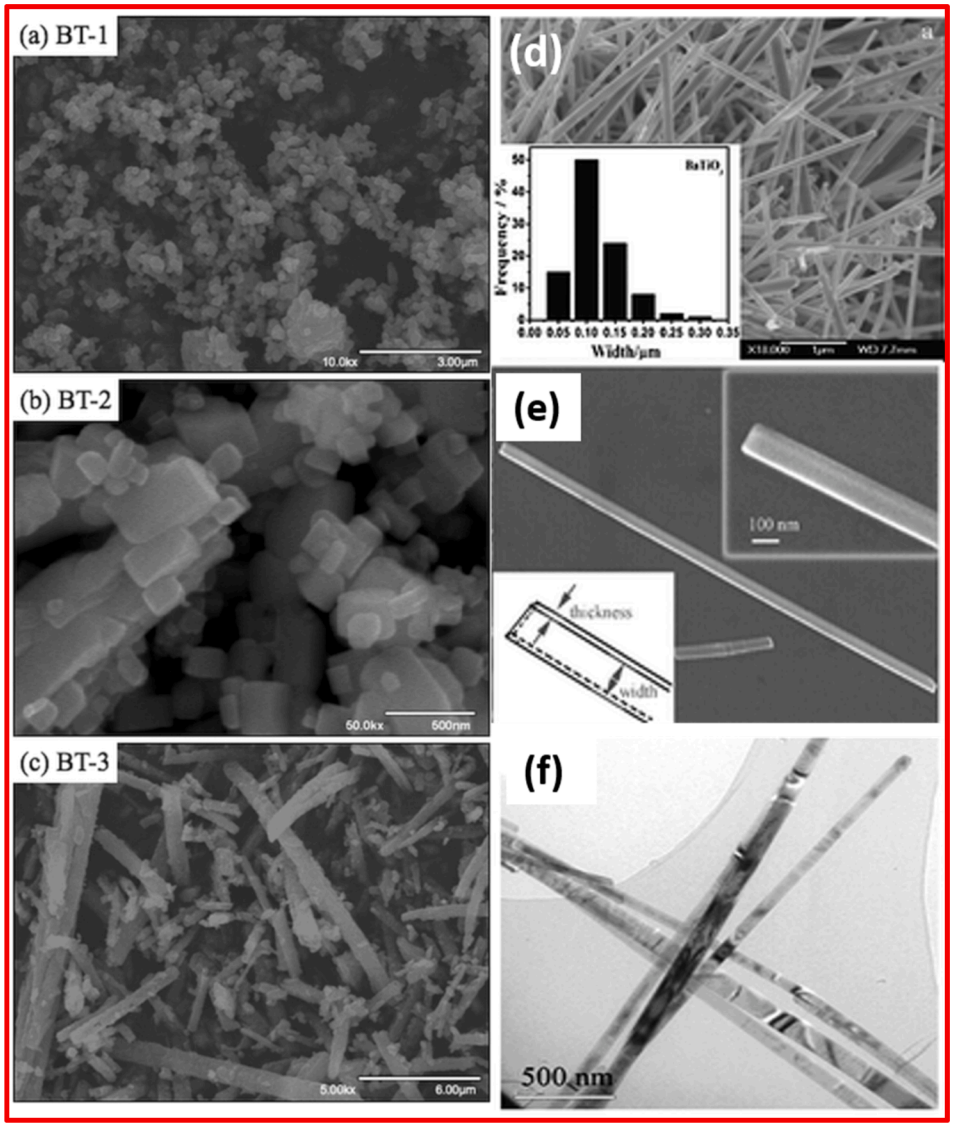

Fig. 22. $BaTiO_3$ nanostructures synthesized by the MSS method: (a) nanospheres, (b) nanocubes, and (c) nanorods [154]. *Copyright 2009. Reproduced with permission from the American Chemical Society.* $BaTiO_3$ nanostrips: (d) SEM, (e) high magnification SEM, and (f) TEM images [245]. *Copyright 2009. Reproduced with permission from the Royal Society of Chemistry.*

3.6.2.2. ABO_2 type delafossites. ABO_2 type compounds are categorized as delafossite oxides where 'A' is a monovalent cation in +1 oxidation state (such as Cu, Ag, etc.) and B is a trivalent cation in +3 oxidation state (such as Al, Ga, In, Fe, etc.). The delafossite structure is comprised of edge share distorted BO_6 octahedra arranged in alternative layers whereas A cation is oriented in 2D closed pack array of dumbbell-shaped O-A-O and oxygen is tetrahedrally coordinates with A^+ and B^{3+} cations [266]. Because of their high surface area, chemical reactivity, electron-hole overlap integral, and interfacial energy, ABO_2 NPs are expected to possess a multitude of applications. These include UV photodetectors [267], oxide sensors [268], catalysts [266,269–271], sodium ion batteries [272], photovoltaics devices [273], solar cells [274–277], etc. Delafossite NPs have been synthesized by various methods such as hydrothermal [270,278,279], flash auto-combustion [280], chemical deposition [267], glycine-nitrate process [268], oxygen plasma enhanced reactive evaporation technique [281], sol–gel [282], co-precipitation method [283], etc. All these methods have their own advantages and disadvantages. For example, chemical deposition technique requires costly and sophisticated instrumental set-up and is not financially viable. Sol-gel method is difficult to achieve shape and size control of products. Combustion technique faces safety concerns. Hydrothermal method requires autoclaves and product yield could be an issue.

The MSS method is an easy and green approach to synthesize Cu-based delafossite NPs with excellent material properties. Santra et al. have demonstrated the feasibility of the MSS method to synthesize $CuBO_2$ nanorods using KCl salt at 800 °C [284]. They studied the evolution of the $CuBO_2$ nanorods by exposing for three different time intervals of 30, 60 and 180 min (Fig. 23). The formation and growth of the copper borate nanorods was clearly seen with the increase of the MSS processing time from 30 min to 60 min, and then to

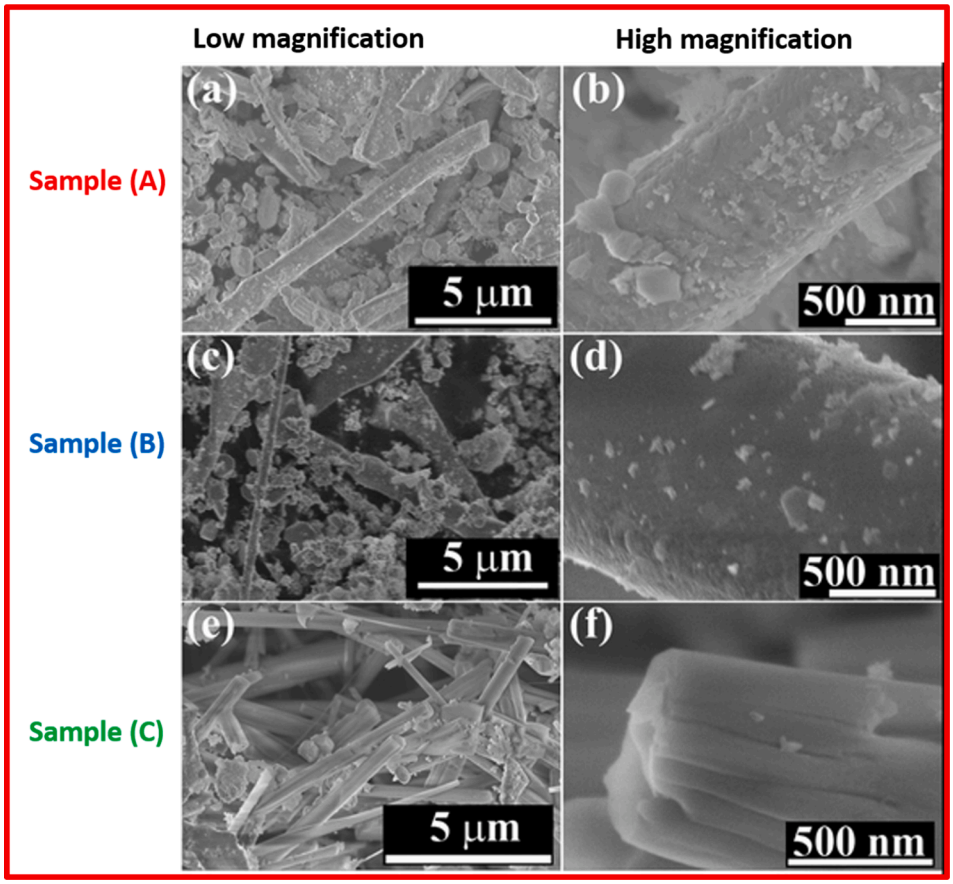

Fig. 23. $CuBO_2$ nanorods synthesized the MSS method as samples A, B and C for different time intervals of 30, 60 and 180 min, respectively [284]. *Copyright 2015. Reproduced with permission from the American Chemical Society.*

180 min. As the MSS processing time increases, the surface roughness of these microrods also reduces.

Accordingly, Santra et al. have drawn a schematic and proposed a growth mechanism of the MSS process for the $CuBO_2$ nanorods (Fig. 24) [284]. As depicted pictorially, when the processing time was 30 min, the formed $CuBO_2$ nanorods were attached with small and irregular particles of primary $CuBO_2$ nanocrystals which have not been converted into nanorods due to short processing time. When the processing time is raised to 60 min, these primary attached $CuBO_2$ NPs grew into nanorods and got detached from the host bundle surface, which leads to the reduction of the surface roughness of the rods even though some of the remnant NPs are still lying on the surface of the $CuBO_2$ nanorods. These NPs were gradually converted into small nanorods as the reaction time was raised to 180 min. These small nanorods further form nanobundles and get detached from the previous host bundles to reduce surface energy. At the end of this stage, all nanorods are quite uniform as all the precursors are transformed into nanorods (and bundles).

TEM studied conducted on the sample C suggested that the tips of individual nanorods are less than 100 nm in diameter. The *d* spacing was measured to be 2.33 Å, which is well in agreement with XRD data [284].

3.6.2.3. AB_2O_4 type spinels. AB_2O_4 type spinel compounds have divalent A and trivalent B ions occupying tetrahedral (T_d) and octahedral (O_h) sites, respectively, in a cubic crystal (S.G. Fd-3m). The structure has two variants as normal and reverse spinels differing in their distribution at T_d and O_h sites. In normal spinel, 1/8th of T_d sites is occupied by A ions and only half of the O_h sites is occupied by B ions. On the other hand, in inverse spinel, half of B ions and entire A ions occupies O_h sites and half of the B ions occupies T_d sites [285]. Spinel compounds have unique properties which make them suitable for various technical applications such in persistent phosphor [286], nuclear waste host [287], luminescence host [288–290], defect induced emission [291], spintronic devices [292], electronics [293], magnetism [294], catalyst [295–297], biomedical [298], lithium ion batteries [299], etc. These applications not only depend on their ionic arrangement or structure, but also on how they are synthesized [300].

The traditional method of preparing spinels is via the SSR route which needs continuous grinding and heating of the solid precursors (usually oxides, nitrates and carbonates) [301,302]. Because of the high diffusing length, this route requires high heating temperature and long time to cross its activation barrier [303]. Another problem with solid-state synthesized spinel compounds is their low surface area, high level of agglomeration, large and non-uniform particles, and irregular shape, which seriously degrade their various physical and chemical properties. There have been continuous exploration of low temperature, easy to perform and mild

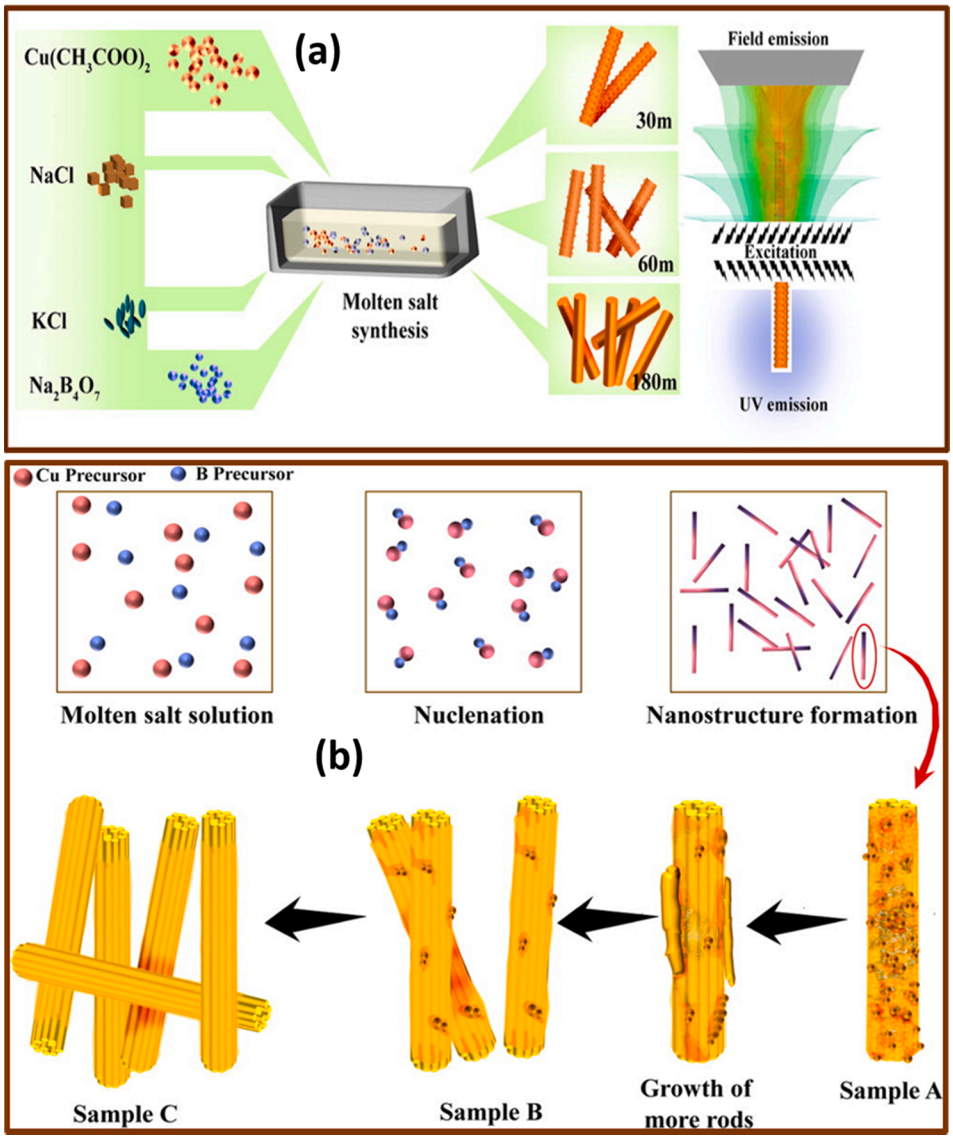

Fig. 24. MSS of $CuBO_2$ nanorods in KCl molten salt: (a) schematic and (b) proposed growth mechanism [284]. *Copyright 2015. Reproduced with permission from the American Chemical Society.*

approach to synthesize spinels such as gel-combustion [304], hydro/solvothermal route [305], sol–gel method [291], and co-precipitation [306]. However, it is still a challenge to synthesize uniform and small NPs of spinels under non-harsh environments through environmentally friendly approaches.

Recently, there has been an upsurge of the MSS method to synthesize spinel compounds by various researchers for advanced applications. Spinel nanostructures with high surface area, in well-defined shape, and free of agglomeration is vital for their applications in optoelectronics, catalysis, gas sensing, etc. [189,307,308]. Here we have compiled spinel nanostructures synthesized by the MSS method under various synthesis conditions and tabulated them in Table 8. For example, Zhang et al. have synthesized micron-sized $MgAl_2O_4$ in metal halide salts and proposed that the size and morphology of the final product are strongly dependent on the original size/shape of the alumina precursor and the MSS synthesis is governed by template formation process [309]. Moreover, Kim et al. have reported the MSS synthesis of highly ordered $LiNi_{0.5}Mn_{1.5}O_4$ spinel as an electrode material for lithium ion battery using a salt mixture of LiCl and LiOH [310]. Lin et al. have also synthesized the same compound using a slightly modified MSS procedure [311]. They have first synthesized a precursor using a sol–gel process and then calcined the precursor with LiOH in KCl molten salt to synthesize $LiNi_{0.5}Mn_{1.5}O_4$. It was reported that $Ni_{0.5}Zn_{0.5}Fe_2O_4$ was synthesized by the MSS method involving a reaction between Fe_2O_3, NiO, and ZnO powders. Furthermore, spinel $LiMn_2O_4$ nanowires have been synthesized by a novel reaction method using $Na_{0.44}MnO_2$ nanowires as a self-template wherein Na/Li ion exchange and addition of more Li ions were carried in a molten salt mixture of $LiNO_3$ (88 mol%) and LiCl (12 mol%) at 450 °C for 1 h [308]. The synthesized $LiMn_2O_4$ demonstrated highly superior

Table 8
Examples of various spinel nanocrystals synthesized by the MSS method.

Nanospinel	Salt	Synthesis temp.	Product characteristics	Ref.
Co_3O_4	NaCl-KCl	700 °C	Nanorods (diameter: 150 nm and lengths of about 2.0 μm) Nanorods (diameter: 40–100 nm and lengths of about 10 μm)	Ke et al. [189]
	NaCl	800–815 °C		Liu et al. [312]
Mn_3O_4	NaCl	850 °C	Nanowires (diameter: 40–80 nm and lengths up to 150 μm)	Wang et al. [26]
$ZnFe_2O_4$	NaOH-NaCl	700 °C	NPs, 15–20 nm	Darshane et al. [307]
$MgAl_2O_4$	KCl	850 °C	Nanospheres, ~30 nm	Naeini et al. [246]
	LiCl/NaCl/KCl	800–1150 °C	Microcrystals	Zhang et al. [309]
$LiNi_{0.5}Mn_{0.5}O_4$	LiCl	700–1000 °C	Microcrystals, single crystal octahedra	Kim et al. [310]
	KCl	900 °C	Microcrystals, 500–800 nm	Lin et al. [311]
$LiMn_2O_4$	LiOH	600 °C	Nanooctahedrals, ~80 nm	Wang et al. [313]
	NaCl-KCl	700 °C	Hollow spheres, 50 nm	Zhao et al. [314]
	$LiNO_3$-LiCl	450 °C	Nanowires: diameter: 50–100 nm	Hosono et al. [308]
$NiFe_2O_4$	NaCl	700 °C	Nanocube, ~15 nm	Darshane et al. [315]
$Ni_{0.5}Zn_{0.5}Fe_2O_4$	NaCl	800 °C	NPs: ~29 nm	Mouhib et al. [316]
	NaCl-KCl	900–1050 °C	Nanocrystals: ~30–50 nm	Jiang et al. [317]

performance particularly for lithium ion battery with high power density.

Furthermore, to harness the full potential of $ZnFe_2O_4$ NPs for H_2S gas sensing application, Darshana et al. have synthesized $ZnFe_2O_4$ NPs using NaOH/NaCl molten salt at 700 °C (Fig. 25A) [307]. The formed $ZnFe_2O_4$ spinel NPs have a diameter of ~15–20 nm with highly crystalline nature and cubic structure. These NPs have also showed excellent selective sensitivity toward 200 ppm of H_2S at the operating temperature of 250 °C. Wang et al. reported the synthesis of Mn_3O_4 nanowires using NaCl molten salt at 850 °C (Fig. 25B)

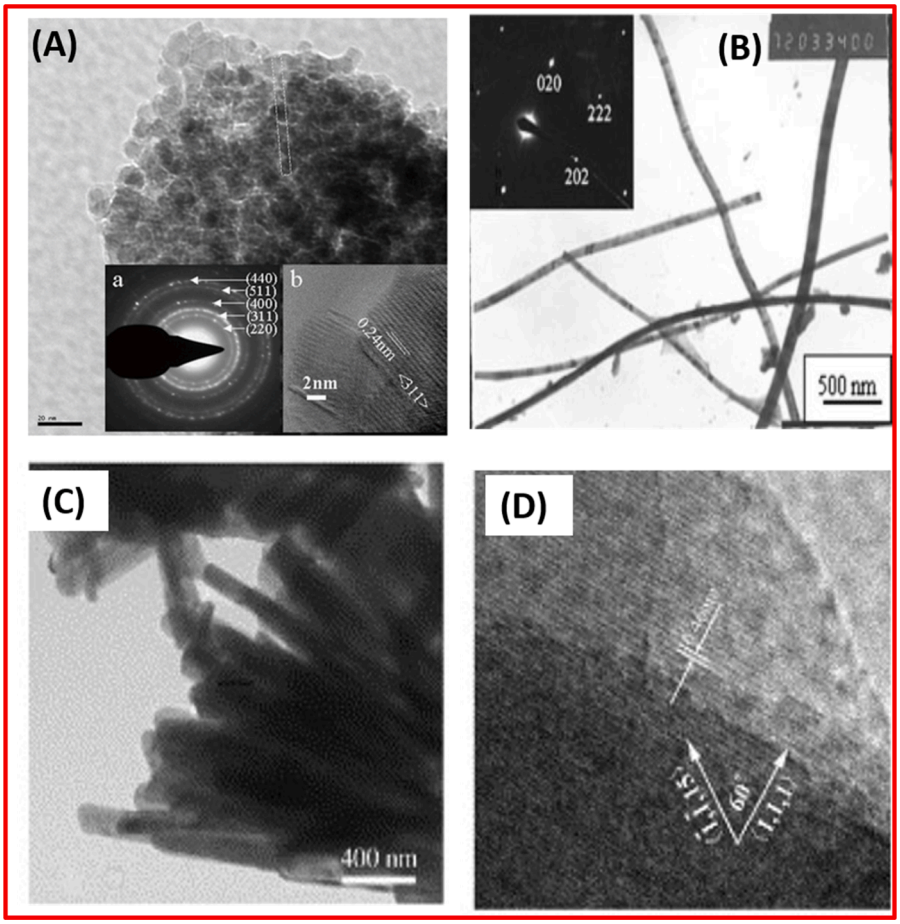

Fig. 25. Representative spinel nanostructures synthesized by the MSS method: (a) $ZnFe_2O_4$ NPs [307]. *Copyright 2014. Reproduced with permission from John Wiley and Sons.* (b) Mn_3O_4 nanowires [26]. *Copyright 2002. Reproduced with permission from John Wiley and Sons.* (C& D) Co_3O_4 nanorods [189]. *Copyright 2007. Reproduced with permission from Elsevier.*

[26]. The nanowires have a diameter of ~40–80 nm and a length up to 150 μm. It is expected that such 1D nanomaterial have improved electronic, optical, and mechanical properties for applications in electronic devices [26,308]. On the similar line, Co_3O_4 nanorods were synthesized using NaCl-KCl salt at 700 °C (Fig. 25C) [189]. The diameter and length of these nanorods are around 150 nm and 2 μm, respectively. Following the Ostwald ripening mechanism, Co_3O_4 nanorods grew along the (−1, −1, 15) direction along a 60° angle to the (1 1 1) plane (Fig. 21D).

3.6.2.4. $A_2B_2O_7$ type pyrochlores. Complex metal oxides with the $A_2B_2O_7$ composition, where A and B are respectively in 3+ and 4+ oxidation states, have been a focal point of scientific research over many years. Depending on the A/B radius ratio and other influencing factors such as temperature, pressure and doping effect, they are known to exist in ideal pyrochlore structure (space group Fd-3m) or defect fluorite structure (space group Fm-3m). Accordingly, they can display a wide range of solid solutions between BO_2 and A_2O_3. Because of the various unique properties exhibited by $A_2B_2O_7$ materials such as lower thermal conductivity, high dielectric constant, high thermal stability, structure flexibility, high radiation stability, ability to accommodate dopant ion at both A and B sites [89,217,318,319], they have displayed exemplary performance in various technological applications. These includes nuclear waste host [90], scintillator [112], luminescence host [89,217], catalyst [320–322], gas sensors [323], ionic conductor [324], magnetism [325,326], etc.

Doping pyrochlore materials can also leads to interesting optical properties, order–disorder phase transition, catalytic properties, radioluminescence, magnetic properties, etc. [90,110,111,178–181,327–330]. It is believed that higher concentration of activator ions can be doped in pyrochlore materials going from bulk to nanosized domain. Also, the higher electron-hole overlap integral of pyrochlore NPs may yield higher oscillator strength which can increase photoluminescence and radioluminescence efficiency. The higher electron-hole overlap integral in nanostructured material comes from the nanoscale localization of electrons and holes [331,332]. In addition, clinical procedure requires that injected bioimaging agents are cleared from the human body as quickly as possible. Renal mode is the main clearance route for bioimaging agents which require the size of NPs (including surface modifiers) to be smaller than 10 nm. In other words, the smaller NPs the better for medical applications. Hence, developing new or modified synthetic strategies to prepare sub-10 nm luminescent NPs is of crucial importance.

Usually, phosphors prepared by high temperature solid-state routes results in micron-sized particles which are not desirable for optoelectronics, scintillator and X-ray based bioimaging applications. Moreover, Wang et al. have published a brief review article to summarize $A_2B_2O_7$-type powders and ceramics prepared by various synthesis methods [333]. In recent years, as a novel synthetic technique, the MSS method has been regarded as an effective and convenient method to synthesize $A_2B_2O_7$ NPs at relatively low temperature with high level of monodispersity. One of the co-authors of this article has developed a kinetically modified MSS for the synthesis of $A_2B_2O_7$ NPs employing single-source precursors which have been explained in detailed earlier [48]. In the past several years, the authors of this article and their coworkers have carried out extensive work on the MSS of pyrochlore NPs in different modifications such as undoped, lanthanide ion doped, core shell NPs, etc. [30,89,91,121,181,217,334]. Moreover, to fine tune the photoluminescence and radioluminescence properties of the $A_2B_2O_7$ NPs, we have played with various MSS processing parameters such as the pH value of coprecipitation solution, MSS processing time, MSS processing temperature, etc. [89,91,182,217]. To include the effort from many other research groups in this area, we have compiled the $A_2B_2O_7$-type microcrystals and NPs synthesized by the MSS method with various synthesis parameters and tabulated them in Table 9.

In this article, we take the $La_2Hf_2O_7$ and $Lu_2Ti_2O_7$ nanocrystals as specific examples synthesized by the MSS method. Lanthanum hafnate $La_2Hf_2O_7$, due to its high density of 7.9 g/cm^3 and the presence of Hf with Z = 72, provides high stopping power for X-ray and γ-ray [91,112]. It exists in the cubic pyrochlore crystal structure with space group Fd-3m and a = 10.785 Å [344]. With such properties, it is considered as a potential matrix for novel high energy radiation detectors such as scintillators and X-ray phosphors. In the past, spectroscopic investigations of $La_2Hf_2O_7$ doped with Eu^{3+}, Tb^{3+}, Pr^{3+}or Ce^{3+} ions have proved that this matrix is able to transfer the gained energy to dopants and produce luminescence of significant intensity [91,112,345–348].

Very recently, we have highlighted the potential of the MSS method over direct calcination in synthesizing $La_2Hf_2O_7$ and $Pr_2Hf_2O_7$ NPs at 650 °C (Fig. 26) [177]. The difference arises because the MSS procedure proceeds differently with direct calcination from the single-source precursor. Direct calcination can synthesize pyrochlore phased compounds, but only at high temperature of 1000 °C, so the products no longer remain in nanosized domains rather are micron-sized particles.

The MSS synthesized $La_2Hf_2O_7$ NPs are mostly sphere shaped and have the average diameter of ~10–12 nm (Fig. 27) [217]. The Fourier transformed (FT) image illustrated the lattice planes in two different sized NPs, showing interplanar spacing's of 3.125 Å and 3.202 Å, which correspond to the (222) and (311) planes of order pyrochlore $La_2Hf_2O_7$.

Lutetium titanium oxide ($Lu_2Ti_2O_7$) is another important pyrochlore due to its high refractive index and high density which make it highly efficient for scintillation and optical imaging applications. Li et al. have carried out extensive research on synthesizing microcrystals, nanorods and nanowires of $Lu_2Ti_2O_7$ using the MSS method [340–342]. They have successfully synthesized nanowires using KCl salt at 1000 °C with almost 100% formation of nanowires (Fig. 28a & b). The nanowires have a diameter of 10–500 nm and a length upto several tens of micrometers. The faceted topography of these $Lu_2Ti_2O_7$ nanowires is attributed to chemical interaction between them (Fig. 28c). The same group has also reported the synthesis of $Lu_2Ti_2O_7$ nanorods using NaCl salt at 1000 °C. The formed nanorods have cross-section of six-sided polygon with a length of several microns, a diameter of 50–500 nm, an aspect ratio of 15–20, and single-crystalline nature (Fig. 28d–f).

Table 9
Examples of various pyrochlore nanocrystals synthesized by the MSS method.

$A_2B_2O_7$ pyrochlore	Salt	Synthesis temp.	Product characteristics	Ref.
$La_2Hf_2O_7$	$NaNO_3$-KNO_3	650 °C	Nanospheres, ~20–50 nm	Mao et al. [30,89–92,110–112,180,217]
$Yb_2Ti_2O_7$	$CaCl_2$-NaCl	650 °C	Microcrystals	Gilbert et al. [117]
	NaCl-KCl-NaF	1200 °C		Hand et al. [335]
$RE_2Hf_2O_7$ (RE = Gd, Y, Pr, Er and Lu)	$NaNO_3$-KNO_3	650 °C	Nanospheres, ~20–50 nm	Mao and Group. [110]
	NaCl–KCl	1100 °C	Submicron $La_2Zr_2O_7$	Huang et al. [49]
	$NaNO_3$-KNO_3	650 °C	Nanospheres, ~20–50 nm	Mao and Group. [48,121,181,182,334,336]
$La_2Zr_2O_7$	K_2SO_4-Na_2SO_4	800 °C	NPs: 60–90 nm	Wang et al. [337]
$Gd_2Ti_2O_7$	LiCl-KCl	750 °C	Nanocrystals	Dharuman et al. [338]
$Y_2Sn_2O_7$	KOH	400 °C	Microcubes	Nithyadharseni et al. [339]
	NaCl	900 °C	Micron-sized octahedral crystals	Li et al. [340]
$Lu_2Ti_2O_7$	NaCl	1000 °C	Nanorods (dia. 50–500 nm, length of several microns)	Li et al. [341]
	KCl	1000 °C	Single crystalline nanowires (dia. 200 nm)	Li et al. [342]
$La_2Ce_2O_7$	NaCl-KCl-NaF	1100 °C	Micron-sized crystals	Huang et al. [343]

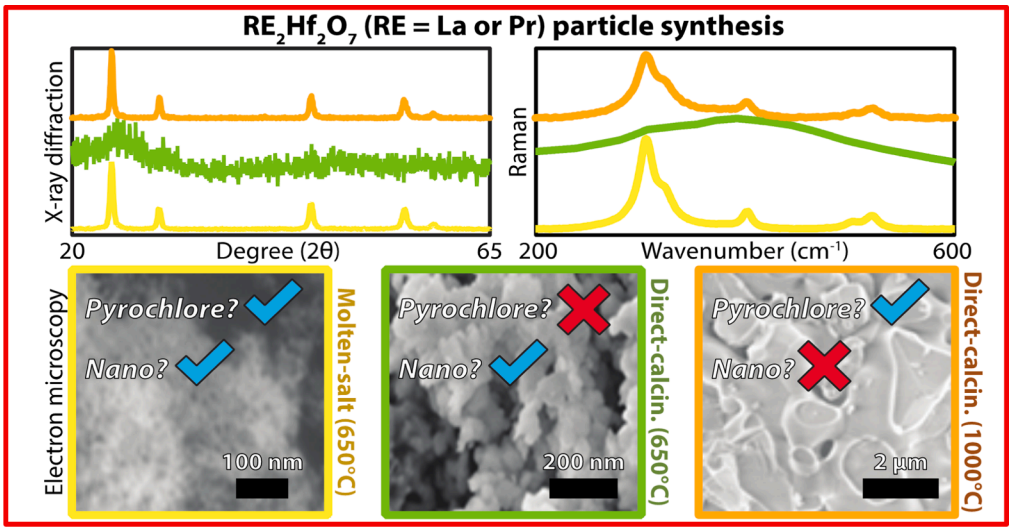

Fig. 26. Schematic showing the formation of pyrochlore NPs at 650 °C, unlike forming microparticles in case of direct calcination [177]. *Copyright 2018. Reproduced with permission from the American Chemical Society.*

4. Summary and perspective

Materials design with well-defined morphology, narrow size distribution and high phase purity through generalizable, scalable, reproducible and green chemistry approaches is a focal point of materials science research globally. Among various bottom-up approaches for the synthesis of nanomaterials, the MSS method is one of the simplest techniques which is efficient, green, easy, highly reliable, and generalizable to carry out in research laboratories without sophisticated instrumentation compared to high temperature solid-state and ceramic routes, sol–gel, or combustion techniques. It is also easy to scale-up for industrial-scale synthesis. It can produce highly uniform NPs without agglomeration unlike conventional colloidal, hydrothermal and solvothermal synthesis methods. In recent years, it has been explored for the synthesis of various technologically important materials with properties and applications including ferroelectricity, ferromagnetism, electrodes for Li-ion batteries, semiconductors, luminescent materials, photocatalysts, and electrocatalysts especially in nanosized domain even with complex compositions. It is expected that this synthesis method will attain more popularity in coming years with advancement in science and technology and enable more complexities associated with the design of nanostructured materials for humankind.

In this review article, we have explained the different aspects of the MSS method and highlighted its importance in designing high quality nanomaterials for advanced applications. Strong polarizing and ionizing nature of molten salts used in the MSS process offers

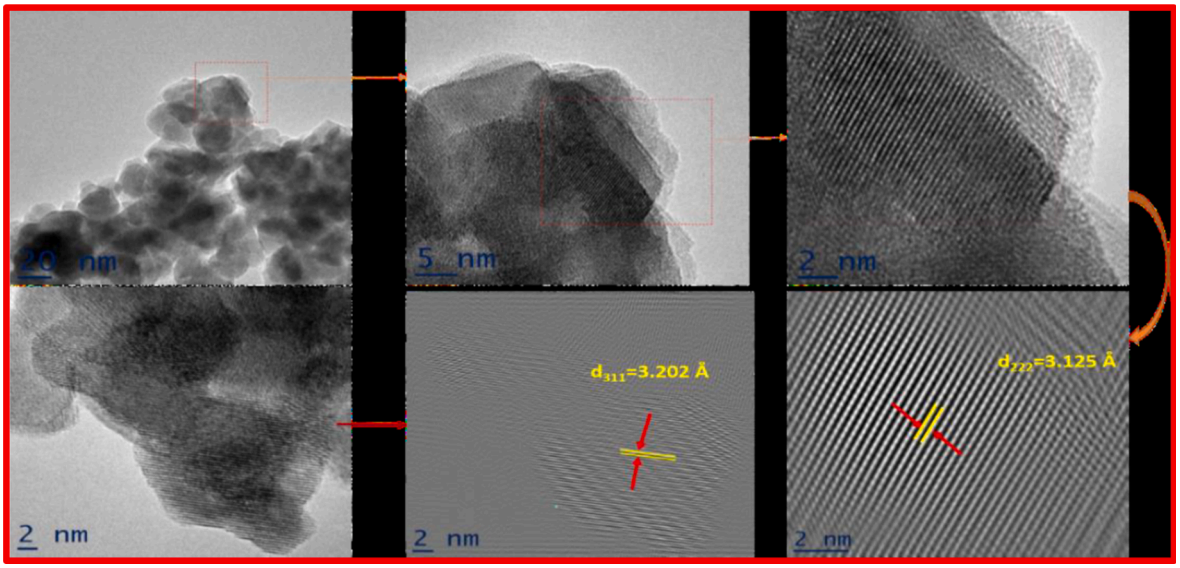

Fig. 27. The $La_2Hf_2O_7$ NPs synthesized by the MSS method: representative TEM images and corresponding Fourier transform images [101]. *Copyright 2018. Reproduced with permission from the American Chemical Society.*

exemplary solvation power for various oxides and covalent solids. It facilitates easy and fast mass transfer, and therefore aids in uniform nucleation process in a continuous liquid phase. The MSS method has demonstrated as a highly successful approach to synthesize both simple and complex metal oxides such as perovskites, delafossites, spinels and pyrochlores. The advanced MSS derivatives, such as TMSS, aerosol MSS, and kinetically modified MSS, for materials synthesis have also been reviewed.

In the future, more sophisticated characterization tools, especially for in situ characterizations, are required to analyze different species formed at different stages throughout the MSS process. Several processes which happen at micron level in the formation of micro/nanocrystalline materials are not well understood, which is a big curtail in the chemical and physical aspects pertaining to rational synthesis of new solid materials. The investigation of the structure-forming processes is an enormous challenge for both analytical and theoretical methods because very small particles or aggregates with different chemical composition and different sizes must be probed, both before and during their nucleation and growth. Furthermore, the used precursors are present in a complex and dynamic equilibrium. Pienack et al. have written a review article on in situ monitoring of crystalline solid using several techniques such as in situ scattering, spectroscopy, microscopy, etc. [349]. Some of the specific techniques are small angle x-ray scattering, small angle neutron scattering, mass spectrometry, x-ray absorption spectroscopy, transmission electron microscopy, etc. Guiton and her colleagues from the University of Kentucky have used in situ TEM to probe structural phase transformation (SPT) in nanostructure materials [350]. They have exploited in situ heating and biasing in the TEM to probe SPT in inorganic, single-phase, solid-state, and nanostructured systems. This will give better understanding of the molten salt chemistry.

Moreover, a quantitative approach for understanding the kinetics of molten salt reaction with the reactant species can give more detailed insight on the role of various synthesis parameters which are needed to be optimized for fine tuning the size, shape and composition of nanomaterials.

This is well explained in work carried out by Xiao et al. for synthesis of β-Li_2TiO_3 crystals and Hojamberdiev et al. for the synthesis of $La_2Ti_2O_7$ crystals [351,352]. Xiao et al. have realized (0 0 1) faceted β-Li_2TiO_3 crystals in Na_2SO_4 molten salt. They have postulated that the formed aggregates of 1–10 μm in size at 900–1000 °C dissolve in the flux at higher annealing time (10 h holding at 1000 °C) to produce $Li^+/[TiO_{2+x}]^{x-}/O^{2-}$ species wherein O^{2-} are solvated by sulfate ion of the flux. At lower solute concentration, Li^+ and Na^+ ions are attached to the negatively charged (0 0 1) surface via electrostatic interaction. At equilibrium, only Na^+ ions get adsorbed on the (0 0 1) surface preferentially whereas Li^+ ions migrate to the side surface of the crystals. Then they react with $[TiO_{2+x}]^{x-}$ and O^{2-} leading to the formation of β-Li_2TiO_3 crystals.

Morphology of crystals grown by flux assisted methods are strongly dependent on several factors, including solute–solvent interaction and the crystal–solution interface. Hojamberdiev et al. realized $La_2Ti_2O_7$ with different morphologies using the fluxes of Na_2MoO_4, K_2MoO_4, NaCl, and the mixture of NaCl + K_2MoO_4 (molar ratio = 3:7). Using the MSS process with the alkali-metal molybdate flux, they could produce $La_2Ti_2O_7$ platelet crystals with dominant (1 0 0) facet which otherwise is very difficult.

It was reported by Afanasiev et al. that the charged planes which has large density of alkali ions in a crystal structure would be preferentially exposed in the crystalline products [353]. It was believed that the growth of $La_2Ti_2O_7$ platelet crystals might be happening via a Burton–Cabrera–Frank (BCF)-type screw-dislocation process [352]. The crystal growth rate in high-temperature ionic melts is mediated by the ion diffusing rate to kinks in spiral steps. Although the flux mediated crystal growth is generally a BCF-type screw-dislocation process as just mentioned [354], there can be other mechanisms which might also govern their nucleation and growth such as oriented attachment and a Kirkendall effect [353] and layer-by-layer growth [355].

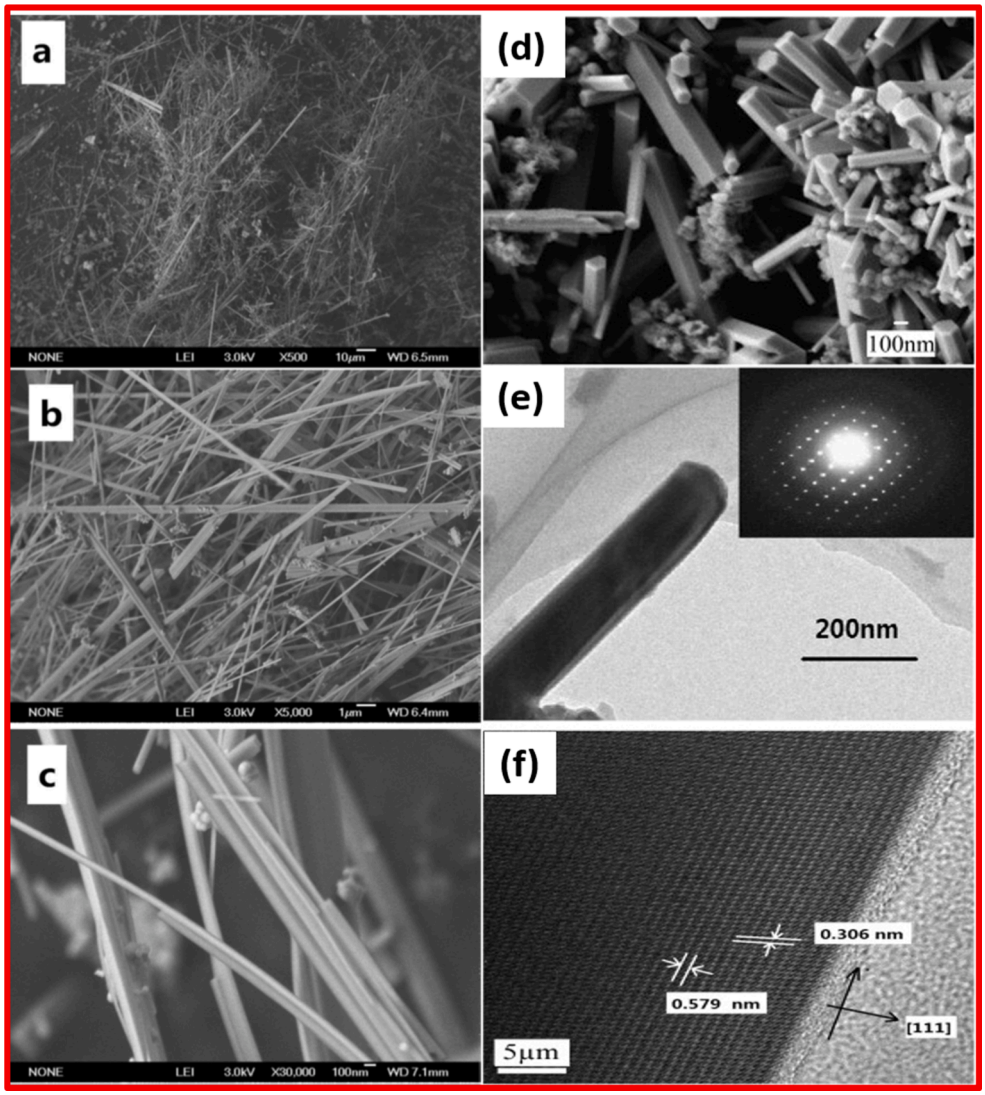

Fig. 28. (a–c) $Lu_2Ti_2O_7$ nanowires synthesized using KCl salt at 1000 °C [342]. *Copyright 2012. Reproduced with permission from the Royal Society of Chemistry.* (d–f) $Lu_2Ti_2O_7$ nanorods synthesized using NaCl salt at 1000 °C [341]. *Copyright 2012. Reproduced with permission from Elsevier.*

The examples just described above are about bulk materials, not nanomaterials. That is exactly the point: we all can learn what have achieved on bulk materials and then extend what we have learned to study the growth of nanomaterials.

Equipped with knowledge of the nanomaterial synthesis by the MSS method via in situ and mechanistic studies, one can establish the correlation among various critical synthesis parameters such as the reaction pH, nucleation kinetics, rate constant, and activation energy of the final products. One then could establish more control over the MSS of metal oxide NPs and predict the final outcome. In this article, we have qualitatively discussed various aspects of the MSS method as the best as we can at the current stage. In the future, more efforts need to be invested on establishing more systematic correlation between the various experimental synthesis parameters and the thermodynamics and kinetics of the molten salt reactions for nanomaterials. Furthermore, small angle X-ray scattering, small angle neutron scattering, and X-ray absorption spectroscopy of reaction precursors, intermediates and products along with theoretical calculations (e.g. DFT calculations) could also be quite helpful to validate the empirical trends of various experimental results observed in the MSS method for nanomaterials such as particle size variation as a function of synthesis conditions, effect of salt composition and S/R ratio on morphology and other similar results. These efforts could help us understand various chemical and physical aspects involved not only in the MSS method but other bottom-up approaches for the synthesis of nanomaterials.

Declaration of Competing Interest

The authors declare that they have no known competing financial interests or personal relationships that could have appeared to influence the work reported in this paper.

Acknowledgement

YM would like to thank the financial support by the National Science Foundation under CHE (Award #1952803 and 1710160) and the IIT startup funds. SKG thanks the United States-India Education Foundation (USIEF, India) and the Institute of International Education (IIE, USA) for his Fulbright Nehru Postdoctoral Fellowship (Award #2268/FNPDR/2017).

References

[1] Srivastava R. Synthesis and characterization techniques of nanomaterials. Int J Green Nanotechnol 2012;4:17–27.
[2] Gatoo MA, Naseem S, Arfat MY, Mahmood Dar A, Qasim K, Zubair S. Physicochemical properties of nanomaterials: implication in associated toxic manifestations. Biomed Res Int 2014:8.
[3] Schneider T. Evaluation and control of occupational health risks from nanoparticles. Nordic Council of Ministers; 2007.
[4] Dan G, Guoxin X, Jianbin L. Mechanical properties of nanoparticles: basics and applications. J Phys D Appl Phys 2014;47:013001.
[5] Chunglok A, Muensit N, Daengngam C. Extreme wetting-resistant multiscale nano-/microstructured surfaces for viscoelastic liquid repellence. J Nanomater 2016;2016.
[6] Ghorai S. Chemical, physical and mechanical properties of nanomaterials and its applications; 2013.
[7] Dong L, Craig MM, Khang D, Chen C. Applications of nanomaterials in biology and medicine. J Nanotechnol 2012;2012.
[8] Yurkov GY, Fionov AS, Koksharov YA, Koleso VV, Gubin SP. Electrical and magnetic properties of nanomaterials containing iron or cobalt nanoparticles. Inorg Mater 2007;43:834–44.
[9] Kumbhakar P, Ray SS, Stepanov AL. Optical properties of nanoparticles and nanocomposites. J Nanomater 2014;2014.
[10] Geng J, Lu D, Zhu J-J, Chen H-Y. Antimony (III)-doped $PbWO_4$ crystals with enhanced photoluminescence via a shape-controlled sonochemical route. J Phys Chem B 2006;110:13777–85.
[11] Honig J, Spałek J. Electronic properties of $NiS_{2-x}Se_x$ single crystals: from magnetic Mott–Hubbard insulators to normal metals. Chem Mater 1998;10:2910–29.
[12] Rao C, Vivekchand S, Biswas K, Govindaraj A. Synthesis of inorganic nanomaterials. Dalton Trans 2007:3728–49.
[13] Cushing BL, Kolesnichenko VL, O'Connor CJ. Recent advances in the liquid-phase syntheses of inorganic nanoparticles. Chem Rev 2004;104:3893–946.
[14] Mao Y, Park TJ, Zhang F, Zhou H, Wong SS. Environmentally friendly methodologies of nanostructure synthesis. Small 2007;3:1122–39.
[15] Patzke GR, Krumeich F, Nesper R. Oxidic nanotubes and nanorods—anisotropic modules for a future nanotechnology. Angew Chem Int Ed 2002;41:2446–61.
[16] Rao CNR, Nath M. Inorganic nanotubes. Dalton Trans 2003:1–24.
[17] Bhatia S. Nanoparticles types, classification, characterization, fabrication methods and drug delivery applications. In: Natural polymer drug delivery systems. Springer; 2016. p. 33–93.
[18] Khan I, Saeed K, Khan I. Nanoparticles: Properties, applications and toxicities. Arabian J Chem 2017.
[19] Zhang X-F, Liu Z-G, Shen W, Gurunathan S. Silver nanoparticles: synthesis, characterization, properties, applications, and therapeutic approaches. Int J Mol Sci 2016;17:1534.
[20] Corr SA. Metal oxide nanoparticles. In: Nanoscience: Volume 1: Nanostructures through chemistry. The Royal Society of Chemistry; 2013. p. 180–207.
[21] Fernández-Garcia M, Rodriguez J. Metal oxide nanoparticles-nanomaterials: inorganic and bioinorganic perspectives. Brookhaven National Laboratory; 2007.
[22] Einarsrud M-A, Grande T. 1D oxide nanostructures from chemical solutions. Chem Soc Rev 2014;43:2187–99.
[23] Liu X, Fechler N, Antonietti M. Salt melt synthesis of ceramics, semiconductors and carbon nanostructures. Chem Soc Rev 2013;42:8237–65.
[24] Mao Y, Tran T, Guo X, Huang JY, Shih CK, Wang KL, et al. Luminescence of nanocrystalline erbium-doped yttria. Adv Funct Mater 2009;19:748–54.
[25] Li L, Deng J, Chen J, Sun X, Yu R, Liu G, et al. Wire structure and morphology transformation of niobium oxide and niobates by molten salt synthesis. Chem Mater 2009;21:1207–13.
[26] Wang W, Xu C, Wang G, Liu Y, Zheng C. Preparation of smooth single-crystal Mn_3O_4 nanowires. Adv Mater 2002;14:837–40.
[27] Tiano AL, Koenigsmann C, Santulli AC, Wong SS. Solution-based synthetic strategies for one-dimensional metal-containing nanostructures. Chem Commun 2010;46:8093–130.
[28] Xu C-Y, Zhang Q, Zhang H, Zhen L, Tang J, Qin L-C. Synthesis and characterization of single-crystalline alkali titanate nanowires. J Am Chem Soc 2005;127:11584–5.
[29] Mao Y, Banerjee S, Wong SS. Large-scale synthesis of single-crystalline perovskite nanostructures. J Am Chem Soc 2003;125:15718–9.
[30] Zuniga JP, Abdou M, Gupta SK, Mao Y. Molten-salt synthesis of complex metal oxide nanoparticles. JoVE 2018:e58482.
[31] Kerridge DH. Recent advances in molten salts as reaction media. Pure Appl Chem 1975;41:355–71.
[32] Volkov S. Chemical reactions in molten salts and their classification. Chem Soc Rev 1990;19:21–8.
[33] Sundermeyer W. Fused salts and their use as reaction media. Angew Chem Int Ed Engl 1965;4:222–38.
[34] Knauth P, Schoonman J. Nanostructured materials: Selected synthesis methods, properties and applications. Springer Science & Business Media; 2006.
[35] Nikam A, Prasad B, Kulkarni A. Wet chemical synthesis of metal oxide nanoparticles: a review. CrystEngComm 2018;20:5091–107.
[36] Ealia SAM, Saravanakumar M. A review on the classification, characterisation, synthesis of nanoparticles and their application. In: IOP conference series: materials science and engineering. IOP Publishing; 2017. p. 032019.
[37] Livage J, Henry M, Sanchez C. Sol-gel chemistry of transition metal oxides. Prog Solid State Chem 1988;18:259–341.
[38] Feinle A, Elsaesser MS, Huesing N. Sol–gel synthesis of monolithic materials with hierarchical porosity. Chem Soc Rev 2016;45:3377–99.
[39] de Azevedo Marques AP, De Melo DM, Paskocimas CA, Pizani PS, Joya MR, Leite ER, et al. Photoluminescent $BaMoO_4$ nanopowders prepared by complex polymerization method (CPM). J Solid State Chem 2006;179:671–8.
[40] Nersisyan HH, Lee JH, Ding J-R, Kim K-S, Manukyan KV, Mukasyan AS. Combustion synthesis of zero-, one-, two- and three-dimensional nanostructures: Current trends and future perspectives. Prog Energy Combust Sci 2017;63:79–118.
[41] Kakihana M, Arima M, Nakamura Y, Yashima M, Yoshimura M. Spectroscopic characterization of precursors used in the Pechini-type polymerizable complex processing of barium titanate. Chem Mater 1999;11:438–50.
[42] Aruna ST, Mukasyan AS. Combustion synthesis and nanomaterials. Curr Opin Solid State Mater Sci 2008;12:44–50.
[43] Tyagi A. Combustion synthesis: a soft-chemical route for functional nano-ceramics. BARC newsletter 2006.
[44] Ganguli AK, Ganguly A, Vaidya S. Microemulsion-based synthesis of nanocrystalline materials. Chem Soc Rev 2010;39:474–85.
[45] Zawadzki M, Wrzyszcz J. Hydrothermal synthesis of nanoporous zinc aluminate with high surface area. Mater Res Bull 2000;35:109–14.
[46] Lou Z, He M, Wang R, Qin W, Zhao D, Chen C. Large-scale synthesis of monodisperse magnesium ferrite via an environmentally friendly molten salt route. Inorg Chem 2014;53:2053–7.
[47] Plechkova NV, Seddon KR. Applications of ionic liquids in the chemical industry. Chem Soc Rev 2008;37:123–50.
[48] Mao Y, Guo X, Huang JY, Wang KL, Chang JP. Luminescent nanocrystals with $A_2B_2O_7$ composition synthesized by a kinetically modified molten salt method. J Phys Chem C 2009;113:1204–8.
[49] Huang Z, Li F, Jiao C, Liu J, Huang J, Lu L, et al. Molten salt synthesis of $La_2Zr_2O_7$ ultrafine powders. Ceram Int 2016;42:6221–7.
[50] Beyene AM, Baek C, Jung WK, Ragupathy P, Kim DK. Understanding the role of oxygen ion (O^{2-}) activity in 1-D crystal growth of rutile TiO_2 in molten salts. CrystEngComm 2018;20:487–95.
[51] Shavel A, Guerrini L, Alvarez-Puebla RA. Colloidal synthesis of silicon nanoparticles in molten salts. Nanoscale 2017;9:8157–63.
[52] Gouget G, Debecker DP, Kim A, Olivieri G, Gallet J-J, Bournel F, et al. In situ solid-gas reactivity of nanoscaled metal borides from molten salt synthesis. Inorg Chem 2017;56:9225–34.

[53] Zou X, Ji L, Hsu H-Y, Zheng K, Pang Z, Lu X. Designed synthesis of SiC nanowire-derived carbon with dual-scale nanostructures for supercapacitor applications. J Mater Chem A 2018;6:12724–32.
[54] Liu X, Antonietti M, Giordano C. Manipulation of phase and microstructure at nanoscale for SiC in molten salt synthesis. Chem Mater 2013;25:2021–7.
[55] Liu X, Giordano C, Antonietti M. A molten-salt route for synthesis of Si and Ge nanoparticles: chemical reduction of oxides by electrons solvated in salt melt. J Mater Chem 2012;22:5454–9.
[56] Grosjean R, Le Godec Y, Delacroix S, Gouget G, Beaunier P, Ersen O, et al. A high pressure pathway toward boron-based nanostructured solids. Dalton Trans 2018;47:7634–9.
[57] Huang Y-B, Pachfule P, Sun J-K, Xu Q. From covalent–organic frameworks to hierarchically porous B-doped carbons: a molten-salt approach. J Mater Chem A 2016;4:4273–9.
[58] Kanady JS, Leidinger P, Haas A, Titlbach S, Schunk S, Schierle-Arndt K, et al. Synthesis of Pt_3Y and other early-late intermetallic nanoparticles by way of a molten reducing agent. J Am Chem Soc 2017;139:5672–5.
[59] Chen Z, Gu Y, Hu L, Xiao W, Mao X, Zhu H, et al. Synthesis of nanostructured graphite via molten salt reduction of CO_2 and SO_2 at a relatively low temperature. J Mater Chem A 2017:20603–7.
[60] Zhang W, Pan X, Long P, Liu X, Long X, Yu Y, et al. Platinum nanoparticles supported on defective tungsten bronze-type $KSr_2Nb_5O_{15}$ as a novel photocatalyst for efficient ethylene oxidation. J Mater Chem A 2017;5:18998–9006.
[61] Urbankowski P, Anasori B, Makaryan T, Er D, Kota S, Walsh PL, et al. Synthesis of two-dimensional titanium nitride Ti_4N_3 (MXene). Nanoscale 2016;8:11385–91.
[62] Zhang H, Dasbiswas K, Ludwig NB, Han G, Lee B, Vaikuntanathan S, et al. Stable colloids in molten inorganic salts. Nature 2017;542:328.
[63] Hu Z, Xiao X, Jin H, Li T, Chen M, Liang Z, et al. Rapid mass production of two-dimensional metal oxides and hydroxides via the molten salts method. Nat Commun 2017;8:15630.
[64] Peng R, Wu N, Zheng Y, Huang Y, Luo Y, Yu P, et al. Large-scale synthesis of metal-ion-doped manganese dioxide for enhanced electrochemical performance. ACS Appl Mater Interfaces 2016;8:8474–80.
[65] Jin R, Liu H, Guan Y, Zhou J, Li G. Molten salt synthesis of fluorine-doped Mn_3O_4 nanobelts as anode materials for Li-ion batteries. CrystEngComm 2015;17:7717–22.
[66] Srivastava V, Kamysbayev V, Hong L, Dunietz E, Klie RF, Talapin DV. Colloidal chemistry in molten salts: synthesis of luminescent $In_{1-x}Ga_xP$ and $In_{1-x}Ga_xAs$ quantum dots. J Am Chem Soc 2018;140:12144–51.
[67] Portehault D, Delacroix S, Gouget G, Grosjean R, Chan-Chang T-H-C. Beyond the compositional threshold of nanoparticle-based materials. Acc Chem Res 2018;51:930–9.
[68] Xue P, Wu H, Lu Y, Zhu X. Recent progress in molten salt synthesis of low-dimensional perovskite oxide nanostructures, structural characterization, properties, and functional applications: a review. J Mater Sci Technol 2018;34:914–30.
[69] Kimura T. Molten salt synthesis of ceramic powders. In: Advances in ceramics-synthesis and characterization, processing and specific applications; 2011. p. 75–100.
[70] Kimura T, Holmes MH, Newnham RE. Fabrication of grain-oriented Bi_2WO_6 ceramics. J Am Ceram Soc 1982;65:223–6.
[71] Li B-R, Shang W, Hu Z-L, Zhang N-Q. Template-free fabrication of pure single-crystalline $BaTiO_3$ nano-wires by molten salt synthesis technique. Ceram Int 2014;40:73–80.
[72] Arendt RH, Rosolowski JH, Szymaszek JW. Lead zirconate titanate ceramics from molten salt solvent synthesized powders. Mater Res Bull 1979;14:703–9.
[73] Wickham D. The preparation of ferrites with the aid of fused salts. Proc. Int. Conf. Ferrites 1971:105–7.
[74] Albayrak C, Barım G, Dag Ö. Effect of hygroscopicity of the metal salt on the formation and air stability of lyotropic liquid crystalline mesophases in hydrated salt–surfactant systems. J Colloid Interface Sci 2014;433:26–33.
[75] Lin Y, Dong J, Dai J, Wang J, Yang H, Zong H. Facile synthesis of flowerlike $LiFe_5O_8$ microspheres for electrochemical supercapacitors. Inorg Chem 2017;56:14960–7.
[76] Afanasiev P, Geantet C. Synthesis of solid materials in molten nitrates. Coord Chem Rev 1998;178:1725–52.
[77] Flood H, Förland T. The acidic and basic properties of oxides. Acta Chem Scand 1947;1:592–604.
[78] Lux H. "Acids" and "bases" in a fused salt bath: the determination of oxygen-ion concentration. Z Elektrochem Soc 1939;45:303–10.
[79] Sherer CS. The role of alkali metal cations in Lux-Flood acid-base reactions in fused salt media. J Inorg Nucl Chem 1972;34:1615–9.
[80] Lusiola T, Bortolani F, Zhang Q, Dorey R. Molten hydroxide synthesis as an alternative to molten salt synthesis for producing $K_{0.5}Na_{0.5}NbO_3$ lead free ceramics. J Mater Sci 2012;47:1938–42.
[81] González-Jiménez IN, Torres-Pardo A, Rano S, Laberty-Robert C, Hernández-Garrido JC, López-Haro M, et al. Multicationic $Sr_4Mn_3O_{10}$ mesostructures: molten salt synthesis, analytical electron microscopy study and reactivity. Mater Horiz 2018;5:480–5.
[82] Huo K, Zhu B, Fu J, Li X, Chu PK. Large-scale synthesis of mullite nanowires by molten salt method. J Nanosci Nanotechnol 2010;10:4792–6.
[83] Shoemaker DP, Chung DY, Mitchell JF, Bray TH, Soderholm L, Chupas PJ, et al. Understanding fluxes as media for directed synthesis: In situ local structure of molten potassium polysulfides. J Am Chem Soc 2012;134:9456–63.
[84] Sunshine SA, Kang D, Ibers JA. A new low-temperature route to metal polychalcogenides: solid-state synthesis of potassium titanium sulfide ($K_4Ti_3S_{14}$), a novel one-dimensional compound. J Am Chem Soc 1987;109:6202–4.
[85] Wan DM, Wang J, Ng SC, Gan LM. Formation and characterization of lead magnesium niobate synthesized from the molten salt of potassium chlorate. J Alloy Compd 1998;274:110–7.
[86] Urben P. Bretherick's handbook of reactive chemical hazards. Elsevier; 2017.
[87] Helan M, Berchmans LJ, Jose TP, Visuvasam A, Angappan S. Molten salt synthesis of $LiMn_2O_4$ using chloride–carbonate melt. Mater Chem Phys 2010;124:439–42.
[88] Boltersdorf J, King N, Maggard PA. Flux-mediated crystal growth of metal oxides: synthetic tunability of particle morphologies, sizes, and surface features for photocatalysis research. CrystEngComm 2015;17:2225–41.
[89] Gupta SK, Zuniga JP, Abdou M, Mao Y. Thermal annealing effects on $La_2Hf_2O_7$:Eu^{3+} nanoparticles: a curious case study of structural evolution and site-specific photo- and radio-luminescence. Inorg Chem Front 2018;5:2508–21.
[90] Abdou M, Gupta SK, Zuniga JP, Mao Y. On structure and phase transformation of uranium doped $La_2Hf_2O_7$ nanoparticles as an efficient nuclear waste host. Mater Chem Front 2018;2:2201–11.
[91] Zuniga JP, Gupta SK, Abdou M, Mao Y. Effect of molten salt synthesis processing duration on the photo- and radioluminescence of UV-, visible-, and X-ray-excitable $La_2Hf_2O_7$:Eu^{3+} nanoparticles. ACS Omega 2018;3:7757–70.
[92] Yoon KH, Cho YS, Kang DH. Molten salt synthesis of lead-based relaxors. J Mater Sci 1998;33:2977–84.
[93] Kimura T, Takahashi T, Yamaguchi T. Preparation and characteristics of Ni-ferrite powders obtained in the presence of fused salts. J Mater Sci 1980;15:1491–7.
[94] Kimura T, Yamaguchi T. Morphology of Bi_2WO_6 powders obtained in the presence of fused salts. J Mater Sci 1982;17:1863–70.
[95] Akdogan EK, Brennan RE, Allahverdi M, Safari A. Effects of molten salt synthesis (MSS) parameters on the morphology of $Sr_3Ti_2O_7$ and $SrTiO_3$ seed crystals. J Electroceram 2006;16:159–65.
[96] Schmalzried H. Chemical kinetics of solids. John Wiley & Sons; 2008.
[97] Hayashi Y, Kimura T, Yamaguchi T. Preparation of rod-shaped $BaTiO_3$ powder. J Mater Sci 1986;21:757–62.
[98] Takahashi T, Mogushi N, Kimura T, Yamaguchi T. Formation mechanism of ferrite powders in flux. Nippon Kagaku Kaishi 1981;1981:1391–5.
[99] Nachtrieb NH. Conduction in fused salts and salt-metal solutions. Annu Rev Phys Chem 1980;31:131–56.
[100] Honea EC, Homer ML, Labastie P, Whetten RL. Localization of an excess electron in sodium halide clusters. Phys Rev Lett 1989;63:394.
[101] Selloni A, Carnevali P, Car R, Parrinello M. Localization, hopping, and diffusion of electrons in molten salts. Phys Rev Lett 1987;59:823.

[102] Li L, Deng J, Chen J, Xing X. Topochemical molten salt synthesis for functional perovskite compounds. Chem Sci 2016;7:855–65.
[103] Liu JR, Hong RY, Feng WG, Badami D, Wang YQ. Large-scale production of strontium ferrite by molten-salt-assisted coprecipitation. Powder Technol 2014;262:142–9.
[104] Hailili R, Wang C, Lichtfouse E. Perovskite nanostructures assembled in molten salt based on halogen anions KX (X = F, Cl and Br): Regulated morphology and defect-mediated photocatalytic activity. Appl Catal B 2018;232:531–43.
[105] Mao Y. Facile molten-salt synthesis of double perovskite La_2BMnO_6 nanoparticles. RSC Adv 2012;2:12675–8.
[106] Mao Y, Parsons J, McCloy JS. Magnetic properties of double perovskite La_2BMnO_6 (B = Ni or Co) nanoparticles. Nanoscale 2013;5:4720–8.
[107] Mao Y, Wong SS. Composition and shape control of crystalline $Ca_{1-x}Sr_xTiO_3$ perovskite nanoparticles. Adv Mater 2005;17:2194–9.
[108] Rojas-Hernandez RE, Rubio-Marcos F, Gonçalves RH, Rodriguez MAN, Véron E, Allix M, et al. Original synthetic route to obtain a $SrAl_2O_4$ phosphor by the molten salt method: insights into the reaction mechanism and enhancement of the persistent luminescence. Inorg Chem 2015;54:9896–907.
[109] Reddy MV, Xu Y, Rajarajan V, Ouyang T, Chowdari BVR. Template free facile molten synthesis and energy storage studies on MCo_2O_4 (M = Mg, Mn) as anode for Li-ion batteries. ACS Sustainable Chem Eng 2015;3:3035–42.
[110] Pokhrel M, Wahid K, Mao Y. Systematic studies on $RE_2Hf_2O_7$:5%Eu^{3+} (RE = Y, La, Pr, Gd, Er, and Lu) nanoparticles: Effects of the A-Site RE^{3+} cation and calcination on structure and photoluminescence. J Phys Chem C 2016;120:14828–39.
[111] Wahid K, Pokhrel M, Mao Y. Structural, photoluminescence and radioluminescence properties of Eu^{3+} doped $La_2Hf_2O_7$ nanoparticles. J Solid State Chem 2017;245:89–97.
[112] Zuniga JP, Gupta SK, Pokhrel M, Mao Y. Exploring the optical properties of $La_2Hf_2O_7$:Pr^{3+} nanoparticles under UV and X-ray excitation for potential lighting and scintillating applications. New J Chem 2018;42:9381–92.
[113] Mao Y, Park T-J, Wong SS. Synthesis of classes of ternary metal oxide nanostructures. Chem Commun 2005:5721–35.
[114] Mao Y, Zhou H, Wong SS. Synthesis, properties and applications of perovskite phase metal oxide nanostructures. Mater Matters 2010;5:50.
[115] Park T-J, Papaefthymiou GC, Moodenbaugh AR, Mao Y, Wong SS. Synthesis and characterization of submicron single-crystalline $Bi_2Fe_4O_9$ cubes. J Mater Chem 2005;15:2099–105.
[116] Liu JR, Hong RY, Feng WG, Badami D, Wang YQ. Large scale production of strontium ferrite by molten salt assited coprecipitation. Powder Technol 2014;262:142–9.
[117] Gilbert MR. Molten salt synthesis of titanate pyrochlore waste-forms. Ceram Int 2016;42:5263–70.
[118] Chang Y, Wu J, Zhang M, Kupp E, Messing CL. Molten salt synthesis of morphology controlled alpha-alumina platelets. Ceram Int 2017;43:12684–8.
[119] Huang Z, Duan H, Liu J, Zhang H. Preparation of lanthanum cerate powders via a simple molten salt route. Ceram Int 2016;42:10482–6.
[120] Wang G, Liu Y, Ye J, Qiu W, Ma S, An X. Fabrication of rod-like Ti_4O_7 with high conductivity by molten salt synthesis. Mater Lett 2017;186:361–3.
[121] Pokhrel M, Burger A, Groza M, Mao Y. Enhance the photoluminescence and radioluminescence of $La_2Zr_2O_7$:Eu^{3+} core nanoparticles by coating with a thin Y_2O_3 shell. Opt Mater 2017;68:35–41.
[122] Ramesh G, Subramanian V, Sivasubramanian V. Dielectric properties of lead indium niobate ceramics synthesized by conventional solid state reaction method. Mater Res Bull 2010;45:1871–4.
[123] Gupta SK, Sudarshan K, Ghosh P, Srivastava A, Bevara S, Pujari P, et al. Role of various defects in the photoluminescence characteristics of nanocrystalline $Nd_2Zr_2O_7$: an investigation through spectroscopic and DFT calculations. J Mater Chem C 2016:4988–5000.
[124] Kato H, Kobayashi M, Hara M, Kakihana M. Fabrication of $SrTiO_3$ exposing characteristic facets using molten salt flux and improvement of photocatalytic activity for water splitting. Catal Sci Technol 2013;3:1733–8.
[125] Gonzalo-Juan I, Riedel R. Ceramic synthesis from condensed phases. ChemTexts 2016;2:6.
[126] Hayashi Y, Kimura T, Yamaguchi T. Mechanism of Flux-Aided Reaction in Ferrite Systems. Bull Am Ceram Soc 1985;64:1249.
[127] Onoda Jr GY, Hench LL. The science of ceramic processing before firing. Florida Univ Gainesville Dept of Materials Science and Engineering; 1977.
[128] Boltersdorf J, Wong T, Maggard PA. Synthesis and optical properties of Ag (I), Pb (II), and Bi (III) tantalate-based photocatalysts. ACS Catal 2013;3:2943–53.
[129] Choi J, King N, Maggard PA. Metastable Cu (I)-niobate semiconductor with a low-temperature, nanoparticle-mediated synthesis. ACS Nano 2013;7:1699–708.
[130] Geselbracht MJ, Walton RI, Cowell ES, Millange F, O'Hare D. An investigation of the synthesis of the layered perovskite $RbCa_2Nb_3O_{10}$ using time-resolved in situ high-temperature powder X-ray diffraction. Chem Mater 2002;14:4343–9.
[131] King N, Sahoo PP, Fuoco L, Stuart S, Dougherty D, Liu Y, et al. Copper deficiency in the p-type semiconductor $Cu_{1-x}Nb_3O_8$. Chem Mater 2014;26:2095–104.
[132] McLamb N, Sahoo PP, Fuoco L, Maggard PA. Flux growth of single-crystal $Na_2Ta_4O_{11}$ particles and their photocatalytic hydrogen production. Cryst Growth Des 2013;13:2322–6.
[133] Porob DG, Maggard PA. Flux syntheses of La-doped $NaTaO_3$ and its photocatalytic activity. J Solid State Chem 2006;179:1727–32.
[134] Geselbracht MJ, Noailles LD, Ngo LT, Pikul JH, Walton RI, Cowell ES, et al. Probing molten salt flux reactions using time-resolved in situ high-temperature powder X-ray diffraction: A new synthesis route to the mixed-valence $NaTi_2O_4$. Chem Mater 2004;16:1153–9.
[135] Bugaris DE, Zur Loye HC. Materials discovery by flux crystal growth: Quaternary and higher order oxides. Angew Chem Int Ed 2012;51:3780–811.
[136] Fu J, Daanen NN, Rugen EE, Chen DP, Skrabalak SE. Simple reactor for ultrasonic spray synthesis of nanostructured materials. Chem Mater 2017;29:62–8.
[137] Mann AK, Fu J, DeSantis CJ, Skrabalak SE. Spatial and temporal confinement of salt fluxes for the shape-controlled synthesis of Fe_2O_3 nanocrystals. Chem Mater 2013;25:1549–55.
[138] Mann AK, Wicker S, Skrabalak SE. Aerosol-assisted molten salt synthesis of $NaInS_2$ nanoplates for use as a new photoanode material. Adv Mater 2012;24:6186–91.
[139] Mann AK, Skrabalak SE. Synthesis of single-crystalline nanoplates by spray pyrolysis: a metathesis route to Bi_2WO_6. Chem Mater 2011;23:1017–22.
[140] Chen DP, Fu J, Skrabalak SE. Towards shape control of metal oxide nanocrystals in confined molten media. ChemNanoMat 2015;1:18–26.
[141] Gurav A, Kodas T, Pluym T, Xiong Y. Aerosol processing of materials. Aerosol Sci Technol 1993;19:411–52.
[142] Okuyama K, Lenggoro IW. Preparation of nanoparticles via spray route. Chem Eng Sci 2003;58:537–47.
[143] Kodas TT, Hampden-Smith MJ. Aerosol processing of materials. New York: Wiley-Vch; 1999.
[144] Picard GS, Bouyer FC. Molecular modelling: An analytical tool with a predictive character for investigating reactivity in molten salt media. In: AIP conference proceedings. American Institute of Physics; 1995. p. 295–304.
[145] Warren WW. Electronic properties of metal/molten salt solutions. In: Molten salts: From fundamentals to applications. Springer; 2002. p. 23–46.
[146] Ignatiev V. Molten salts for safe, low waste and proliferation resistant treatment of radwaste in accelerator driven and critical systems. In: Molten salts: From fundamentals to applications. Springer; 2002. p. 263–82.
[147] Richardson FD. Physical chemistry of melts in metallurgy. Academic Press; 1974.
[148] Thanh NTK, Maclean N, Mahiddine S. Mechanisms of nucleation and growth of nanoparticles in solution. Chem Rev 2014;114:7610–30.
[149] Kim D-W, Sudare T, Nakanishi T, Yuasa S, Yubuta K, Zettsu N, et al. Flux-mediated topochemical growth of platelet-shaped perovskite $LiNbO_3$ single crystals from layered potassium niobate crystals. Cryst Growth Des 2018;18:4111–6.
[150] Niu W, Zhang L, Xu G. Seed-mediated growth of noble metal nanocrystals: crystal growth and shape control. Nanoscale 2013;5:3172–81.
[151] Choi J, King N, Maggard PA. Metastable Cu(I)-niobate semiconductor with a low-temperature, nanoparticle-mediated synthesis. ACS Nano 2013;7:1699–708.
[152] Arney D, Watkins T, Maggard PA. Effects of particle surface areas and microstructures on photocatalytic H_2 and O_2 production over $PbTiO_3$. J Am Ceram Soc 2011;94:1483–9.
[153] Deloume J-P, Scharff J-P, Marote P, Durand B, Abou-Jalil A. Molten alkali metal oxonitrates, a liquid state for nanosized perovskite phase elaboration. J Mater Chem 1999;9:107–10.
[154] Huang K-C, Huang T-C, Hsieh W-F. Morphology-controlled synthesis of barium titanate nanostructures. Inorg Chem 2009;48:9180–4.
[155] Zhang Y, Wang L, Xue D. Molten salt route of well dispersive barium titanate nanoparticles. Powder Technol 2012;217:629–33.
[156] Tian X, Li J, Chen K, Han J, Pan S. Template-free and scalable synthesis of core–shell and hollow $BaTiO_3$ particles: Using molten hydrated salt as a solvent. Cryst Growth Des 2009;9:4927–32.

[157] Ge H, Hou Y, Xia C, Zhu M, Wang H, Yan H. Preparation and piezoelectricity of $NaNbO_3$ high-density ceramics by molten salt synthesis. J Am Ceram Soc 2011; 94:4329–34.
[158] Santulli AC, Zhou H, Berweger S, Raschke MB, Sutter E, Wong SS. Synthesis of single-crystalline one-dimensional $LiNbO_3$ nanowires. CrystEngComm 2010;12: 2675–8.
[159] Yu J, Tang S, Wang R, Shi Y, Nie B, Zhai L, et al. Synthesis of single-crystalline barium dititanate nanobelts. Cryst Growth Des 2008;8:1481–3.
[160] Baral A, Varma K. Low temperature molten-salt synthesis of nanocrystalline cubic Sr_2SbMnO_6. J Solid State Chem 2009;182:3282–8.
[161] Liu X, Wu J, Huang X, Liu Z, Zhang Y, Wang M, et al. Predominant growth orientation of $Li_{1.2}(Mn_{0.4}Co_{0.4})O_2$ cathode materials produced by the NaOH compound molten salt method and their enhanced electrochemical performance. J Mater Chem A 2014;2:15200–8.
[162] Liu J, Hou M, Yi J, Guo S, Wang C, Xia Y. Improving the electrochemical performance of layered lithium-rich transition-metal oxides by controlling the structural defects. Energy Environ Sci 2014;7:705–14.
[163] Shi SJ, Tu JP, Tang YY, Liu XY, Zhao XY, Wang XL, et al. Morphology and electrochemical performance of $Li[Li_{0.2}Mn_{0.54}Ni_{0.13}Co_{0.13}]O_2$ cathode materials treated in molten salts. J Power Sources 2013;241:186–95.
[164] Yu C, Li G, Guan X, Zheng J, Li L. Composite $Li[Li_{0.11}Mn_{0.57}Ni_{0.32}]O_2$: Two-step molten-salt synthesis, oxidation state stabilization, and uses as high-voltage cathode for lithium-ion batteries. J Alloy Compd 2012;528:121–5.
[165] ZhenYao W, Biao L, Jin M, DingGuo X. The enhanced electrochemical performance of nanocrystalline $Li[Li_{0.26}Ni_{0.11}Mn_{0.63}]O_2$ synthesized by the molten-salt method for Li-ion batteries. Electrochim Acta 2014;117:285–91.
[166] Fu J, Hou Y, Zheng M, Zhu M. Topochemical build-up of $BaTiO_3$ nanorods using $BaTi_2O_5$ as the template. CrystEngComm 2017;19:1115–22.
[167] Schaak RE, Mallouk TE. Perovskites by design: A toolbox of solid-state reactions. Chem Mater 2002;14:1455–71.
[168] Xu C-Y, Zhen L, Yang R, Wang ZL. Synthesis of single-crystalline niobate nanorods via ion-exchange based on molten-salt reaction. J Am Chem Soc 2007;129: 15444–5.
[169] Saito Y, Takao H, Tani T, Nonoyama T, Takatori K, Homma T, et al. Lead-free piezoceramics. Nature 2004;432:84–7.
[170] Li L, Deng J, Yu R, Chen J, Wang Z, Xing X. Niobium pentoxide hollow nanospheres with enhanced visible light photocatalytic activity. J Mater Chem A 2013; 1:11894–900.
[171] Fu J, Hou Y, Liu X, Zheng M, Zhu M. A construction strategy of ferroelectrics by the molten salt method and its application in the energy field. J Mater Chem C 2020;8:8704–31.
[172] Jansen M. A concept for synthesis planning in solid-state chemistry. Angew Chem Int Ed 2002;41:3746–66.
[173] Weng X, Boldrin P, Abrahams I, Skinner SJ, Darr JA. Direct syntheses of mixed ion and electronic conductors $La_4Ni_3O_{10}$ and $La_3Ni_2O_7$ from nanosized coprecipitates. Chem Mater 2007;19:4382–4.
[174] Gupta SK, Abdou M, Ghosh PS, Zuniga JP, Mao Y. Thermally induced disorder-order phase transition of $Gd_2Hf_2O_7$:Eu^{3+} nanoparticles and its implication on photo- and radioluminescence. ACS Omega 2019;4:2779–91.
[175] Gupta SK, Abdou M, Zuniga JP, Ghosh PS, Molina E, Xu B, et al. Roles of oxygen vacancies and pH induced size changes on photo- and radioluminescence of undoped and Eu^{3+}-doped $La_2Zr_2O_7$ nanoparticles. J Lumin 2019;209:302–15.
[176] Gupta SK, Penilla M, Zuniga JP, Abdou M, Mao Y. Visible and ultraviolet upconversion and near infrared downconversion luminescence from lanthanide doped $La_2Zr_2O_7$ nanoparticles. J Lumin 2019:116591.
[177] Pokhrel M, Gupta SK, Wahid K, Mao Y. Pyrochlore rare-earth hafnate $RE_2Hf_2O_7$ (RE = La and Pr) nanoparticles stabilized by molten-salt synthesis at low temperature. Inorg Chem 2019;58:1241–51.
[178] Pokhrel M, Alcoutlabi M, Mao Y. Optical and X-ray induced luminescence from Eu^{3+} doped $La_2Zr_2O_7$ nanoparticles. J Alloy Compd 2017;693:719–29.
[179] Alaparthi SB, Tian Y, Mao Y. Synthesis and photoluminescence properties of $La_2Zr_2O_7$:Eu^{3+}@YBO_3 core@shell nanoparticles. Nanotechnology 2013;25: 025703.
[180] Trummel V, Gupta SK, Pokhrel M, Wall D, Mao Y. Investigating the impact of gamma radiation on structural and optical properties of Eu^{3+} doped rare-earth hafnate pyrochlore nanocrystals. J Lumin 2019;207:1–13.
[181] Alaparthi SB, Lu L, Tian Y, Mao Y. Europium doped lanthanum zirconate nanoparticles with high concentration quenching. Mater Res Bull 2014;49:114–8.
[182] Pokhrel M, Brik MG, Mao Y. Particle size and crystal phase dependent photoluminescence of $La_2Zr_2O_7$:Eu^{3+} nanoparticles. J Am Ceram Soc 2015;98:3192–201.
[183] Xia Y, Yang P, Sun Y, Wu Y, Mayers B, Gates B, et al. One-dimensional nanostructures: synthesis, characterization, and applications. Adv Mater 2003;15: 353–89.
[184] Du Y, Inman D. Synthesis of MgO powders from molten salts. J Mater Sci 1997;32:2373–9.
[185] Jiang Z-Y, Xu T, Xie Z-X, Lin Z-W, Zhou X, Xu X, et al. Molten salt route toward the growth of ZnO nanowires in unusual growth directions. J Phys Chem B 2005;109:23269–73.
[186] Wang C, Chang F, Zhang X, Zhan R, Liu Y. Minimization of defects in Nb-doped TiO_2 photocatalysts by molten salt flux. Ceram Int 2018;44:10249–57.
[187] Zhang J, Li R. Molten salt synthesis of hexagonal tungsten trioxide nanoparticles for lithium-ion battery anode. Mater Lett 2018;233:199–202.
[188] Park T-J, Wong SS. As-prepared single-crystalline hematite rhombohedra and subsequent conversion into monodisperse aggregates of magnetic nanocomposites of iron and magnetite. Chem Mater 2006;18:5289–95.
[189] Ke X, Cao J, Zheng M, Chen Y, Liu J, Ji G. Molten salt synthesis of single-crystal Co_3O_4 nanorods. Mater Lett 2007;61:3901–3.
[190] Wang X, Hu C, Liu H, Du G, He X, Xi Y. Synthesis of CuO nanostructures and their application for nonenzymatic glucose sensing. Sens Actuators, B 2010;144: 220–5.
[191] Sun Q, Zeng Y, Jiang D. Synthesis and morphological transition of Ni^{2+} doped Rh-In_2O_3 nanocrystals under $LiNO_3$ molten salts. Appl Phys Lett 2012;101: 073109.
[192] Ahmed J, Mao Y. Ultrafine iridium oxide nanorods synthesized by molten salt method toward electrocatalytic oxygen and hydrogen evolution reactions. Electrochim Acta 2016;212:686–93.
[193] Zuwei Z, Chenguo H, Yufeng X, Rusen Y, Zhong Lin W. Synthesis of Ba-doped CeO_2 nanowires and their application as humidity sensors. Nanotechnology 2007;18:465504.
[194] Grabis J, Jankovica D, Sokolova E, Steins I. Characteristics of zirconia nanoparticles prepared by molten salts and microwave synthesis. In: IOP conference series: Materials science and engineering, 49; 2013. p. 012003.
[195] Cheng J, Zhang H, Ma H, Zhong H, Zou Y. Study of carbon-supported IrO_2 and RuO_2 for use in the hydrogen evolution reaction in a solid polymer electrolyte electrolyzer. Electrochim Acta 2010;55:1855–61.
[196] Lee Y, Suntivich J, May KJ, Perry EE, Shao-Horn Y. Synthesis and activities of rutile IrO_2 and RuO_2 nanoparticles for oxygen evolution in acid and alkaline solutions. J Phys Chem Lett 2012;3:399–404.
[197] Chao T, Liu C, Hsieh A, Chang H, Huang Y, Tsai D. Quartz crystal microbalance sensor based on nanostructured IrO_2. Sens Actuators, B 2007;122:95–100.
[198] Chen Y, Chen C, Huang Y, Lee K, Tiong K. Synthesis of IrO_2 nanocrystals on carbon nanotube bundle arrays and their field emission characteristics. J Alloy Compd 2009;487:659–64.
[199] Chen C, Chen Y, Huang Y, Tsai D, Liao P, Tiong K. Synthesis and structural characterization of twinned V-shaped IrO_2 nanowedges on TiO_2 nanorods via MOCVD. J Alloy Compd 2009;480:107–10.
[200] Chen C, Chen Y, Huang Y, Tsai D, Tiong K, Du C. Growth and characterization of V-shaped IrO_2 nanowedges via metal-organic vapor deposition. Nanotechnology 2008;19:465607.
[201] Chen RS, Chen YS, Huang YS, Chen YL, Chi Y, Liu CS, et al. Growth of IrO_2 films and nanorods by means of CVD: an example of compositional and morphological control of nanostructures. Chem Vap Deposition 2003;9:301–5.
[202] Chen R, Huang Y, Liang Y, Tsai D, Tiong K. Growth and characterization of iridium dioxide nanorods. J Alloy Compd 2004;383:273–6.
[203] Chen R-S, Huang Y-S, Liang Y-M, Tsai D-S, Chi Y, Kai J-J. Growth control and characterization of vertically aligned IrO_2 nanorods. J Mater Chem 2003;13: 2525–9.

[204] Wang G, Tsai D-S, Huang Y-S, Korotcov A, Yeh W-C, Susanti D. Selective growth of IrO_2 nanorods using metalorganic chemical vapor deposition. J Mater Chem 2006;16:780–6.
[205] Lee Y, Kang M, Shim JH, Lee N-S, Baik JM, Lee Y, et al. Growth of highly single crystalline IrO_2 nanowires and their electrochemical applications. J Phys Chem C 2012;116:18550–6.
[206] Zhao C, Yu H, Li Y, Li X, Ding L, Fan L. Electrochemical controlled synthesis and characterization of well-aligned IrO_2 nanotube arrays with enhanced electrocatalytic activity toward oxygen evolution reaction. J Electroanal Chem 2013;688:269–74.
[207] Satishkumar B, Govindaraj A, Nath M, Rao CNR. Synthesis of metal oxide nanorods using carbon nanotubes as templates. J Mater Chem 2000;10:2115–9.
[208] Tang J, Kong B, Wang Y, Xu M, Wang Y, Wu H, et al. Photoelectrochemical detection of glutathione by IrO_2–Hemin–TiO_2 nanowire arrays. Nano Lett 2013;13:5350–4.
[209] Korotcov A, Hsu HP, Huang YS, Tsai DS. Raman scattering characterization of well-aligned IrO_2 nanocrystals grown on sapphire substrates via reactive sputtering. J Raman Spectrosc 2006;37:1411–5.
[210] Ardizzone S, Bianchi CL, Borgese L, Cappelletti G, Locatelli C, Minguzzi A, et al. Physico-chemical characterization of IrO_2–SnO_2 sol-gel nanopowders for electrochemical applications. J Appl Electrochem 2009;39:2093–105.
[211] Puthiyapura VK, Pasupathi S, Su H, Liu X, Pollet B, Scott K. Investigation of supported IrO2 as electrocatalyst for the oxygen evolution reaction in proton exchange membrane water electrolyser. Int J Hydrogen Energy 2014;39:1905–13.
[212] Siracusano S, Baglio V, Stassi A, Ornelas R, Antonucci V, Aricò A. Investigation of IrO_2 electrocatalysts prepared by a sulfite-couplex route for the O_2 evolution reaction in solid polymer electrolyte water electrolyzers. Int J Hydrogen Energy 2011;36:7822–31.
[213] Cruz J, Baglio V, Siracusano S, Ornelas R, Ortiz-Frade L, Arriaga L, et al. Nanosized IrO_2 electrocatalysts for oxygen evolution reaction in an SPE electrolyzer. J Nanopart Res 2011;13:1639–46.
[214] Lim J, Park D, Jeon SS, Roh CW, Choi J, Yoon D, et al. Ultrathin IrO_2 nanoneedles for electrochemical water oxidation. Adv Funct Mater 2018;28:1704796.
[215] Ye Y, Liu E, Hu X, Yan Z, Jiang Z, Fan J. Preparation and luminescence properties of Y_2O_3: Er^{3+}/TiO_2 with high specific surface area. Chin Sci Bull 2011;56:2668.
[216] Mao Y, Huang JY, Ostroumov R, Wang KL, Chang JP. Synthesis and luminescence properties of erbium-doped Y_2O_3 nanotubes. J Phys Chem C 2008;112:2278–85.
[217] Gupta SK, Zuniga JP, Ghosh PS, Abdou M, Mao Y. Correlating structure and luminescence properties of undoped and $La_2Hf_2O_7$:Eu^{3+} NPs prepared with different coprecipitating pH values through experimental and theoretical studies. Inorg Chem 2018;57:11815–30.
[218] Gupta SK, Sudarshan K, Ghosh P, Sanyal K, Srivastava A, Arya A, et al. Luminescence of undoped and Eu^{3+} doped nanocrystalline $SrWO_4$ scheelite: time resolved fluorescence complimented by DFT and positron annihilation spectroscopic studies. RSC Adv 2016;6:3792–805.
[219] Li J-G, Li X, Sun X, Ishigaki T. Monodispersed colloidal spheres for uniform Y_2O_3:Eu^{3+} red-phosphor particles and greatly enhanced luminescence by simultaneous Gd^{3+} doping. J Phys Chem C 2008;112:11707–16.
[220] Gupta SK, Sudarshan K, Srivastava A, Kadam R. Visible light emission from bulk and nano $SrWO_4$: Possible role of defects in photoluminescence. J Lumin 2017;192:1220–6.
[221] Sudarshan K, Sharma SK, Gupta R, Gupta SK, Sayed FN, Pujari PK. Role of surface defects in catalytic properties of CeO_2 nanoparticles towards oxygen reduction reaction. Mater Chem Phys 2017;200:99–106.
[222] Shukla R, Gupta SK, Grover V, Natarajan V, Tyagi AK. The role of reaction conditions in the polymorphic control of Eu^{3+} doped $YInO_3$: structure and size sensitive luminescence. Dalton Trans 2015;44:10628–35.
[223] Gupta SK, Mohapatra M, Kaity S, Natarajan V, Godbole S. Structure and site selective luminescence of sol–gel derived Eu:Sr_2SiO_4. J Lumin 2012;132:1329–38.
[224] Gupta SK, Mohapatra M, Natarajan V, Godbole S. Site-specific luminescence of Eu^{3+} in gel-combustion-derived strontium zirconate perovskite nanophosphors. J Mater Sci 2012;47:3504–15.
[225] Wu X, Liang Y, Liu M, Chen R, Li Y. Synthesis and fluorescence properties of Y_2O_3:Eu by molten salt synthesis method. J Rare Earths 2010;28:688–92.
[226] Huang Y, Ye H-Q, Zhuang W-D, Hu Y-S, Zhao C-L, Li C, et al. Preparation of Y_2O_3:Eu^{3+} phosphor by molten salt assisted method. Trans Nonferrous Met Soc China 2007;17:644–8.
[227] Cahn J. On the morphology stability of growth crystals in crystal growth. Oxford (UK): Pergamon; 1967.
[228] Luo L, Hu F, Xiong L, Li X, Zhou M, Wang Z. Luminescent properties of Y_2O_3:Eu^{3+} nanocrystals prepared by molten salt synthesis. J Nanomater 2013;2013:2.
[229] Gupta SK, Ghosh P, Pathak N, Arya A, Natarajan V. Understanding the local environment of Sm^{3+} in doped $SrZrO_3$ and energy transfer mechanism using time-resolved luminescence: a combined theoretical and experimental approach. RSC Adv 2014;4:29202–15.
[230] Gupta SK, Ghosh P, Pathak N, Tewari R. Nature of defects in blue light emitting $CaZrO_3$: Spectroscopic and theoretical study. RSC Adv 2015;5:56526–33.
[231] Gupta SK, Ghosh PS, Yadav AK, Pathak N, Arya A, Jha SN, et al. Luminescence properties of $SrZrO_3$/Tb^{3+} perovskite: host-dopant energy-transfer dynamics and local structure of Tb^{3+}. Inorg Chem 2016;55:1728–40.
[232] Gupta SK, Grover V, Shukla R, Srinivasu K, Natarajan V, Tyagi AK. Exploring pure and RE co-doped (Eu^{3+}, Tb^{3+} and Dy^{3+}) gadolinium scandate: Luminescence behaviour and dynamics of energy transfer. Chem Eng J 2016;283:114–26.
[233] Gupta SK, Kadam RM, Natarajan V, Godbole SV. Nanoparticles of $Sr_{0.995}Gd_{0.005}ZrO_3$-gel-combustion synthesis, characterization, fluorescence and EPR spectroscopy. Mater Sci Eng, B 2014;183:6–11.
[234] Gupta SK, Pathak N, Gupta R, Thulasidas S, Natarajan V. Probing the oxidation state and coordination geometry of uranium ion in $SrZrO_3$ perovskite. J Mol Struct 2014;1068:204–9.
[235] Banerjee S, Kim D-I, Robinson RD, Herman IP, Mao Y, Wong SS. Observation of Fano asymmetry in Raman spectra of $SrTiO_3$ and $Ca_xSr_{1-x}TiO_3$ perovskite nanocubes. Appl Phys Lett 2006;89:223130.
[236] Berweger S, Neacsu CC, Mao Y, Zhou H, Wong SS, Raschke MB. Optical nanocrystallography with tip-enhanced phonon Raman spectroscopy. Nat Nanotechnol 2009;4:496.
[237] Mao Y, Banerjee S, Wong SS. Hydrothermal synthesis of perovskite nanotubes. Chem Commun 2003:408–9.
[238] Pradhan SK, Mao Y, Wong SS, Chupas P, Petkov V. Atomic-scale structure of nanosized titania and titanate: particles, wires, and tubes. Chem Mater 2007;19:6180–6.
[239] Zhang F, Mao Y, Park T-J, Wong SS. Green synthesis and property characterization of single-crystalline perovskite fluoride nanorods. Adv Funct Mater 2008;18:103–12.
[240] Zhou H, Mao Y, Wong SS. Probing structure–parameter correlations in the molten salt synthesis of $BaZrO_3$ perovskite submicrometer-sized particles. Chem Mater 2007;19:5238–49.
[241] Zhou H, Mao Y, Wong SS. Shape control and spectroscopy of crystalline $BaZrO_3$ perovskite particles. J Mater Chem 2007;17:1707–13.
[242] Park T-J, Mao Y, Wong SS. Synthesis and characterization of multiferroic $BiFeO_3$ nanotubes. Chem Commun 2004:2708–9.
[243] Yoon KH, Oh KY, Yoon SO. Influence of synthesis methods of the PTCR effect in semiconductive $BaTiO_3$. Mater Res Bull 1986;21:1429–37.
[244] Ito Y, Shimada S, Inagaki M. Molten-salt synthesis of $Ba_{1-x}Pb_xTiO_3$ in the system $BaTiO_3$–$PbCl_2$. J Am Ceram Soc 1995;78:2695–9.
[245] Deng H, Qiu Y, Yang S. General surfactant-free synthesis of $MTiO_3$ (M = Ba, Sr, Pb) perovskite nanostrips. J Mater Chem 2009;19:976–82.
[246] Sahoo GK, Mazumder R. Grain size effect on the dielectric properties of molten salt synthesized $BaTiO_3$. Ferroelectrics 2010;402:193–9.
[247] Li H-L, Du Z-N, Wang G-L, Zhang Y-C. Low temperature molten salt synthesis of $SrTiO_3$ submicron crystallites and nanocrystals in the eutectic NaCl–KCl. Mater Lett 2010;64:431–4.
[248] Cai Z, Xing X, Yu R, Sun X, Liu G. Morphology-controlled synthesis of lead titanate powders. Inorg Chem 2007;46:7423–7.
[249] Yang J, Hou Y, Wang C, Zhu M, Yan H. Relaxor behavior of $(K_{0.5}Bi_{0.5})TiO_3$ ceramics derived from molten salt synthesized single-crystalline nanowires. Appl Phys Lett 2007;91:023118.
[250] Hu C, Liu H, Lao C, Zhang L, Davidovic D, Wang Z. Size-manipulable synthesis of single-crystalline $BaMnO_3$ and $BaTi_{1/2}Mn_{1/2}O_3$ nanorods/nanowires. J Phys Chem B 2006;110:14050–4.

[251] Song W, Salvador PA, Rohrer GS. Influence of the magnitude of ferroelectric domain polarization on the photochemical reactivity of $BaTiO_3$. ACS Appl Mater Interfaces 2018;10:41450–7.
[252] Li T, Lipatov A, Lu H, Lee H, Lee J-W, Torun E, et al. Optical control of polarization in ferroelectric heterostructures. Nat Commun 2018;9:3344.
[253] Defay E, Faye R, Despesse G, Strozyk H, Sette D, Crossley S, et al. Enhanced electrocaloric efficiency via energy recovery. Nat Commun 2018;9:1827.
[254] Wang L, Feng Q, Kim Y, Kim R, Lee KH, Pollard SD, et al. Ferroelectrically tunable magnetic skyrmions in ultrathin oxide heterostructures. Nat Mater 2018;17:1087–94.
[255] Jang S, Oh JH. Rapid fabrication of microporous $BaTiO_3$/PDMS nanocomposites for triboelectric nanogenerators through one-step microwave irradiation. Sci Rep 2018;8:14287.
[256] Malakooti MH, Julé F, Sodano HA. Printed nanocomposite energy harvesters with controlled alignment of barium titanate nanowires. ACS Appl Mater Interfaces 2018;10:38359–67.
[257] Wu J, Qin N, Yuan B, Lin E, Bao D. Enhanced pyroelectric catalysis of $BaTiO_3$ nanowires for utilizing waste heat in pollution treatment. ACS Appl Mater Interfaces 2018;10:37963–73.
[258] Wu J, Qin N, Bao D. Effective enhancement of piezocatalytic activity of $BaTiO_3$ nanowires under ultrasonic vibration. Nano Energy 2018;45:44–51.
[259] Demircivi P, Simsek EB. Visible-light-enhanced photoactivity of perovskite-type W-doped $BaTiO_3$ photocatalyst for photodegradation of tetracycline. J Alloy Compd 2019;774:795–802.
[260] Dhanalakshmi M, Basavaraj RB, Darshan GP, Sharma SC, Nagabhushana H. Pivotal role of fluxes in $BaTiO_3$:Eu^{3+} nano probes for visualization of latent fingerprints on multifaceted substrates and anti-counterfeiting applications. Microchem J 2019;145:226–34.
[261] Morsi MA, Abdelaziz M, Oraby AH, Mokhles I. Structural, optical, thermal, and dielectric properties of polyethylene oxide/carboxymethyl cellulose blend filled with barium titanate. J Phys Chem Solids 2019;125:103–14.
[262] Lu X, Tong Y, Cheng ZY. Fabrication and characterization of free-standing, flexible and translucent $BaTiO_3$-P(VDF-CTFE) nanocomposite films. J Alloy Compd 2019;770:327–34.
[263] Fu J, Hou Y, Zheng M, Zhu M. Comparative study of dielectric properties of the PVDF composites filled with spherical and rod-like $BaTiO_3$ derived by molten salt synthesis method. J Mater Sci 2018;53:7233–48.
[264] Teresa Buscaglia M, Harnagea C, Dapiaggi M, Buscaglia V, Pignolet A, Nanni P. Ferroelectric $BaTiO_3$ nanowires by a topochemical solid-state reaction. Chem Mater 2009;21:5058–65.
[265] Lv D, Zuo R, Su S. Processing and morphology of (111) $BaTiO_3$ crystal platelets by a two-step molten salt method. J Am Ceram Soc 2012;95:1838–42.
[266] Ahmed J, Mao Y. Delafossite $CuAlO_2$ nanoparticles with electrocatalytic activity toward oxygen and hydrogen evolution reactions, nanomaterials for sustainable energy. American Chemical Society; 2015. p. 57–72.
[267] Cossuet T, Resende J, Rapenne L, Chaix-Pluchery O, Jiménez C, Renou G, et al. ZnO/$CuCrO_2$ core-shell nanowire heterostructures for self-powered UV photodetectors with fast response. Adv Funct Mater 2018;28:1803142.
[268] Tong B, Deng Z, Xu B, Meng G, Shao J, Liu H, et al. Oxygen vacancy defects boosted high performance p-type delafossite $CuCrO_2$ gas sensors. ACS Appl Mater Interfaces 2018;10:34727–34.
[269] Mohan S, Mao Y. Dependence of (Photo) electrochemical properties on geometry factors of hydrothermally synthesized delafossite copper gallium oxide $CuGaO_2$ toward oxygen evolution reaction. J Electrochem Soc 2018;165:H607–13.
[270] Mohan S, Mao Y. Hydrothermally synthesized copper gallium delafossite nanoflakes for (photo) electrocatalytic water splitting. ECS Trans 2017;77:1985–94.
[271] Zhao S-Y, Zhang B, Su H, Zhang J-J, Li X-H, Wang K-X, et al. Enhanced oxygen electroreduction over nitrogen-free carbon nanotube-supported $CuFeO_2$ nanoparticles. J Mater Chem A 2018;6:4331–6.
[272] Youn DH, Choi YH, Kim J-H, Han S, Heller A, Mullins CB. Simple microwave-assisted synthesis of delafossite $CuFeO_2$ as an anode material for sodium-ion batteries. ChemElectroChem 2018;5:2419–23.
[273] Wang J, Daunis TB, Cheng L, Zhang B, Kim J, Hsu JWP. Combustion synthesis of p-type transparent conducting $CuCrO_{2+x}$ and Cu:CrO_x thin films at 180 °C. ACS Appl Mater Interfaces 2018;10:3732–8.
[274] Dunlap-Shohl WA, Daunis TB, Wang X, Wang J, Zhang B, Barrera D, et al. Room-temperature fabrication of a delafossite $CuCrO_2$ hole transport layer for perovskite solar cells. J Mater Chem A 2018;6:469–77.
[275] Szymanski NJ, Walters LN, Hellman O, Gall D, Khare SV. Dynamical stabilization in delafossite nitrides for solar energy conversion. J Mater Chem A 2018;6:20852–60.
[276] Akin S, Liu Y, Dar MI, Zakeeruddin SM, Grätzel M, Turan S, et al. Hydrothermally processed $CuCrO_2$ nanoparticles as an inorganic hole transporting material for low-cost perovskite solar cells with superior stability. J Mater Chem A 2018;6:20327–37.
[277] Schiavo E, Latouche C, Barone V, Crescenzi O, Muñoz-García AB, Pavone M. An ab initio study of Cu-based delafossites as an alternative to nickel oxide in photocathodes: effects of Mg-doping and surface electronic features. PCCP 2018;20:14082–9.
[278] Deng Z, Meng G, Fang X, Dong W, Shao J, Wang S, et al. A novel ammonia gas sensors based on p-type delafossite $AgAlO_2$. J Alloy Compd 2019;777:52–8.
[279] Chen Y, Chen T, Wu X, Yang G. $CuMnO_2$ nanoflakes as pH-switchable catalysts with multiple enzyme-like activities for cysteine detection. Sens Actuators, B 2019;279:374–84.
[280] El-Bassuony AAH, Abdelsalam HK. Attractive improvement in structural, magnetic, optical, and antimicrobial activity of silver delafossite by Fe/Cr doping. J Supercond Novel Magn 2018;31:3691–703.
[281] Nair BG, Joseph JA, Kellner ZT, Sharma V, Remillard SK, DeYoung PA, et al. Tin-incorporated nanostructured copper indium oxide delafossite thin films: Structural, electrical and optical analysis. J Alloy Compd 2018;746:435–44.
[282] Ghosh CK, Popuri SR, Mahesh TU, Chattopadhyay KK. Preparation of nanocrystalline $CuAlO_2$ through sol–gel route. J Sol-Gel Sci Technol 2009;52:75–81.
[283] Yamazaki T, Morimoto S, Hyodo K, Ishikawa T, Ichiyanagi Y. Effect of cobalt-doping on the magnetic properties and crystal structure of delafossite AgFeO2 nanoparticles. J Alloy Compd 2018;745:631–6.
[284] Santra S, Das NS, Das B, Banerjee D, Chattopadhyay KK. Synthesis of $CuBO_2$ nano/microrods via easy molten salt route and study of its field emission properties. Cryst Growth Des 2015;15:1518–25.
[285] Pathak N, Gupta SK, Sanyal K, Kumar M, Kadam RM, Natarajan V. Photoluminescence and EPR studies on Fe^{3+} doped $ZnAl_2O_4$: an evidence for local site swapping of Fe^{3+} and formation of inverse and normal phase. Dalton Trans 2014;43:9313–23.
[286] Pathak N, Sanyal B, Gupta SK, Kadam RM. $MgAl_2O_4$ both as short and long persistent phosphor material: Role of antisite defect centers in determining the decay kinetics. Solid State Sci 2019;88:13–9.
[287] Gupta SK, Pathak N, Ghosh PS, Kadam RM. On the photophysics and speciation of actinide ion in $MgAl_2O_4$ spinel using photoluminescence spectroscopy and first principle calculation: A case study with uranium. J Alloy Compd 2017;695:337–43.
[288] Kumar M, Gupta SK. An insight into optical spectroscopy of intense green emitting $ZnAl_2O_4$:Tb^{3+} nanoparticles: photo, thermally stimulated luminescence and EPR study. J Lumin 2015;168:151–7.
[289] Kumar M, Gupta SK, Kadam RM. Near white light emitting $ZnAl_2O_4$:Dy^{3+} nanocrystals: Sol–gel synthesis and luminescence studies. Mater Res Bull 2016;74:182–7.
[290] Gupta SK, Ghosh PS, Pathak N, Kadam RM. Why host to dopant energy transfer is absent in the $MgAl_2O_4$:Eu^{3+} spinel? And exploring Eu^{3+} site distribution and local symmetry through its photoluminescence: interplay of experiment and theory. RSC Adv 2016;6:42923–32.
[291] Pathak N, Ghosh PS, Gupta SK, Mukherjee S, Kadam RM, Arya A. An insight into the various defects-induced emission in $MgAl_2O_4$ and their tunability with phase behavior: combined experimental and theoretical approach. J Phys Chem C 2016;120:4016–31.
[292] Wu R, Yun C, Wang X, Lu P, Li W, Lin Y, et al. All-oxide nanocomposites to yield large, tunable perpendicular exchange bias above room temperature. ACS Appl Mater Interfaces 2018;10:42593–602.
[293] Yamasaki Y, Miyasaka S, Kaneko Y, He J-P, Arima T, Tokura Y. Magnetic reversal of the ferroelectric polarization in a multiferroic spinel oxide. Phys Rev Lett 2006;96:207204.

[294] Hemberger J, Lunkenheimer P, Fichtl R, Von Nidda H-AK, Tsurkan V, Loidl A. Relaxor ferroelectricity and colossal magnetocapacitive coupling in ferromagnetic $CdCr_2S_4$. Nature 2005;434:364.
[295] Zasada F, Gryboś J, Piskorz W, Sojka Z. Mono- and diatomic reactive oxygen species produced upon O_2 interaction with the (111) facet of cobalt spinel at various conditions—molecular DFT and atomistic thermodynamic investigations. J Phys Chem C 2018;122:27528–39.
[296] Zhang T, Li Z, Zhang Z, Wang L, Sun P, Wang S. Design of a three-dimensional interconnected hierarchical micro-mesoporous structure of graphene as support material for spinel $NiCo_2O_4$ electrocatalysts toward oxygen reduction reaction. J Phys Chem C 2018;122:27469–76.
[297] Li C, Han X, Cheng F, Hu Y, Chen C, Chen J. Phase and composition controllable synthesis of cobalt manganese spinel nanoparticles towards efficient oxygen electrocatalysis. Nat Commun 2015;6:7345.
[298] Arsalani S, Guidelli EJ, Araujo JFDF, Bruno AC, Baffa O. Green synthesis and surface modification of iron oxide nanoparticles with enhanced magnetization using natural rubber latex. ACS Sustainable Chem Eng 2018;6:13756–65.
[299] He W, Liu J, Sun W, Yan W, Zhou L, Wu C, et al. Coprecipitation-gel synthesis and degradation mechanism of octahedral $Li_{1.2}Mn_{0.54}Ni_{0.13}Co_{0.13}O_2$ as high-performance cathode materials for lithium-ion batteries. ACS Appl Mater Interfaces 2018;10:23018–28.
[300] Baqiya MA, Taufiq A, Ayun K, Zainuri M, Pratapa S. Spinel-structured nanoparticles for magnetic and mechanical applications, magnetic spinels-synthesis, properties and applications. InTech; 2017.
[301] Armijo J. The kinetics and mechanism of solid-state spinel formation—A review and critique. Oxid Met 1969;1:171–98.
[302] Lu J, Zhan C, Wu T, Wen J, Lei Y, Kropf AJ, et al. Effectively suppressing dissolution of manganese from spinel lithium manganate via a nanoscale surface-doping approach. Nat Commun 2014;5:5693.
[303] Stein A, Keller SW, Mallouk TE. Turning down the heat: design and mechanism in solid-state synthesis. Science 1993;259:1558–64.
[304] Raj SS, Gupta SK, Grover V, Muthe KP, Natarajan V, Tyagi AK. $MgAl_2O_4$ spinel: Synthesis, carbon incorporation and defect-induced luminescence. J Mol Struct 2015;1089:81–5.
[305] Liang Y, Wang H, Zhou J, Li Y, Wang J, Regier T, et al. Covalent hybrid of spinel manganese–cobalt oxide and graphene as advanced oxygen reduction electrocatalysts. J Am Chem Soc 2012;134:3517–23.
[306] Zhou L, Zhao D, Lou XW. Double-shelled $CoMn_2O_4$ hollow microcubes as high-capacity anodes for lithium-ion batteries. Adv Mater 2012;24:745–8.
[307] Darshane SL, Deshmukh RG, Suryavanshi SS, Mulla IS. Gas-sensing properties of zinc ferrite nanoparticles synthesized by the molten-salt route. J Am Ceram Soc 2008;91:2724–6.
[308] Hosono E, Kudo T, Honma I, Matsuda H, Zhou H. Synthesis of single crystalline spinel $LiMn_2O_4$ nanowires for a lithium ion battery with high power density. Nano Lett 2009;9:1045–51.
[309] Zhang S, Jayaseelan DD, Bhattacharya G, Lee WE. Molten salt synthesis of magnesium aluminate ($MgAl_2O_4$) spinel powder. J Am Ceram Soc 2006;89:1724–6.
[310] Kim JH, Myung ST, Sun YK. Molten salt synthesis of $LiNi_{0.5}Mn_{1.5}O_4$ spinel for 5 V class cathode material of Li-ion secondary battery. Electrochim Acta 2004;49:219–27.
[311] Lu X, Lin X, Shang Y, Huang T, Yu A. Modified KCl molten salt method synthesis of spinel $LiNi_{0.5}Mn_{1.5}O_4$ with loose structure as cathodes for Li-ion batteries. Int J Electrochem Sci 2014;9:7253–65.
[312] Liu Y, Wang G, Xu C, Wang W. Fabrication of Co_3O_4 nanorods by calcination of precursor powders prepared in a novel inverse microemulsion. Chem Commun 2002:1486–7.
[313] Wang X, Zhu J, Liu Y. Spinel lithium manganese oxide nanoparticles: unique molten salt synthesis strategy and excellent electrochemical performances. J Nanosci Nanotechnol 2009;9:6518–22.
[314] Zhao X, Reddy MV, Liu H, Ramakrishna S, Rao GVS, Chowdari BVR. Nano $LiMn_2O_4$ with spherical morphology synthesized by a molten salt method as cathodes for lithium ion batteries. RSC Adv 2012;2:7462–9.
[315] Darshane SL, Suryavanshi SS, Mulla IS. Nanostructured nickel ferrite: A liquid petroleum gas sensor. Ceram Int 2009;35:1793–7.
[316] Mouhib Y, Belaiche M, Briche S. Elaboration, characterization, and magnetic properties of $Ni_{0.5}Zn_{0.5}Fe_2O_4$ nanoparticles of high purity using molten salts technique. Phys Status Solidi (a) 2018;215:1800469.
[317] Jiang H-T, Wang X-F, Yu C-L, Wang L. Molten salt synthesis of $Ni_{0.5}Zn_{0.5}Fe_2O_4$ powders. Mater Manuf Process 2010;25:1489–93.
[318] Childs C, Lawler KV, Hector AL, Petitgirard S, Noked O, Smith JS, et al. Covalency is frustrating: $La_2Sn_2O_7$ and the nature of bonding in pyrochlores under high pressure-temperature conditions. Inorg Chem 2018;57:15051–61.
[319] Trump BA, Koohpayeh SM, Livi KJT, Wen JJ, Arpino KE, Ramasse QM, et al. Universal geometric frustration in pyrochlores. Nat Commun 2018;9:2619.
[320] Sardar K, Petrucco E, Hiley CI, Sharman JDB, Wells PP, Russell AE, et al. Water-splitting electrocatalysis in acid conditions using ruthenate-iridate pyrochlores. Angew Chem Int Ed 2014;53:10960–4.
[321] Weiss M, Bredow T, Marschall R. The influence of Tin(II) incorporation on visible light absorption and photocatalytic activity in defect-pyrochlores. Chem – Eur J 2018;24:18535–43.
[322] Kim J, Shih P-C, Qin Y, Al-Bardan Z, Sun C-J, Yang H. A porous Pyrochlore $Y_2[Ru_{1.6}Y_{0.4}]O_{7-\delta}$ electrocatalyst for enhanced performance towards the oxygen evolution reaction in acidic media. Angew Chem Int Ed 2018;57:13877–81.
[323] Zhong F, Zhao J, Shi L, Xiao Y, Cai G, Zheng Y, et al. Alkaline-earth metals-doped pyrochlore $Gd_2Zr_2O_7$ as oxygen conductors for improved NO_2 sensing performance. Sci Rep 2017;7:4684.
[324] Pandey J, Shrivastava V, Nagarajan R. Metastable $Bi_2Zr_2O_7$ with pyrochlore-like structure: stabilization, oxygen ion conductivity, and catalytic properties. Inorg Chem 2018;57:13667–78.
[325] Ueda K, Kaneko R, Ishizuka H, Fujioka J, Nagaosa N, Tokura Y. Spontaneous Hall effect in the Weyl semimetal candidate of all-in all-out pyrochlore iridate. Nat Commun 2018;9:3032.
[326] Lhotel E, Petit S, Ciomaga Hatnean M, Ollivier J, Mutka H, Ressouche E, et al. Evidence for dynamic kagome ice. Nat Commun 2018;9:3786.
[327] Pan X, Li C, Zheng J, Liang S, Huang R, Yi Z. A new defect pyrochlore Oxide $Sn_{1.06}Nb_2O_{5.59}F_{0.97}$: Synthesis, noble metal hybrids, and photocatalytic applications. Inorg Chem 2018;57:6641–7.
[328] Pal A, Ghosh S, Kumar S, Schwier EF, Sawada M, Shimada K, et al. Electronic structure by X-ray absorption spectroscopy and observation of field induced unusually slow spin relaxation from magnetic properties in pyrochlore $Eu_{2-x}Fe_xTi_2O_7$. J Magn Magn Mater 2019;476:7–17.
[329] Wu Y, Zheng L, He W, He J, Guo H. Effects of Yb^{3+} doping on phase structure, thermal conductivity and fracture toughness of $(Nd_{1-x}Yb_x)_2Zr_2O_7$. Ceram Int 2019;45:3133–9.
[330] Zhong F, Zhao J, Shi L, Cai G, Zheng Y, Zheng Y, et al. Pyrochlore $Pr_2Zr_{1.95}In_{0.05}O_{7+\delta}$ oxygen conductors: Defect-induced electron transport and enhanced NO_2 sensing performances. Electrochim Acta 2019;293:338–47.
[331] Brovelli S, Schaller RD, Crooker SA, García-Santamaría F, Chen Y, Viswanatha R, et al. Nano-engineered electron–hole exchange interaction controls exciton dynamics in core–shell semiconductor nanocrystals. Nat Commun 2011;2:280.
[332] Granados del Águila A, Groeneveld E, Maan JC, de Mello Donegá C, Christianen PCM. Effect of electron-hole overlap and exchange interaction on exciton radiative lifetimes of CdTe/CdSe heteronanocrystals. ACS Nano 2016;10:4102–10.
[333] Wang Z, Zhou G, Jiang D, Wang S. Recent development of $A_2B_2O_7$ system transparent ceramics. J Adv Ceram 2018;7:289–306.
[334] Suresh BA, Yue T, Yuanbing M. Synthesis and photoluminescence properties of $La_2Zr_2O_7$:Eu^{3+}@YBO_3 core@shell nanoparticles. Nanotechnology 2014;25:025703.
[335] Hand ML, Stennett MC, Hyatt NC. Rapid low temperature synthesis of a titanate pyrochlore by molten salt mediated reaction. J Eur Ceram Soc 2012;32:3211–9.
[336] Pokhrel M, Alcoutlabi M, Mao Y. Optical and X-ray induced luminescence from Eu^{3+} doped optical and X-ray induced luminescence from Eu3+ doped $La_2Zr_2O_7$ nanoparticles nanoparticles. J Alloy Compd 2017;693:719–29.
[337] Wang X, Zhu Y, Zhang W. Preparation of lanthanum zirconate nano-powders by Molten Salts method. J Non-Cryst Solids 2010;356:1049–51.
[338] Dharuman N, John Berchmans L. Low temperature synthesis of nano-crystalline gadolinium titanate by molten salt route. Ceram Int 2013;39:8767–71.

[339] Nithyadharseni P, Reddy MV, Ozoemena KI, Balakrishna RG, Chowdari BVR. Low temperature molten salt synthesis of $Y_2Sn_2O_7$ anode material for lithium ion batteries. Electrochim Acta 2015;182:1060–9.
[340] Li B-R, Chang H-B, Liu D-Y, Yuan X-N. Synthesis of $Lu_2Ti_2O_7$ powders by molten salt method. Mater Chem Phys 2011;130:755–9.
[341] Li B-R, Chang H-B, Gao H, Hou S-X. Synthesis of $Lu_2Ti_2O_7$ nano-rods from molten salt with two-step calcinations. Mater Lett 2012;79:219–21.
[342] Li B, Gao H, Guo Y, Hou S. Synthesis and thermal properties of $Lu_2Ti_2O_7$ nano-wires. CrystEngComm 2012;14:4168–72.
[343] Huang Z, Duan H, Liu J, Zhang H. Preparation of lanthanum cerate powders via a simple molten salt route. Ceram Int 2016;42:10482–6.
[344] Gupta H, Brown S, Rani N, Gohel V. A lattice dynamical investigation of the Raman and the infrared frequencies of the cubic $A_2Hf_2O_7$ pyrochlores. J Phys Chem Solids 2002;63:535–8.
[345] Trojan-Piegza J, Gierlotka S, Zych E, Lojkowski W. Spectroscopic studies of nanopowder and nanoceramics $La_2Hf_2O_7$:Pr scintillator. J Am Ceram Soc 2014;97:1595–601.
[346] Ji Y-M, Jiang D-Y, Shi J-L. Preparation and spectroscopic properties of $La_2Hf_2O_7$/Tb. Mater Lett 2005;59:868–71.
[347] Eagleman Y, Weber M, Chaudhry A, Derenzo S. Luminescence study of cerium-doped $La_2Hf_2O_7$: Effects due to trivalent and tetravalent cerium and oxygen vacancies. J Lumin 2012;132:2889–96.
[348] Hirayama M, Sonoyama N, Yamada A, Kanno R. Relationship between structural characteristics and photoluminescent properties of $(La_{1-x}Eu_x)_2M_2O_7$ (M = Zr, Hf, Sn) pyrochlores. J Lumin 2008;128:1819–25.
[349] Pienack N, Bensch W. In-situ monitoring of the formation of crystalline solids. Angew Chem Int Ed 2011;50:2014–34.
[350] Yu L, Hudak BM, Ullah A, Thomas MP, Porter CC, Thisera A, et al. Unveiling the microscopic origins of phase transformations: An in situ TEM perspective. Chem Mater 2020;32:639–50.
[351] Xiao X, Hayashi F, Yubuta K, Selloni A, Teshima K. Effects of alkali cations and sulfate/chloride anions on the flux growth of {001}-faceted β-Li_2TiO_3 crystals. Cryst Growth Des 2017;17:1118–24.
[352] Hojamberdiev M, Yamaguchi A, Yubuta K, Oishi S, Teshima K. Fabrication of $La_2Ti_2O_7$ crystals using an alkali-metal molybdate flux growth method and their nitridability to form $LaTiO_2N$ crystals under a high-temperature NH_3 atmosphere. Inorg Chem 2015;54:3237–44.
[353] Afanasiev P. Snapshots of zinc oxide formation in molten salt: Hollow microtubules generated by oriented attachment and the kirkendall effect. J Phys Chem C 2012;116:2371–81.
[354] Burton W-K, Cabrera N, Frank F. The growth of crystals and the equilibrium structure of their surfaces. Philos Trans R Soc Lond Ser A, Math Phys Sci 1951;243:299–358.
[355] Matsushita Y, Ueda H, Ueda Y. Flux crystal growth and thermal stabilities of LiV_2O_4. Nat Mater 2005;4:845–50.